

LETTER

A Nonequilibrium Framework for Community Responses to Pulse Perturbations

Lucas P. Medeiros¹  | Michael G. Neubert¹  | Heidi M. Sosik¹  | Stephan B. Munch^{2,3} 

¹Biology Department, Woods Hole Oceanographic Institution, Woods Hole, Massachusetts, USA | ²Southwest Fisheries Science Center, National Marine Fisheries Service, National Oceanic and Atmospheric Administration, Santa Cruz, California, USA | ³Department of Applied Mathematics, University of California, Santa Cruz, California, USA

Correspondence: Lucas P. Medeiros (lucas.medeiros@whoi.edu)

Received: 5 May 2025 | **Revised:** 12 December 2025 | **Accepted:** 16 December 2025

Editor: Ian Donohue

Keywords: chaos | cycles | disturbances | reactivity | resilience | stability | transient

ABSTRACT

Understanding responses of ecological communities to shocks that displace species abundances is of paramount importance given the increasing frequency of extreme climatic events. However, current theory on responses to such pulse perturbations focuses on equilibrium points and we lack a unified framework that accommodates other common, but more complicated, population fluctuations such as transients and cycles. Here we introduce this framework by deriving metrics that quantify the minimum, typical and maximum amplification of perturbed abundances for nonequilibrium population dynamics. By simulating models under several nonequilibrium scenarios, we demonstrate that these metrics accurately characterise the full range of amplification of perturbed abundances in the short and long terms. Notably, we show that perturbation amplification depends strongly on community state in the short term, but this state dependency vanishes in the long term. We illustrate how our framework can provide insights about models and data for communities that are not at equilibrium.

Introduction

Extreme climatic events such as storms, droughts, wildfires and heatwaves are becoming more common and stronger with climate change (Emanuel 2005; Lewis and Karoly 2013; Trenberth et al. 2015). These climatic events can dramatically impact ecological communities such as tropical forests (Brando et al. 2014) and coral reefs (Hughes et al. 2018), where wildfires and heatwaves, respectively, can cause widespread mortality in several species in a short period of time. In ecology, these events are known as pulse perturbations—rapid displacements of species abundances (Bender et al. 1984; Kéfi et al. 2019). Devising effective conservation and management strategies in the face of such perturbations requires broadly applicable theoretical metrics that can be used with population monitoring data.

Most studies on pulse perturbations (hereafter perturbations) assume that populations are displaced from an asymptotically stable equilibrium point (hereafter stable equilibrium point; Bender et al. 1984; Harrison 1979; Holling 1973; May 1973; Neubert and Caswell 1997). If we assume that population dynamics are approximately linear around such an equilibrium point, details of the full dynamics can be ignored, which allows the derivation of stability metrics from dynamical systems theory (May 1973; Perko 2013; Strogatz 2000). Widely used metrics in ecology are resilience (Harrison 1979; Holling 1973; May 1973) and reactivity (Caswell and Neubert 2005; Neubert and Caswell 1997), which quantify the asymptotic (i.e., long time scale) and maximum instantaneous (i.e., short time scale) amplification of perturbed abundances (i.e., perturbation growth rate), respectively. Although these different metrics were at first

considered separately, recent work has introduced a rigorous way to connect them in terms of how the distribution of perturbation amplification changes over time (Arnoldi et al. 2018, 2019). These studies have shown that asymptotic and instantaneous responses can be uncorrelated because they represent the extremes of a continuum of responses. For example, perturbed abundances can dampen in the long term, even though they are amplified in the short term (Arnoldi et al. 2018; Neubert and Caswell 1997). A complete understanding of stability requires metrics that describe not only worst-case responses (e.g., maximum amplification), but also typical responses (e.g., average amplification) at ecologically relevant time scales (Arnoldi et al. 2018, 2019).

While an equilibrium assumption provides mathematical tractability, many natural communities exhibit transient, cyclic or chaotic population dynamics (Hastings et al. 2018; Rogers et al. 2022; Sugihara and May 1990; Turchin 2013). To address this disjunction, ecologists have adopted tools from dynamical systems theory to measure responses to perturbation under such nonequilibrium conditions. For example, Floquet (Funasaki and Kot 1993; Klausmeier 2008) and Lyapunov (Ellner and Turchin 1995) exponents have been introduced to ecology as a way to quantify long-term responses under cyclic and chaotic dynamics, respectively. Ecologists have also developed statistical methods to estimate these exponents from time-series data (Ellner and Turchin 1995; Rogers et al. 2022; Turchin 2013). More recently, studies introduced metrics of short-term responses under nonequilibrium dynamics that go beyond the asymptotic information provided by Floquet and Lyapunov exponents (Cenci and Saavedra 2019; Medeiros et al. 2023; Rogers et al. 2023; Ushio et al. 2018). These studies revealed that, under nonequilibrium dynamics, short-term responses to perturbations depend on community state (i.e., specific combination of species abundances). Because stability metrics are computed along a nonequilibrium trajectory instead of at an equilibrium point, their values change as abundances fluctuate. Thus, the same perturbation can have a different impact on the community depending on when it occurs (e.g., summer versus winter; Rogers et al. 2023; Ushio et al. 2018).

Notwithstanding these advances, we lack a theory for how non-equilibrium communities respond to pulse perturbations that is comparable to the equilibrium theory. Filling this gap would allow us to solve three key problems. First, we do not know whether stability metrics derived for equilibrium points can be used under nonequilibrium conditions. Having a rigorous derivation of nonequilibrium metrics would allow us to understand the main differences between equilibrium and nonequilibrium metrics. Second, we do not have an overarching approach that connects short- and long-term metrics. Developing such an approach would allow us to compare metrics on common ground and to better understand how stability changes across time scales. Finally, we do not have an approach that accommodates a distribution of perturbations. Because there is always uncertainty in how a perturbation will impact a community—for example, which species will be most impacted—we need an approach that describes how a distribution of perturbations changes over time.

Here, we introduce a unified framework to quantify the growth rate of pulse perturbations under nonequilibrium population dynamics. We first show that we can linearize the dynamics about the nonequilibrium trajectory and obtain a sequence of Jacobian matrices that can be integrated into a single state-transition matrix. This state-transition matrix contains all the information necessary to quantify metrics of minimum, typical and maximum perturbation growth rate for a distribution of perturbations at different time scales. By performing simulations under several nonequilibrium scenarios, we demonstrate that these metrics accurately capture the entire range of perturbation outcomes over time. Then, we show that the perturbation growth rate depends on the state of the community for short time scales and that such state dependency vanishes for longer time scales. Finally, we illustrate how the nonequilibrium metrics can provide novel insights about ecological models and be estimated from time-series data.

Population Dynamics Model

Our framework is based on a generic deterministic model for a community with an arbitrary number of species. We consider both continuous- and discrete-time dynamics to highlight connections between stability metrics for these two types of models. The model tracks the abundances of S interacting species, where the vector of abundances at time t is given by $\mathbf{N}(t) = [N_1(t), \dots, N_S(t)]^\top$. In continuous time, the model is given by a set of ordinary differential equations ($i = 1, \dots, S$):

$$\frac{dN_i(t)}{dt} = f_i(N_1(t), \dots, N_S(t)), \quad (1)$$

where f_i is a function describing the rate of change of species i . In discrete time, the model is given by a set of difference equations ($i = 1, \dots, S$):

$$N_i(t + \Delta t) = F_i(N_1(t), \dots, N_S(t)), \quad (2)$$

where F_i is a function describing the change in abundance of species i from t to $t + \Delta t$. Note that f_i and F_i are generally nonlinear functions with multiple parameters that can depend on time (Section S1); we omit this explicit time dependence to simplify the notation. We can write these models in a more compact form as: $d\mathbf{N}(t)/dt = \mathbf{f}(\mathbf{N}(t))$ and $\mathbf{N}(t + \Delta t) = \mathbf{F}(\mathbf{N}(t))$, where $\mathbf{f} = [f_1, \dots, f_S]^\top$ and $\mathbf{F} = [F_1, \dots, F_S]^\top$ are vector-valued functions. The change in abundance of species i in discrete time can be obtained from the continuous-time model by

$$F_i(\mathbf{N}(t)) = N_i(t) + \int_t^{t+\Delta t} f_i(\mathbf{N}(s))ds. \quad (3)$$

We divide population dynamics into two kinds of behaviour: equilibrium and nonequilibrium dynamics. We define equilibrium dynamics as population dynamics close to an equilibrium point \mathbf{N}^* , which satisfies $dN_i(t)/dt = 0 \forall i$ in continuous time or $N_i(t + \Delta t) = N_i(t) \forall i$ in discrete time. In contrast, we define nonequilibrium dynamics as population dynamics away from an equilibrium point, such as when $\mathbf{N}(t)$ changes over time due to transient, cyclic or chaotic dynamics. This broad definition

is commonly used in ecology (DeAngelis and Waterhouse 1987; Klausmeier 2008; McCann 2011; Medeiros et al. 2023; Ushio et al. 2018).

Perturbation Growth Rate

Mathematically, a pulse perturbation is an instantaneous displacement $\mathbf{x}(t_0)$ that moves unperturbed abundances ($\tilde{\mathbf{N}}(t_0)$) to a perturbed state ($\mathbf{N}(t_0)$) at an initial time t_0 : $\mathbf{x}(t_0) = \mathbf{N}(t_0) - \tilde{\mathbf{N}}(t_0)$ (Bender et al. 1984). In most ecological studies, $\tilde{\mathbf{N}}(t_0)$ is assumed to be an equilibrium point ($\tilde{\mathbf{N}}(t_0) = \mathbf{N}^*$; Figure 1). However, $\tilde{\mathbf{N}}(t_0)$ can be any state along a nonequilibrium trajectory (Section S1; Figure 2). The central question about pulse perturbations is whether they will amplify or dampen after some total time $\tau = t_n - t_0$. Therefore, the unifying concept that connects different metrics is the perturbation growth rate (i.e., perturbation amplification), defined as

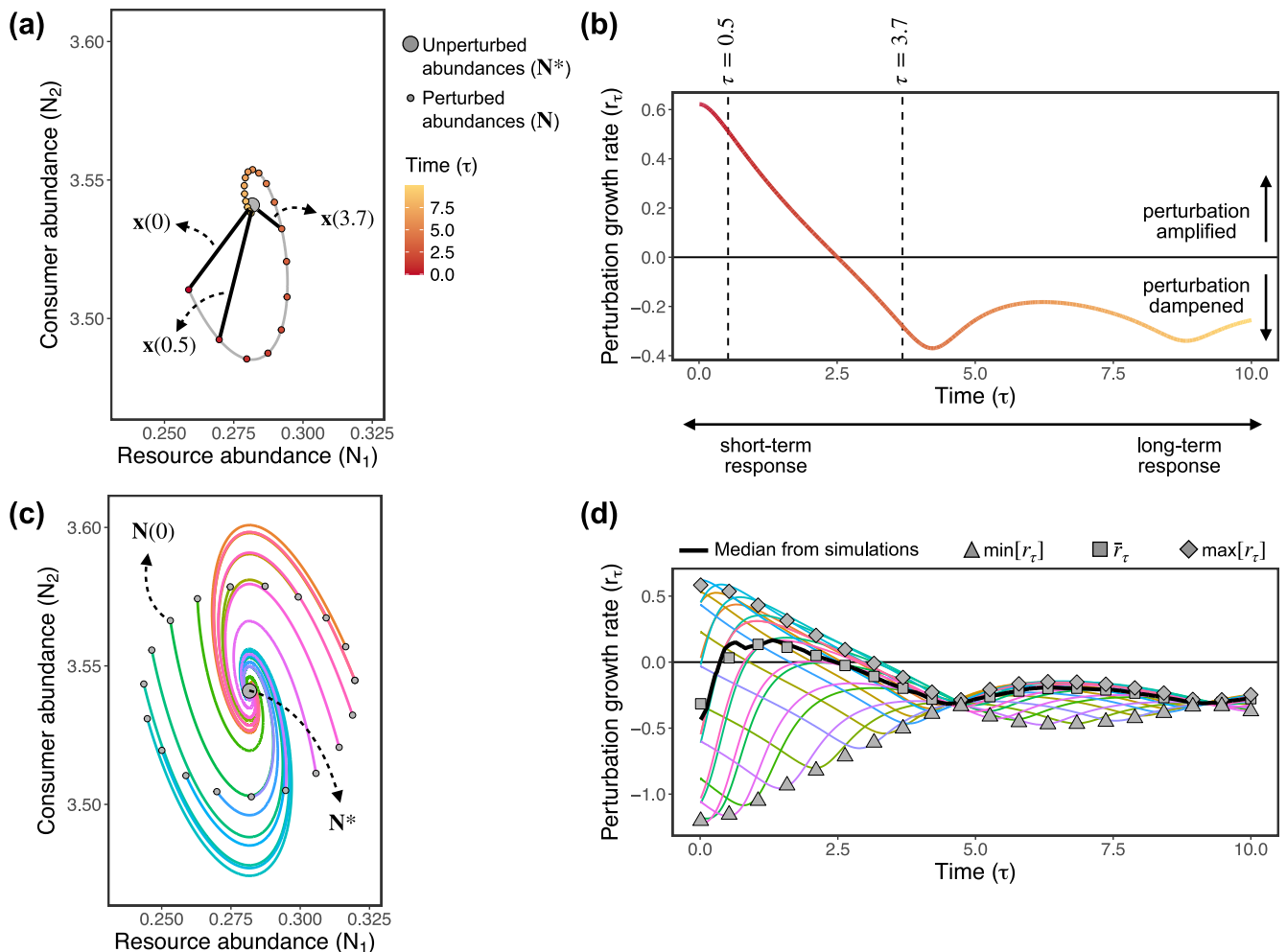


FIGURE 1 | Responses to pulse perturbations for a 2-species resource-consumer model (Equation 24) under equilibrium dynamics. (a) Abundances over time after a perturbation (\mathbf{N} , small coloured points). The large grey point is the equilibrium point $\mathbf{N}^* = [0.28, 3.54]^\top$, whereas the black lines represent the perturbation $\mathbf{x}(\tau)$ at three different times τ . (b) Perturbation growth rate (r_τ) for the perturbation shown in (a). The dashed lines highlight times for which the perturbation size has increased ($\tau = 0.5$) or decreased ($\tau = 3.7$). (c) Abundances over time after 20 perturbations (each coloured line depicts one perturbation). Small grey points are perturbed abundances at $\tau = 0$ ($\mathbf{N}(0)$), where all perturbations have the same initial size (i.e., $\|\mathbf{x}(0)\| = 0.038$) but vary in their direction. (d) Perturbation growth rate (r_τ) for each perturbation shown in (c), where the thick black line corresponds to the median perturbation growth rate. Grey points are the analytical metrics for the minimum ($\min[r_\tau]$, triangles), median (\bar{r}_τ , squares) and maximum ($\max[r_\tau]$, diamonds) perturbation growth rate. Analytical metrics are shown at the same times shown in (a) except for the first point which corresponds to $\tau = 0.01$.

$$r_\tau = \frac{1}{\tau} \log \left[\frac{\|\mathbf{x}(t_n)\|}{\|\mathbf{x}(t_0)\|} \right], \quad (4)$$

where $\|\mathbf{x}(t)\| = \sqrt{\sum_{i=1}^S x_i(t)^2}$ is the Euclidean norm (or size) of the perturbation at time t (Arnoldi et al. 2018). If $r_\tau > 0$, the perturbation grows from t_0 to t_n ; if $r_\tau < 0$, it shrinks (Figures 1 and 2). Note that r_τ measures the average growth rate of a perturbation between t_0 and t_n , which can be different from the instantaneous growth rate of that perturbation at t_n (Arnoldi et al. 2018).

Linear Dynamics of Perturbations

Before analysing the multispecies case, it is worth considering what r_τ represents under single-species dynamics. Let us write

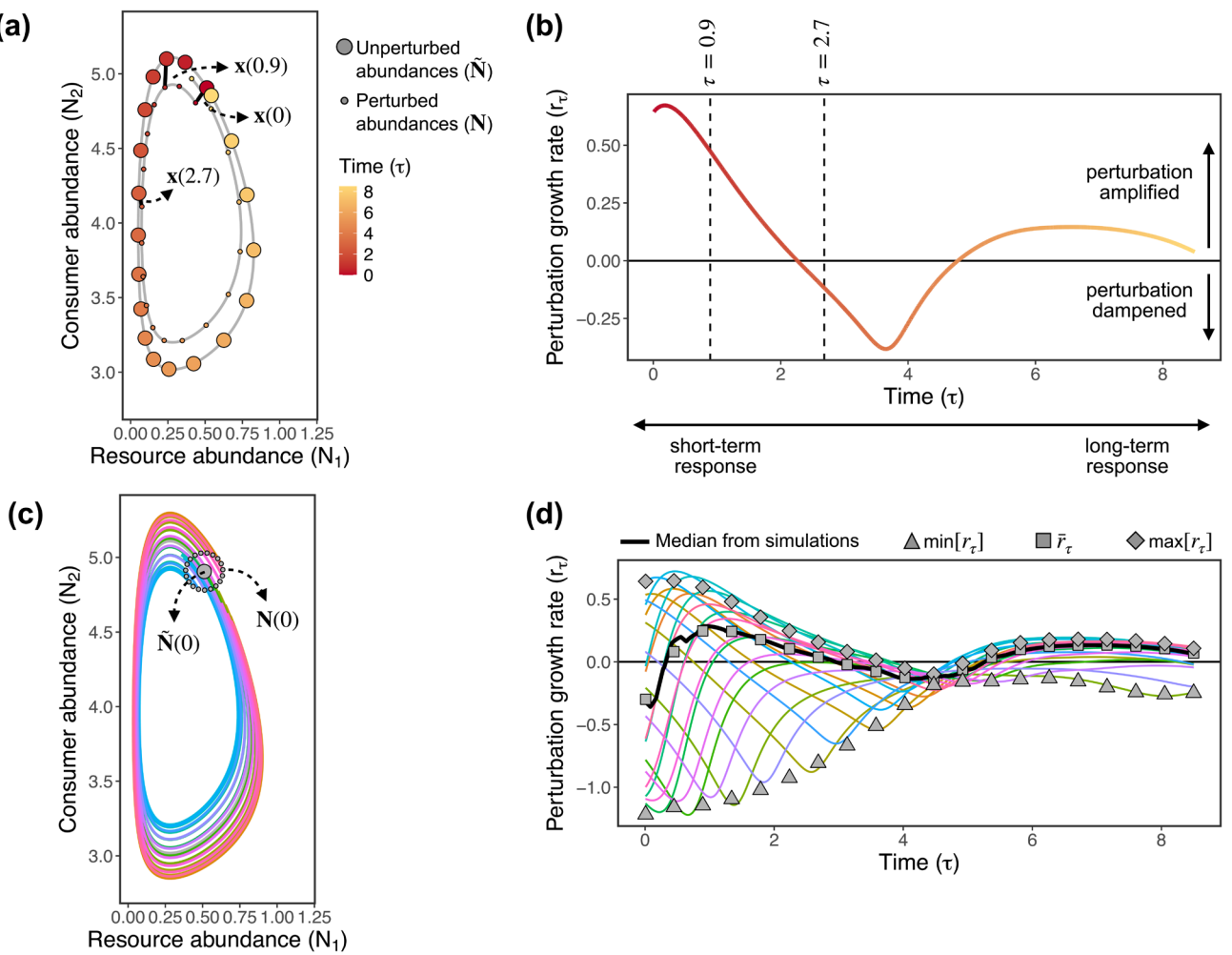


FIGURE 2 | Responses to pulse perturbations for a 2-species resource-consumer model (Equation 24) under nonequilibrium dynamics. (a) Unperturbed ($\tilde{\mathbf{N}}$, large points) and perturbed (\mathbf{N} , small points) abundances after a perturbation. The black lines represent the perturbation $\mathbf{x}(\tau)$ at three different times τ . Unperturbed abundances are on a limit cycle with period $t = 8.5$. (b) Perturbation growth rate (r_τ) for the perturbation shown in (a). The dashed lines highlight times for which the perturbation size has increased ($\tau = 0.9$) or decreased ($\tau = 2.7$). (c) Abundances over time after 20 perturbations (each coloured line depicts one perturbation). Small grey points are perturbed abundances at $\tau = 0$ ($\mathbf{N}(0)$), where all perturbations have the same initial size (i.e., $\|\mathbf{x}(0)\| = 0.263$) but vary in their direction. (d) Perturbation growth rate (r_τ) for each perturbation shown in (c), where the thick black line corresponds to the median perturbation growth rate. Grey points are the analytical metrics for the minimum ($\min[r_\tau]$, triangles), median (\bar{r}_τ , squares) and maximum ($\max[r_\tau]$, diamonds) perturbation growth rate. Analytical metrics are shown at the same times shown in (a) except for the first point which corresponds to $\tau = 0.0085$.

the dynamics of $\mathbf{x}(t)$ in continuous time as $d\mathbf{x}(t)/dt = J_f \mathbf{x}(t)$ and in discrete time as $\mathbf{x}(t + \Delta t) = J_F \mathbf{x}(t)$, where J_f and J_F are scalar parameters. For the total time τ , the growth rate is given by: $r_\tau = \log[\mathbf{x}(\tau)/\mathbf{x}(0)]/\tau = J_f = \log[J_F]/\Delta t$. Thus, by focusing on r_τ , we have a unified criterion for $\mathbf{x}(t)$ to grow ($r_\tau > 0$) or shrink ($r_\tau < 0$) that is independent of the underlying model (i.e., continuous versus discrete time). In what follows, we describe how we can leverage the linear dynamics of $\mathbf{x}(t)$ to derive analytical formulas for r_τ under multispecies dynamics.

If the perturbation $\mathbf{x}(t)$ is sufficiently small, then its dynamics are well-approximated by a set of linear equations even if the dynamics of $\mathbf{N}(t)$ are nonlinear (Perko 2013; Strogatz 2000). Importantly, even if unperturbed ($\tilde{\mathbf{N}}(t)$) and perturbed ($\mathbf{N}(t)$) species abundances are changing in time—that is, $\tilde{\mathbf{N}}(t)$ is not an equilibrium point—the linear approximations remain accurate as long as $\mathbf{x}(t)$ remains small (Section S1). For this reason,

we analyse the linear dynamics of perturbations for the general case of nonequilibrium dynamics and discuss the special case of equilibrium dynamics at the end of this section.

When $\tilde{\mathbf{N}}(t)$ changes over time, the dynamics of $\mathbf{x}(t)$ are given by a set of nonautonomous equations (Section S1). Specifically, the linear model of $\mathbf{x}(t)$ in continuous time is given by

$$\frac{d\mathbf{x}(t)}{dt} = \mathbf{J}_f(t)\mathbf{x}(t) \quad (5)$$

and in discrete time by

$$\mathbf{x}(t + \Delta t) = \mathbf{J}_F(t)\mathbf{x}(t), \quad (6)$$

where $\mathbf{J}_f(t)$ and $\mathbf{J}_F(t)$ are the Jacobian matrices of \mathbf{f} and \mathbf{F} , respectively, evaluated at $\tilde{\mathbf{N}}(t)$. Equations (5) and (6) are obtained via a Taylor expansion of $\mathbf{f}(\mathbf{N}(t))$ and $\mathbf{F}(\mathbf{N}(t))$ around $\tilde{\mathbf{N}}(t)$ (Section S1).

The Jacobian matrix has a central role in stability studies and is defined as the matrix containing all first-order partial derivatives. For the continuous-time model (1),

$$[\mathbf{J}_f]_{ij} = \frac{\partial f_i}{\partial N_j}. \quad (7)$$

For the discrete-time model (2),

$$[\mathbf{J}_F]_{ij} = \frac{\partial F_i}{\partial N_j}. \quad (8)$$

At equilibrium, the Jacobian is a constant matrix evaluated at a fixed state (i.e., \mathbf{N}^*); however, for nonequilibrium dynamics the Jacobian is a time-varying matrix evaluated at a moving state (i.e., $\tilde{\mathbf{N}}(t)$). Note that, if the functions \mathbf{f} or \mathbf{F} are also changing over time (e.g., time-varying parameters), then the Jacobian matrix also needs to incorporate these changes (Section S1).

The solution of the continuous-time approximation (5), from t_0 to t_n , is given by

$$\mathbf{x}(t_n) = \Phi_f(t_n, t_0)\mathbf{x}(t_0), \quad (9)$$

where $\Phi_f(t_n, t_0)$ is the state-transition matrix (often called fundamental matrix) of \mathbf{f} that describes how the system moves from $\mathbf{x}(t_0)$ to $\mathbf{x}(t_n)$ (Antsaklis and Michel 2006; Argyris et al. 2015). For a nonautonomous linear system, $\Phi_f(t_n, t_0)$ integrates the matrix $\mathbf{J}_f(t)$ through time:

$$\Phi_f(t_n, t_0) = \exp \left[\int_{t_0}^{t_n} \mathbf{J}_f(s) ds \right], \quad (10)$$

where $\exp[\mathbf{A}] = \sum_{i=0}^{\infty} \frac{1}{i!} \mathbf{A}^i$ is the exponential of a matrix \mathbf{A} and $\mathbf{J}_f(t)$ is integrated in chronological order (Antsaklis and Michel 2006; Barabás et al. 2012). Because $\Phi_f(t_n, t_0)$ is given by an ordered exponential, we cannot integrate $\mathbf{J}_f(t)$ first and then compute the exponential. There are two ways to resolve this issue and obtain $\Phi_f(t_n, t_0)$. One option is to solve the matrix differential equation

$$\frac{d\Phi_f(t, t_0)}{dt} = \mathbf{J}_f(t)\Phi_f(t, t_0) \quad (11)$$

from t_0 to t_n with $\Phi_f(t_0, t_0) = \mathbf{I}$ (Antsaklis and Michel 2006; Klausmeier 2008). This method, however, depends on having an analytical expression for $\mathbf{J}_f(t)$. A second option is to approximate the solution of Equation (11) with a product of n Jacobian matrices evaluated at sequential states under small time steps (Barabás et al. 2012):

$$\Phi_f(t_n, t_0) \approx \exp[(t_n - t_{n-1})\mathbf{J}_f(t_{n-1})] \cdots \exp[(t_2 - t_1)\mathbf{J}_f(t_1)] \\ \exp[(t_1 - t_0)\mathbf{J}_f(t_0)], \quad (12)$$

where $\mathbf{J}_f(t_i)$ represents the Jacobian matrix evaluated at $\tilde{\mathbf{N}}(t_i)$. If the time step $t_{i+1} - t_i$ is infinitesimal (i.e., $n \rightarrow \infty$), then $\mathbf{J}_f(t_i)$ will be constant between t_i and t_{i+1} and Equation (12) will give

the exact solution. We focus here on the second method, which can be used with estimates of the Jacobian matrix from data without knowing its analytical form (Section S7). For small τ (i.e., short time scale), $\Phi_f(t_n, t_0)$ can be approximated using only the first term in the product: $\Phi_f(t_n, t_0) \approx \exp[\tau \mathbf{J}_f(t_0)]$ (Medeiros et al. 2023; Miki et al. 2025; Munch et al. 2020).

The solution of the discrete-time approximation (6) from t_0 to t_n is given by

$$\mathbf{x}(t_n) = \Phi_F(t_n, t_0)\mathbf{x}(t_0), \quad (13)$$

where $\Phi_F(t_n, t_0)$ is the state-transition matrix of \mathbf{F} (Argyris et al. 2015). Analogously to the continuous-time case, $\Phi_F(t_n, t_0)$ is given by a product of $\tau / \Delta t$ matrices $\mathbf{J}_F(t)$ from t_0 to t_n :

$$\Phi_F(t_n, t_0) = \mathbf{J}_F(t_n - \Delta t) \cdots \mathbf{J}_F(t_0 + \Delta t)\mathbf{J}_F(t_0), \quad (14)$$

where $\mathbf{J}_F(t_i)$ is the Jacobian matrix evaluated at $\tilde{\mathbf{N}}(t_i)$. This product of Jacobian matrices is the exact solution of the linear dynamics (unlike the approximation (12)). Similarly to Equation (3), we can connect the continuous- and discrete-time Jacobian matrices over a time period Δt :

$$\mathbf{J}_F(t) = \exp \left[\int_t^{t+\Delta t} \mathbf{J}_f(s) ds \right]. \quad (15)$$

In the special case where $\Delta t = t_{i+1} - t_i$ is a small time step such that $\mathbf{J}_f(t_i)$ is almost constant between t_i and t_{i+1} , then

$$\mathbf{J}_F(t_i) = \exp \left[\int_{t_i}^{t_{i+1}} \mathbf{J}_f(s) ds \right] \approx \exp[(t_{i+1} - t_i)\mathbf{J}_f(t_i)]. \quad (16)$$

At equilibrium, we only need to consider a constant Jacobian matrix evaluated at \mathbf{N}^* , instead of a sequence of Jacobian matrices as in Equations (12) and (14) (Antsaklis and Michel 2006; Arnoldi et al. 2018; Perko 2013). We denote this matrix as \mathbf{J}_f^* and \mathbf{J}_F^* for continuous and discrete time, respectively. Under continuous time, Equation (9) reduces to

$$\mathbf{x}(t_n) = \exp[\tau \mathbf{J}_f^*] \mathbf{x}(t_0), \quad (17)$$

where $\Phi_f(t_n, t_0) = \exp[\tau \mathbf{J}_f^*]$ is the state-transition matrix. Under discrete time, Equation (13) reduces to

$$\mathbf{x}(t_n) = \mathbf{J}_F^{\tau / \Delta t} \mathbf{x}(t_0), \quad (18)$$

where $\Phi_F(t_n, t_0) = \mathbf{J}_F^{\tau / \Delta t}$ is the state-transition matrix and $\tau / \Delta t$ is the number of Jacobian matrices that are multiplied together.

Equations (12), (14), (17) and (18) demonstrate that going from equilibrium to nonequilibrium dynamics involves simple but key modifications of the state-transition matrix. As shown below, these modifications allow us to investigate several non-equilibrium scenarios with the same stability metrics that can be used for equilibrium dynamics.

Stability Metrics

Details about the dynamics (e.g., continuous versus discrete time, equilibrium versus nonequilibrium) are required to define the state-transition matrix ($\Phi_f(t_n, t_0)$ or $\Phi_F(t_n, t_0)$); but once this matrix is defined, we can derive stability metrics that quantify how $\mathbf{x}(t)$ changes through time irrespective of these details. This occurs because the state-transition matrix completely specifies how $\mathbf{x}(t_0)$ is connected to $\mathbf{x}(t_n)$, analogously to the single-species example described in the beginning of the previous section. To simplify the notation, we will drop the subscript (f or F) and dependence on time (t_n and t_0), and hereafter refer to the state-transition matrix as Φ . We now introduce three metrics that apply under equilibrium and nonequilibrium dynamics for either continuous or discrete time.

The amplification of a given perturbation depends on the initial perturbation direction (i.e., the direction of the vector $\mathbf{x}(t_0)$), which represents how each species is affected by the perturbation (Arnoldi et al. 2018; Medeiros et al. 2023; Neubert and Caswell 1997). However, given that we rarely know a priori what direction a perturbation will have, we treat it as random. Thus, we consider a distribution of perturbations around the unperturbed state $\tilde{\mathbf{N}}(t_0)$ (Arnoldi et al. 2018; Medeiros et al. 2023). Specifically, we assume that $\mathbf{x}(t_0)$ has an arbitrary distribution with mean vector μ_0 and covariance matrix Σ_0 (Figures 1c and 2c). Note that the condition that $\mathbf{x}(t)$ is small implies that the variances in Σ_0 (i.e., diagonal elements) must be small. Our goal is to obtain analytical metrics that are computed using only information on Φ , μ_0 and Σ_0 .

Median Perturbation Growth Rate

We first consider the growth rate of average perturbation sizes, which is given by

$$\bar{r}_\tau = \frac{1}{2\tau} \log \left[\frac{\mathbb{E}[\|\mathbf{x}(t_n)\|^2]}{\mathbb{E}[\|\mathbf{x}(t_0)\|^2]} \right]. \quad (19)$$

For any version of the state-transition matrix Φ defined in the previous section, an arbitrary matrix Σ_0 , and assuming that $\mu_0 = \mathbf{0}$ (see Section S2 for $\mu_0 \neq \mathbf{0}$), \bar{r}_τ is given by

$$\bar{r}_\tau = \frac{1}{2\tau} \log \left[\frac{\text{tr}[\Phi \Sigma_0 \Phi^\top]}{\text{tr}[\Sigma_0]} \right], \quad (20)$$

where $\text{tr}(\mathbf{A})$ denotes the trace of a matrix \mathbf{A} . Although Arnoldi et al. (2018) derived Equation (20) assuming equilibrium dynamics under continuous time, the previous section shows that it is valid for equilibrium and nonequilibrium dynamics under continuous or discrete time given the linear dynamics for $\mathbf{x}(t)$. If perturbations affect each species independently with identical variance (i.e., Σ_0 proportional to the identity matrix), then Equation (20) simplifies to:

$$\bar{r}_\tau = \frac{1}{2\tau} \log \left[\frac{1}{S} \text{tr}[\Phi \Phi^\top] \right]. \quad (21)$$

As suggested by Arnoldi et al. (2018), \bar{r}_τ computed using Equation (20) is an excellent approximation to the median growth rate of the distribution of perturbations. That is, even though \bar{r}_τ does not correspond to the mean of r_τ (i.e., $\mathbb{E}[r_\tau]$), it does accurately capture the median of r_τ . We show that this result can be understood based on properties of the median of a random variable (Section S2). Hereafter, we refer to \bar{r}_τ as the median perturbation growth rate.

Maximum and Minimum Perturbation Growth Rate

Although \bar{r}_τ informs us about the typical response of the community to perturbations, it is also useful to know about worst- and best-case scenarios. For stable equilibrium points, reactivity measures the maximum instantaneous (i.e., $\tau \rightarrow 0$) amplification over all possible perturbation directions (Caswell and Neubert 2005; Neubert and Caswell 1997). Such maximum amplification can also be computed for any time scale τ (Nazerian et al. 2024; Neubert and Caswell 1997). The discrete-time version of reactivity is given by the log of the largest singular value of \mathbf{J}_F^* (Caswell and Neubert 2005), which is equivalent to the largest finite-time Lyapunov exponent (Nazerian et al. 2024). We propose that, by using Φ instead of \mathbf{J}_F^* , we can compute the maximum perturbation growth rate for nonequilibrium dynamics as (Section S2)

$$\max_{\mathbf{x}(t_0) \neq \mathbf{0}} [r_\tau] = \frac{1}{\tau} \log [\sigma_1(\Phi)], \quad (22)$$

where the maximum is considered over all nonzero initial perturbations $\mathbf{x}(t_0)$ and the i th singular value of a matrix \mathbf{A} is equivalent to the square root of the i th eigenvalue of $\mathbf{A}\mathbf{A}^\top$ (i.e., $\sigma_i(\mathbf{A}) = \sqrt{\lambda_i(\mathbf{A}\mathbf{A}^\top)}$). An $S \times S$ matrix has S singular values ($\sigma_S \leq \dots \leq \sigma_1$), which are all real numbers. Similarly, the minimum perturbation growth rate can be calculated with the smallest singular value of Φ (Section S2):

$$\min_{\mathbf{x}(t_0) \neq \mathbf{0}} [r_\tau] = \frac{1}{\tau} \log [\sigma_S(\Phi)]. \quad (23)$$

To simplify the notation, hereafter we use $\max[r_\tau]$ and $\min[r_\tau]$ to denote the maximum and minimum perturbation growth rate. Importantly, in contrast to \bar{r}_τ , $\max[r_\tau]$ and $\min[r_\tau]$ do not depend on how perturbations are distributed (i.e., μ_0 and Σ_0).

Connections Among Metrics

Taken together, \bar{r}_τ , $\max[r_\tau]$ and $\min[r_\tau]$ characterise the entire range of responses to perturbation for any time scale τ . These metrics also have a geometric meaning in terms of Φ deforming an initial ball of $\mathbf{x}(t_0)$ vectors (specified by Σ_0) into an ellipsoid of $\mathbf{x}(t_n)$ vectors (Figures 1c and 2c; Argyris et al. (2015); Datseris and Parlitz (2022); Geist et al. (1990)). This ellipsoid represents the covariance matrix of the distribution of perturbations after τ time steps, which is given by $\Phi \Sigma_0 \Phi^\top$ (Section S2). The major and minor axes of the ellipsoid correspond to the perturbations that grew at a rate given by $\max[r_\tau]$ and $\min[r_\tau]$, respectively. Because the trace of a matrix

is the sum of its eigenvalues, from Equation (21) we have that \bar{r}_τ represents the average of all squared singular values of Φ (i.e., average of ellipsoid axes). We can also decompose \bar{r}_τ into contributions of different species, allowing us to understand how responses of individual species shape whole-community response (Medeiros et al. 2023; Medeiros and Saavedra 2023). Specifically, the i th diagonal element of $\Phi \Sigma_0 \Phi^\top$ contains the contribution of species i to \bar{r}_τ or, alternatively, the sensitivity of species i to perturbations (Medeiros et al. 2023; Medeiros and Saavedra 2023).

We show that previously proposed metrics such as the largest eigenvalue (Rogers et al. 2023; Ushio et al. 2018) and determinant (Cenci and Saavedra 2019; Medeiros and Saavedra 2023) of Φ are approximations to $\max[r_\tau]$ and \bar{r}_τ , respectively (Section S3). Note that these previous studies have not explicitly used the concept of a state-transition matrix. We also demonstrate how time-delay embedding (i.e., Takens' Theorem), often used when inferring stability metrics from abundance time series (Rogers et al. 2022, 2023), affects the eigenvalues and singular values of Φ (Section S4). We show that $\max[r_\tau]$ computed under delay coordinates will only be close to $\max[r_\tau]$ of the full system for a large τ . For small τ , the largest eigenvalue of Φ under delay coordinates is a lower bound to $\max[r_\tau]$.

Illustration of Stability Metrics

Equilibrium Case

Following Arnoldi et al. (2018), we illustrate the application of \bar{r}_τ , $\max[r_\tau]$ and $\min[r_\tau]$ to perturbations of the stable equilibrium of the Rosenzweig-MacArthur model (Rosenzweig and MacArthur 1963):

$$\begin{aligned} \frac{dN_1}{dt} &= N_1 \left[r \left(1 - \frac{N_1}{K} \right) - \frac{aN_2}{b+N_1} \right] \\ \frac{dN_2}{dt} &= N_2 \left[\frac{eaN_1}{b+N_1} - d \right], \end{aligned} \quad (24)$$

where N_1 is the abundance of the resource species and N_2 is the abundance of the consumer species (see Table S1 for parameter details). This model exhibits a Hopf bifurcation at $K_H = -b(d+ae)/(d-ae)$, such that abundances settle to a unique stable equilibrium point when $K < K_H$ and to a limit cycle when $K > K_H$.

We first quantified the growth rate (r_τ ; Equation 4) of a single perturbation as abundances $\mathbf{N}(t)$ return to the equilibrium point \mathbf{N}^* from $t = 0$ to $t = 10$ (Figure 1a). Although perturbed abundances grow in the short term (e.g., $r_\tau > 0$ for $\tau = 0.5$), they eventually shrink in the long term (e.g., $r_\tau < 0$ for $\tau = 3.7$; Figure 1b). However, r_τ depends on the initial direction of the perturbation. For a uniform distribution of perturbations around \mathbf{N}^* (Figure 1c), r_τ varies widely across perturbations at short time scales (e.g., $-1.23 \leq r_\tau \leq 0.62$ for $\tau = 0.01$), but exhibits much less variation at long time scales (e.g., $-0.37 \leq r_\tau \leq -0.25$ for $\tau = 10$; Figure 1d). This long-term response is captured by resilience, which is quantified as the real part of the largest eigenvalue of \mathbf{J}_f^* : $\lambda_1(\mathbf{J}_f^*) = -0.31$. Because resilience is independent

of the initial perturbation direction, \bar{r}_τ and $\max[r_\tau]$ converge to $\lambda_1(\mathbf{J}_f^*)$ as $\tau \rightarrow \infty$ (Arnoldi et al. (2018); far right of Figure 1d). In contrast to resilience, $\min[r_\tau]$, \bar{r}_τ and $\max[r_\tau]$ accurately capture the minimum, median and maximum perturbation growth rate across all simulated perturbations and for all time scales (Figure 1d).

Nonequilibrium Case

If the resource carrying capacity (K) in the Rosenzweig-MacArthur model (24) is sufficiently large, the consumer and resource populations fluctuate periodically in time; they co-exist on a limit cycle. For nonequilibrium dynamics like these, r_ξ (Equation 4) measures the difference between unperturbed ($\tilde{\mathbf{N}}(t)$) and perturbed ($\mathbf{N}(t)$) abundances as they change in parallel through time (Figure 2a). We first calculated r_τ of a single perturbation over an entire cycle period from $t = 0$ to $t = 8.5$. For this particular perturbation, $\tilde{\mathbf{N}}(t)$ and $\mathbf{N}(t)$ can be farther apart (e.g., $r_\tau > 0$ for $\tau = 0.9$) or closer together (e.g., $r_\tau < 0$ for $\tau = 2.7$) depending on τ (Figure 2b). In contrast to stable equilibrium points (Figure 1b), a perturbation under nonequilibrium dynamics can be larger than its initial size long after it first impacted the community (e.g., Figure 2b at $\tau = 6$). Next, we analysed how r_τ varies over a distribution of perturbations (Figure 2c). As in the equilibrium case (Figure 1), we found a large variation in r_τ at short time scales (e.g., $-1.13 \leq r_\tau \leq 0.64$ for $\tau = 0.0085$), but not at long time scales (e.g., $-0.25 \leq r_\tau \leq 0.12$ for $\tau = 8.5$; Figure 2d). For large τ , \bar{r}_τ and $\max[r_\tau]$ converge to the largest Floquet exponent (far right of Figure 2d). However, focusing solely on this asymptotic behaviour ignores the response of the community on ecologically relevant time scales. The metrics introduced here accurately capture the minimum, median and maximum perturbation growth rate for all time scales (Figure 2d).

Accuracy of Stability Metrics

Having illustrated the metrics under equilibrium (Figure 1) and nonequilibrium (Figure 2) dynamics, we next assessed their accuracy under two continuous-time models: the Rosenzweig-MacArthur model (Equation 24) and the Hastings-Powell model (Hastings and Powell 1991),

$$\begin{aligned} \frac{dN_1}{dt} &= N_1 \left[r \left(1 - \frac{N_1}{K} \right) - \frac{a_1 N_2}{b_1 + N_1} \right] \\ \frac{dN_2}{dt} &= N_2 \left[\frac{e_1 a_1 N_1}{b_1 + N_1} - d_1 - \frac{a_2 N_3}{b_2 + N_2} \right] \\ \frac{dN_3}{dt} &= N_3 \left[\frac{e_2 a_2 N_2}{b_2 + N_2} - d_2 \right]. \end{aligned} \quad (25)$$

In system (25), N_1 is the abundance of the resource species, N_2 is the abundance of the consumer species, and N_3 is the abundance of the top predator (see Table S1 for parameter details). We demonstrate the accuracy of the stability metrics with two discrete-time models in Section S5.

For each continuous-time model, we explored two scenarios. Each scenario represents a different type of ecological dynamics:

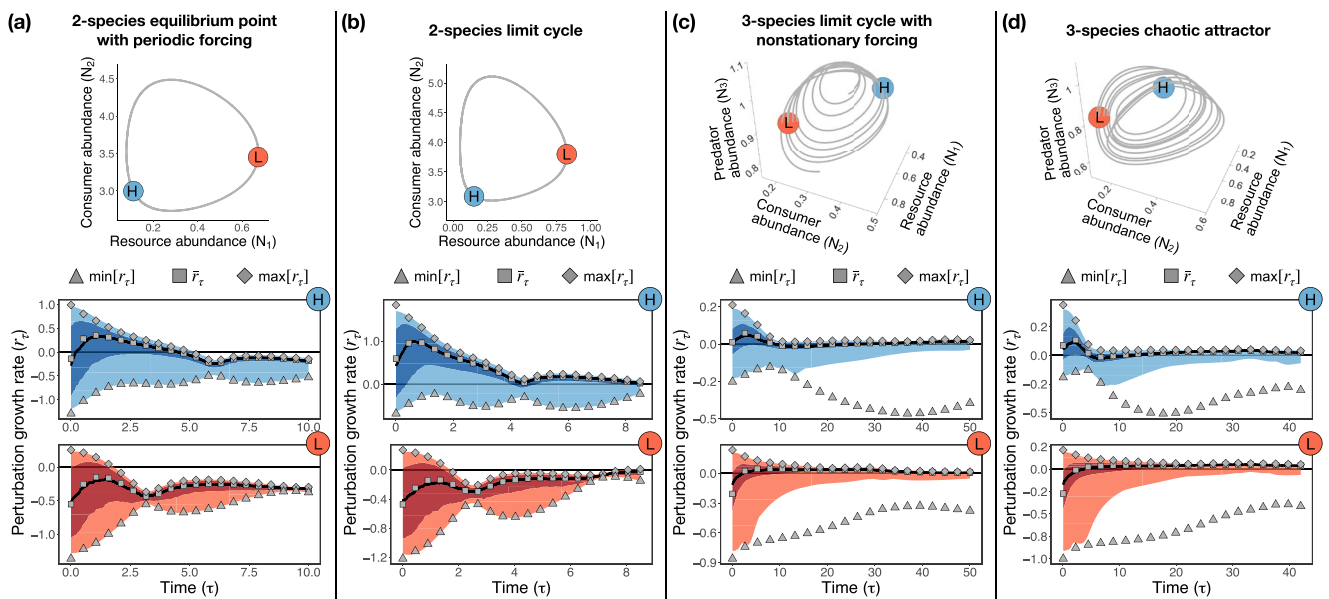


FIGURE 3 | Accuracy of stability metrics across four different nonequilibrium scenarios. Each column (a–d) depicts a scenario, where the top plot shows the trajectory of unperturbed abundances ($\tilde{\mathbf{N}}(t)$, grey line) and the two bottom plots show the outcome of simulated perturbations (blue and red shades) together with the stability metrics as grey points ($\min[r_\tau]$, \bar{r}_τ and $\max[r_\tau]$). Points labelled as H (in blue) and L (in red) represent locations along the trajectory with high and low values of \bar{r}_τ (for small τ), respectively. In bottom plots, the dark shade denotes the region between the 25th and 75th percentiles, whereas the light shade goes to the minimum and maximum values of r_τ . These percentiles are shown as a way to convey the shape of the distribution of r_τ . Note this distribution has a very long tail when τ is large and it becomes extremely unlikely to observe a perturbation with a growth rate given by $\min[r_\tau]$ such as in (c) and (d). Bottom plots span $\tau = 0$ to $\tau = T$, where T denotes the recurrence time of the system. (a) Scenario 1: Rosenzweig-MacArthur model under an equilibrium point with a periodically changing carrying capacity (K). (b) Scenario 2: Rosenzweig-MacArthur model under a limit cycle with fixed parameters (same as Figure 2). (c) Scenario 3: Hastings-Powell model under a limit cycle with a linear trend in predator attack rate (a_2). (d) Scenario 4: Hastings-Powell model under a chaotic attractor with fixed parameters.

1. *Cyclic dynamics driven by environmental forcing* (e.g., seasonal productivity) (Figure 3a). We used the Rosenzweig-MacArthur model (Equation 24) with parameters that, all else equal, would generate a stable equilibrium point, but with periodic forcing of the carrying capacity K (Bieg et al. 2023). This scenario corresponds to Figure 1, but with $K(t) = K_0 + A \sin(p2\pi t)$, where K_0 is the average, A is the amplitude, and $1/p$ is the period of K .
2. *Cyclic dynamics driven by nonlinear species interactions* (Figure 3b). We used the Rosenzweig-MacArthur model (Equation 24) with fixed parameters that generate a limit cycle. This scenario corresponds to Figure 2.
3. *Nonstationary cyclic dynamics driven by nonlinear species interactions and environmental forcing* (e.g., gradual warming) (Figure 3c). We used the Hastings-Powell model (Equation 25) with a linear trend in the top predator attack rate (a_2). Specifically, we set $a_2(t) = \alpha + \beta t$, where α is the baseline and β is the rate of change of a_2 .
4. *Chaotic dynamics driven by nonlinear species interactions* (Figure 3d). We used the Hastings-Powell model (Equation 25) with fixed parameters that generate a chaotic attractor.

For each scenario, we first generated an unperturbed trajectory of species abundances $\{\tilde{\mathbf{N}}(t)\}$, $t = 0, \dots, cT$, where T is the recurrence time of the system and c is the number of recurrences. The recurrence time is a generalisation of the period of cyclic

dynamics and was computed as $T = 1/f_{\max}$, where f_{\max} is the frequency with maximum power obtained from the power spectrum of the abundance time series (Gilpin 2023). We used $c = 1$ for scenarios 1 and 2, $c = 7$ for scenario 3 and $c = 9$ for scenario 4. We computed the three metrics ($\min[r_\tau]$, Equation (23); \bar{r}_τ , Equation (20); and $\max[r_\tau]$, Equation (22)) from the analytical Jacobian matrix of each system evaluated along the unperturbed trajectory. Then, we selected states with high and low \bar{r}_τ in the short term (i.e., small τ) as a way to explore two distinct behaviours along each trajectory (top panels in Figure 3).

For each of the two selected states, we applied $m = 500$ perturbations $\mathbf{x}(t_0)$ around unperturbed abundances (i.e., $\tilde{\mathbf{N}}(t_0)$), where $x_i(t_0)$ was sampled from a standard normal distribution for each species i . We then scaled $\mathbf{x}(t_0)$ to have norm δ (i.e., $\|\mathbf{x}(t_0)\| = \delta$). This guaranteed that the m perturbed abundances $\mathbf{N}(t_0)$ were uniformly distributed on a hypersphere with radius δ centered on $\tilde{\mathbf{N}}(t_0)$. Next, we evolved perturbed abundances in time and computed r_τ at different τ (Figure S1). We set δ as 5% of the average standard deviation of abundances and obtained similar results with larger perturbations (Figure S2). We also performed simulations where $\mathbf{N}(t_0)$ was not uniformly distributed (i.e., Σ_0 not proportional to the identity matrix). As expected, the accuracy of \bar{r}_τ is lower in these simulations, especially for small τ , but it has no effect on the accuracy of $\min[r_\tau]$ and $\max[r_\tau]$ (Figure S3).

The stability metrics accurately captured the amplification of simulated perturbations in all four scenarios (Figure 3).

For example, the plot labelled H (i.e., high short-term \bar{r}_τ) for the Rosenzweig-MacArthur model with a limit cycle (scenario 2, Figure 3b) shows that, at $\tau = 0.0085$, the distribution of r_τ from simulations has the following properties: minimum = −0.64, median = 0.42 and maximum = 1.69. The analytical metrics at $\tau = 0.0085$ accurately captured these properties: $\min[r_\tau] = -0.68$, $\bar{r}_\tau = 0.60$ and $\max[r_\tau] = 1.84$. We obtained results with similar accuracy across all scenarios (i.e., columns of Figure 3), for both locations along the trajectory (i.e., plots labelled H and L in Figure 3) and for all time scales (i.e., different values of τ). We also computed Φ_f using a large time step $t_{i+1} - t_i$ to test the accuracy of approximation (12). We obtained qualitatively similar results, but $\max[r_\tau]$ and \bar{r}_τ were overestimated, whereas $\min[r_\tau]$ was underestimated for small τ (Figure S4). The analytical metrics also closely matched simulations under two discrete-time models (Figure S5). The apparent discrepancy between $\min[r_\tau]$ and the minimum growth rate observed in the simulations is a result of the long-tailed distribution of r_τ for large τ (Figure S6). Especially for a large number of species, it becomes very unlikely to observe a perturbation growth rate given by $\min[r_\tau]$ because almost all perturbations will grow according to $\max[r_\tau]$ when τ is large. Thus, although $\min[r_\tau]$ is an informative metric at short time scales, it becomes less relevant at long time scales.

Importantly, two other metrics (largest eigenvalue and determinant of Φ) that have been proposed to measure responses to perturbations under nonequilibrium dynamics (Cenci and Saavedra 2019; Medeiros and Saavedra 2023; Rogers et al. 2023; Ushio et al. 2018) cannot capture the entire pattern of Figure 3 (Figures S7 and S8). For instance, we are only able to approximate the asymptotic behaviour of r_τ (i.e., for large τ) when using the largest eigenvalue of Φ instead of its largest singular value (Figure S7).

There are two main insights that can be obtained from Figure 3. First, the response of the community greatly depends on the perturbation direction for small τ . That is, r_τ can almost always be positive or negative depending on choice of perturbation direction. Nevertheless, within a given scenario (i.e., column of Figure 3), the likelihood of a positive or negative r_τ changes dramatically depending on when perturbations occur (e.g., H versus L panels). The metrics allow us to quantify such likelihood for any state along a trajectory. Second, our results show that this large variability in r_τ for small τ vanishes as τ becomes large. That is, for large τ , \bar{r}_τ and $\max[r_\tau]$ converge to the same value. Thus, analogously to stable equilibrium points (Figure 1), the sum of singular values (i.e., \bar{r}_τ) converges to the largest singular value (i.e., $\max[r_\tau]$) for large τ .

Responses to Perturbations From Short to Long Time Scales

We now focus on the median perturbation growth rate (\bar{r}_τ) and investigate how it changes along a trajectory as a function of τ —that is, as we move from short to long time scales (Figure S9 shows results with $\max[r_\tau]$). For this analysis, we computed \bar{r}_τ for many points along each unperturbed nonequilibrium trajectory (i.e., $\{\tilde{N}(t)\}$, $t = 0, \dots, cT$) generated from the

Rosenzweig-MacArthur or Hastings-Powell model. We then quantified \bar{r}_τ for three τ values: (1) 2% of the recurrence time ($\tau = 0.02T$), (2) 20% of the recurrence time ($\tau = 0.2T$), and (3) 80% of the recurrence time ($\tau = 0.8T$).

At short time scales, \bar{r}_τ shows strong state dependency across all scenarios (top panels in Figure 4). That is, whether perturbations will typically be amplified ($\bar{r}_\tau > 0$) or damped ($\bar{r}_\tau < 0$) depends on the location along the trajectory where the initial perturbation occurs. For example, when population cycles are the result of a periodically changing carrying capacity (K), a perturbation will typically be amplified in the short term if it affects the community when the resource species has low abundance (i.e., low K), while the perturbation will typically be damped if it affects the community when this species has high abundance (i.e., high K ; Figure 4a). We also investigated other previously proposed metrics under this short time scale (Section S3). We found that the largest eigenvalue of Φ cannot describe the state-dependent patterns of $\max[r_\tau]$ (Figure S10). In contrast, the determinant of Φ is able to approximate the state-dependent patterns of \bar{r}_τ (Figure S11). For small τ , the determinant of $\Phi \approx \exp[\tau \mathbf{J}_f(t_0)]$ is connected to the trace of $\mathbf{J}_f(t_0)$ (Medeiros and Saavedra 2023) and measures the expansion rate of a volume of perturbed abundances (Cenci and Saavedra 2019).

The state dependency observed under short time scales vanishes when we consider a long time scale (bottom panels in Figure 4). As τ approaches the recurrence time of the system, \bar{r}_τ (and $\max[r_\tau]$; Figure S9) converges to a single value (approximately the largest Floquet or Lyapunov exponent) regardless of where the initial perturbation occurs. This value is zero for a limit cycle and greater than zero for a chaotic attractor. Such analysis informs us whether perturbations will dampen (e.g., scenario 1; Figure 4a) or amplify (i.e., scenario 4; Figure 4d) on long time scales. However, as also suggested in Figure 3, solely focusing on an asymptotic analysis misses the state-dependent pattern of responses to perturbations. Because short and long time scales are the extremes of a continuum, it is insightful to analyse the rate of convergence of \bar{r}_τ (and $\max[r_\tau]$) to a single value as τ increases. We found that this convergence is faster under the forced equilibrium point (scenario 1) and slower under chaotic dynamics (scenario 4; Figure S12).

The stability metrics also provide new insights when analysing ecological models with transitions from equilibrium to nonequilibrium dynamics. We explored how parameter changes in the Rosenzweig-MacArthur model (Equation 24) impact \bar{r}_τ as the attractor shifts from an equilibrium point to a limit cycle (i.e., Hopf bifurcation; Section S6). Because \bar{r}_τ applies to both equilibrium and nonequilibrium dynamics, it allows us to study how perturbations amplify on both sides of the Hopf bifurcation. We found that increasing K and r beyond the Hopf bifurcation intensifies perturbation amplification at a specific location along the limit cycle, potentially increasing extinction risk for both species (Figure S13).

Discussion

Understanding how pulse perturbations impact ecological communities is a critical research avenue in the context of

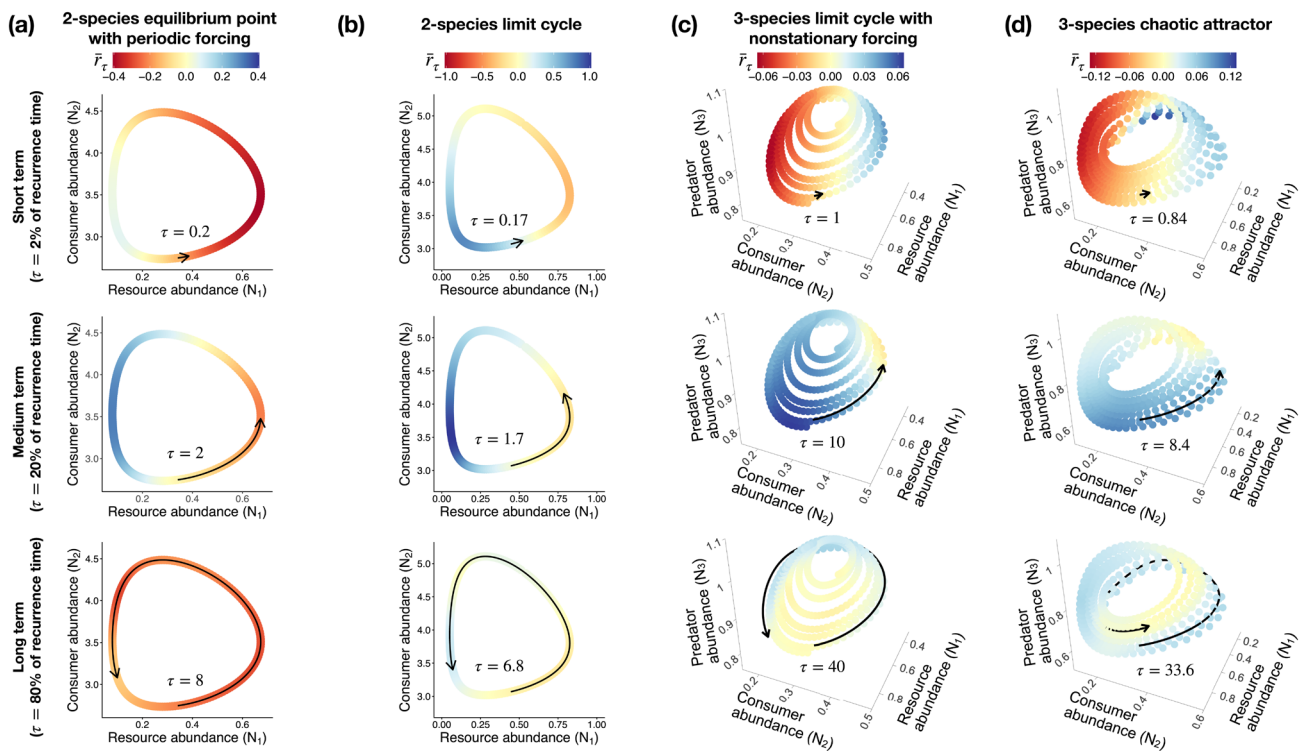


FIGURE 4 | Impact of time scale (τ) on responses to pulse perturbations across four different nonequilibrium scenarios. Each column (a–d) depicts a scenario and each row depicts a time scale (short, medium and long time scales). Time scales are defined in terms of the recurrence time T of the system, where short corresponds to $\tau = 0.02T$, medium corresponds to $\tau = 0.2T$ and long corresponds to $\tau = 0.8T$. Each coloured point in each plot denotes a given unperturbed state ($\tilde{\mathbf{N}}(t)$) along a trajectory at which we compute the median perturbation growth rate (\bar{r}_τ). A red point indicates that perturbations typically dampen ($\bar{r}_\tau < 0$), whereas a blue point indicates that perturbations typically amplify ($\bar{r}_\tau > 0$) at that state. Black arrows in each plot indicate the time scale τ . (a) Scenario 1: Rosenzweig-MacArthur model under an equilibrium point with a periodically changing carrying capacity (K). (b) Scenario 2: Rosenzweig-MacArthur model under a limit cycle with fixed parameters (same as Figure 2). (c) Scenario 3: Hastings-Powell model under a limit cycle with a linear trend in predator attack rate (a_2). (d) Scenario 4: Hastings-Powell model under a chaotic attractor with fixed parameters.

ongoing global change. We introduced a framework to characterise responses to perturbations for nonequilibrium dynamics, from forced equilibrium points to chaotic attractors. To do so, we leveraged known results from dynamical systems theory that are rarely used by ecologists (e.g., Equations 9–14). Our framework unifies existing results for responses of communities at equilibrium (Arnoldi et al. 2018; May 1973; Neubert and Caswell 1997) with the limited results for communities not at equilibrium (Cenci and Saavedra 2019; Ellner and Turchin 1995; Klausmeier 2008; Medeiros et al. 2023). Using perturbation amplification (i.e., perturbation growth rate) as a unifying concept, we derived three key metrics ($\min[r_\tau]$, \bar{r}_τ and $\max[r_\tau]$) and demonstrated their accuracy with simulations (Figure 3). We also obtained novel insights from these metrics regarding the time scale of responses (Figure 4). Finally, we illustrated how to estimate nonequilibrium stability metrics from time series (Box 1; Figure 5). Below, we discuss three main contributions of our study and potential future directions.

First, we determined the conditions under which metrics derived for equilibrium dynamics can be used for nonequilibrium dynamics. We showed that the state-transition matrix (Φ) contains all the necessary information to compute $\min[r_\tau]$, \bar{r}_τ and $\max[r_\tau]$ irrespective of whether the dynamics are at equilibrium. Simplified versions of these metrics, however, can only be used

under certain conditions. For instance, for both equilibrium and nonequilibrium dynamics, the largest eigenvalue of Φ measures perturbation amplification only on long time scales (Figure S7; Arnoldi et al. 2018)). On short time scales, the largest eigenvalue serves as a lower bound to the largest singular value (Section S3; Rogers et al. 2023), but misses important state-dependent patterns of perturbation amplification (Figure S10). In contrast, the metrics derived here accurately characterise perturbation amplification on any time scale.

Second, we established connections between short- and long-term responses to perturbations. Previous work has established connections across time scales for communities at equilibrium (Arnoldi et al. 2018, 2019). However, for time-varying systems such connections can only be found in the dynamical systems literature (e.g., Argyris et al. 2015; Aurell et al. 1997; Geist et al. 1990; Nazerian et al. 2024). Building on these results, we showed that $\min[r_\tau]$, \bar{r}_τ and $\max[r_\tau]$ can be quantified at any time (τ) after the perturbation. This allowed us to explore how the dependence on state decays from short to long time scales (Figure 4 and Figure S12). Ecologically, our results indicate that the same perturbation can have different impacts depending on when it happens, but only on short time scales (Rogers et al. 2023; Ushio et al. 2018). For example, for organisms with seasonal population cycles, the outcome after a few weeks would

BOX 1 | Inferring nonequilibrium stability metrics from abundance time series.

Statistical approaches to infer stability metrics from abundance time-series data (e.g., Cenci and Saavedra 2019; Grziwotz et al. 2023; Hampton et al. 2013; Ives et al. 2003; Medeiros et al. 2023; Nguyen et al. 2025; Rogers et al. 2023; Ushio et al. 2018) use regression models to infer the Jacobian matrix and then compute stability metrics by making minimal assumptions about the underlying population dynamics. Here, we show that we can accurately infer nonequilibrium stability metrics using a local regression model with state-dependent weights (S-map model; Deyle et al. (2016); Sugihara (1994)) adapted for continuous-time dynamics (see Section S7 for details).

We assume that population dynamics are given by $dN_i/dt = f_i(\mathbf{N}(t)) = N_i g_i(\mathbf{N}(t))$. If sampling time intervals are small compared to the generation time of the organisms (Munch et al. 2020) and we have time-series data $\{\mathbf{N}(t)\}$ ($t = 0, 1, \dots, T$), we can fit the following linear regression model to g_i (Stein et al. 2013; Suzuki et al. 2017):

$$g_i(\mathbf{N}(t)) \approx \log \left[\frac{N_i(t+1)}{N_i(t)} \right] = \beta_{i0} + \sum_{j=1}^S \beta_{ij} N_j(t) + \epsilon_i(t), \quad (26)$$

where β_{ij} ($j = 0, \dots, S$) are the model coefficients and $\epsilon_i(t)$ is the error at time t . The units for estimated coefficients and stability metrics is 1/interval, which should be converted to standard units (1/time or 1/generation) for comparison across studies. To simplify the notation, we use $\mathbf{N}(t)$ to denote observations of the unperturbed abundances (previously denoted as $\tilde{\mathbf{N}}(t)$). Equation (26) can also be implemented with time-delay embedding (Rogers et al. 2022, 2023). To account for nonlinearities in g_i , we can fit Equation (26) separately for each focal time t^* , assigning weights $w(t)$ based on the distance between $\mathbf{N}(t)$ and $\mathbf{N}(t^*)$ (Deyle et al. 2016). We then obtain the Jacobian matrix evaluated at $\mathbf{N}(t^*)$ by leveraging the assumed continuous-time dynamics (Song and Saavedra 2021):

$$\left[\hat{\mathbf{J}}_f \right]_{ij}(t^*) = \frac{\partial \hat{f}_i}{\partial N_j}(t^*) = \begin{cases} \hat{\beta}_{ij}(t^*) N_i(t^*) + \hat{g}_i(\mathbf{N}(t^*)), & \text{if } i=j \\ \hat{\beta}_{ij}(t^*) N_i(t^*), & \text{if } i \neq j \end{cases}. \quad (27)$$

Finally, we compute the state-transition matrix at t^* for a given time scale τ as $\hat{\Phi} \approx \exp[\hat{\mathbf{J}}_f(t^* + \tau)] \dots \exp[\hat{\mathbf{J}}_f(t^*)]$, which we use to compute stability metrics.

To showcase this statistical approach, we generated time series $\{\mathbf{N}(t)\}$ ($t = 0, 1, \dots, 149$) from the Rosenzweig-MacArthur model with process and observational noise (Section S7; Figure 5a). Then, we performed leave-future-out cross-validation to determine hyperparameters and fitted the regression model to the entire time series to estimate \bar{r}_τ at every time t^* (Figure 5b). The pattern of the estimated \bar{r}_τ over time closely matched the pattern of the true \bar{r}_τ (i.e., calculated using Equation 24; Figure 5c). Our results were similar, albeit slightly less accurate, when using the standard S-map model (Figure S14) and for time series generated with the Hastings-Powell model (Figures S15 and S16).

depend on when the disturbance occurred (e.g., summer or winter; top panel in Figure 4a,b). However, the outcome after an entire year would not depend on when the disturbance happened (bottom panel in Figure 4a,b).

Third, we described the full range of amplification possibilities by considering a distribution of perturbations. On long time scales, almost all perturbations have the same growth rate (e.g., resilience), allowing us to ignore their initial distribution. In contrast, on short time scales, there is a wide range of outcomes depending on the initial distribution (Figures 1 and 2). Our framework admits uncertainty in how perturbations affect a community (Arnoldi et al. 2018; Medeiros et al. 2023), allowing us to derive metrics for typical (median) and extreme (minimum and maximum) outcomes. We also found that, although information about the initial distribution of perturbations (i.e., μ_0 and Σ_0) is needed to quantify \bar{r}_τ , it is not required to compute $\min[r_\tau]$ and $\max[r_\tau]$. Therefore, \bar{r}_τ has to be interpreted as the typical perturbation amplification conditioned on a specific distribution of perturbations. Future studies can use all three metrics as a way to describe multiple possible perturbation outcomes.

Our findings suggest several possibilities for future theoretical and empirical studies on nonequilibrium population dynamics. Regarding theoretical work, the metrics we developed allow exploration of the effect of parameters on stability in regions of parameter space that were previously inaccessible (Section S6; Figure S13). Given the connections between equilibrium and nonequilibrium metrics that we have established, the same metric can be used to measure the potential for perturbation amplification as a system's attractor changes (e.g., equilibrium point to limit cycle; Figure S13). The metrics derived here do rely on important assumptions such as the pulse perturbation being small and occurring only once. These metrics do not apply, for example, to large perturbations that immediately cause species extinctions. Regarding repeated small perturbations, future work could extend our framework by leveraging other equilibrium results (Arnoldi et al. 2016).

Because the main ingredient for computing $\min[r_\tau]$, \bar{r}_τ and $\max[r_\tau]$ is a sequence of Jacobian matrices, it is possible to apply our framework to natural communities by inferring these matrices from empirical data (Box 1). Jacobian matrices can be inferred from time series with regression models

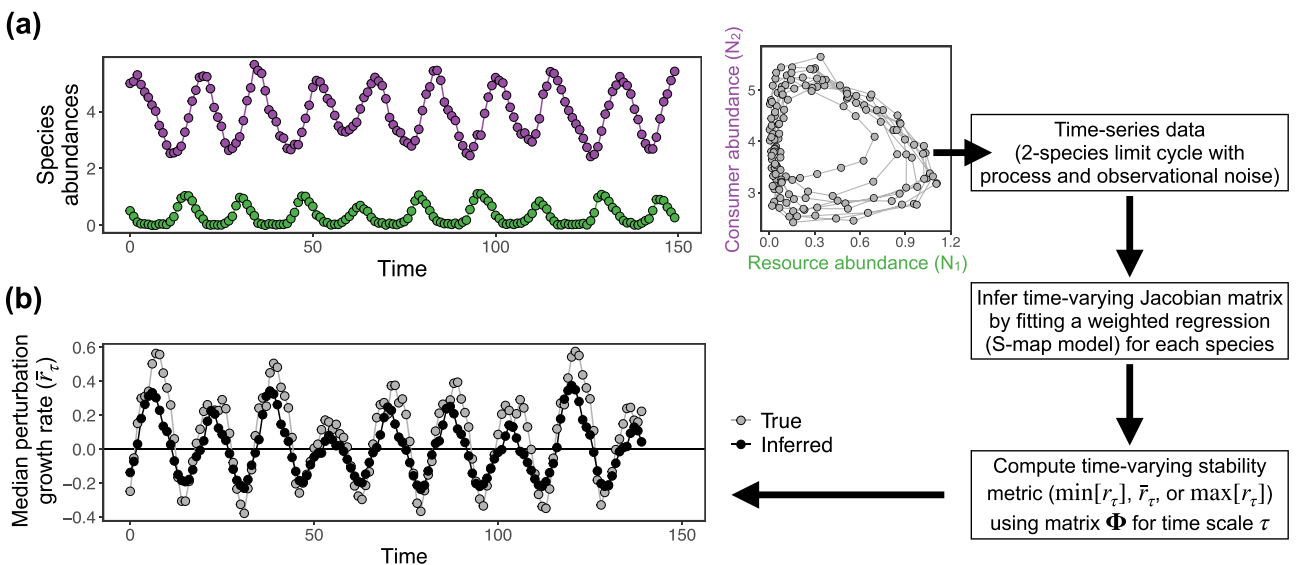


FIGURE 5 | Inference of stability metrics from abundance time series generated from a 2-species resource-consumer model under a limit cycle (Box 1). (a) Plot on the left shows the noisy time-series data for the resource ($N_1(t)$; green points) and consumer ($N_2(t)$; purple points) species with 150 observations ($t = 0, 1, \dots, 149$). Plot on the right shows the same data but plotted in state space. From this data, we first infer the Jacobian matrix $J_f(t)$ at all times t using a weighted regression (S-map model) that assumes continuous-time dynamics. Then, we use Equation (12) to compute the state-transition matrix Φ and Equation (21) to compute the median perturbation growth rate (\bar{r}_τ) at time scale $\tau = 10$. (b) Median perturbation growth rate for all times t computed analytically from Equation (24) (grey points) and inferred from the time series (black points). Note that, because $\tau = 10$, we cannot infer \bar{r}_τ for the last 9 observations in the time series. The correlation between true and inferred \bar{r}_τ is 0.92. The S-map hyperparameters selected with cross-validation are: $\theta = 2$, $\alpha = 0$ and $\lambda = 0$ (Section S7).

by making minimal assumptions about the underlying population dynamics (Cenci and Saavedra 2019; Deyle et al. 2016; Grziwotz et al. 2023; Hampton et al. 2013; Ives et al. 2003; Medeiros et al. 2023; Nguyen et al. 2025; Rogers et al. 2023; Stein et al. 2013; Ushio et al. 2018). To illustrate this procedure, we have shown that we can accurately infer \bar{r}_τ from noisy time series of 2- and 3-species systems (Figure 5 and Figures S14–S16). To summarise information, we recommend focusing on \bar{r}_τ or $\max[r_\tau]$ at the time scale τ that is most relevant for the research question. For instance, to understand how perturbations affect population booms or busts in short-lived organisms (e.g., insects, plankton), we could use a time scale of days or weeks. In addition to retrospective analyses, these metrics can be estimated for the last available time-series observation (Medeiros et al. 2023), providing information for conservation or management in the event of a perturbation.

Unobserved variables are a particularly important aspect of empirical ecological studies. One approach to deal with unobserved variables is to use time-delay embedding to infer Jacobian matrices from data on only one or a few species (Grziwotz et al. 2023; Rogers et al. 2022, 2023). With time-delay embedding, certain quantities (e.g., eigenvalues) are more informative than others (e.g., singular values; Section S4). Determining when one should infer stability metrics from single-species data with time-delay embedding (Grziwotz et al. 2023; Rogers et al. 2022, 2023), multispecies data ignoring unobserved variables (Figure 5; Cenci and Saavedra 2019; Deyle et al. 2016; Medeiros et al. 2023; Miki et al. 2025), or a combination of both (Ushio et al. 2018) is a valuable direction for future work. Overall, our framework should strengthen future studies by providing a bridge between inferred Jacobian matrices and stability analysis that was previously missing for nonequilibrium ecological communities.

Author Contributions

Lucas P. Medeiros and Stephan B. Munch developed the initial ideas with subsequent substantial inputs from Michael G. Neubert and Heidi M. Sosik. Lucas P. Medeiros performed mathematical and computational analyses with inputs from Stephan B. Munch and Michael G. Neubert. Lucas P. Medeiros wrote the paper and all authors revised and edited the text.

Acknowledgements

We thank Hal Caswell, Serguei Saavedra, Bethany Stevens and Chengyi Long for suggestions that improved this manuscript. We also thank members of the Munch and Sosik labs for helpful feedback during the development of this work. This work was supported by the National Oceanic and Atmospheric Administration's Quantitative Ecology and Socioeconomics Training Program (L.P.M.), a grant from the Simons Foundation (01188720, to H.M.S. and M.G.N.) and the US National Science Foundation (OCE-2322676, to H.M.S. and M.G.N.).

Funding

This work was supported by the National Oceanic and Atmospheric Administration's Quantitative Ecology and Socioeconomics Training Program (L.P.M.), a grant from the Simons Foundation (01188720, to H.M.S. and M.G.N.) and the US National Science Foundation (OCE-2322676, to H.M.S. and M.G.N.).

Conflicts of Interest

The authors declare no conflicts of interest.

Data Availability Statement

The codes to reproduce all analyses are archived on GitHub (<https://github.com/lucaspmedeiros/non-equilibrium-pulse-perturbations>)

and Zenodo (<https://doi.org/10.5281/zenodo.17992849>). No data were used in this study.

Peer Review

The peer review history for this article is available at <https://www.webofscience.com/api/gateway/wos/peer-review/10.1111/ele.70313>.

References

- Antsaklis, P. J., and A. N. Michel. 2006. *Linear Systems*. Springer.
- Argyris, J. H., G. Faust, M. Haase, and R. Friedrich. 2015. *An Exploration of Dynamical Systems and Chaos*. Springer.
- Arnoldi, J. F., A. Bideault, M. Loreau, and B. Haegeman. 2018. "How Ecosystems Recover From Pulse Perturbations: A Theory of Short- to Long-Term Responses." *Journal of Theoretical Biology* 436: 79–92.
- Arnoldi, J. F., M. Loreau, and B. Haegeman. 2016. "Resilience, Reactivity and Variability: A Mathematical Comparison of Ecological Stability Measures." *Journal of Theoretical Biology* 389: 47–59.
- Arnoldi, J. F., M. Loreau, and B. Haegeman. 2019. "The Inherent Multidimensionality of Temporal Variability: How Common and Rare Species Shape Stability Patterns." *Ecology Letters* 22: 1557–1567.
- Aurell, E., G. Boffetta, A. Crisanti, G. Paladin, and A. Vulpiani. 1997. "Predictability in the Large: An Extension of the Concept of Lyapunov Exponent." *Journal of Physics A: Mathematical and General* 30: 1–26.
- Barabás, G., G. Meszéna, and A. Ostling. 2012. "Community Robustness and Limiting Similarity in Periodic Environments." *Theoretical Ecology* 5: 265–282.
- Bender, E. A., T. J. Case, and M. E. Gilpin. 1984. "Perturbation Experiments in Community Ecology: Theory and Practice." *Ecology* 65: 1–13.
- Bieg, C., G. Gellner, and K. S. McCann. 2023. "Stability of Consumer-Resource Interactions in Periodic Environments." *Proceedings of the Royal Society B* 290: 20231636.
- Brando, P. M., J. K. Balch, D. C. Nepstad, et al. 2014. "Abrupt Increases in Amazonian Tree Mortality due to Drought-Fire Interactions." *Proceedings of the National Academy of Sciences* 111: 6347–6352.
- Caswell, H., and M. G. Neubert. 2005. "Reactivity and Transient Dynamics of Discrete-Time Ecological Systems." *Journal of Difference Equations and Applications* 11: 295–310.
- Cenci, S., and S. Saavedra. 2019. "Non-Parametric Estimation of the Structural Stability of Non-Equilibrium Community Dynamics." *Nature Ecology & Evolution* 3: 912–918.
- Datseris, G., and U. Parlitz. 2022. *Nonlinear Dynamics: A Concise Introduction Interlaced With Code*. Springer Nature.
- DeAngelis, D. L., and J. Waterhouse. 1987. "Equilibrium and Nonequilibrium Concepts in Ecological Models." *Ecological Monographs* 57: 1–21.
- Deyle, E. R., R. M. May, S. B. Munch, and G. Sugihara. 2016. "Tracking and Forecasting Ecosystem Interactions in Real Time." *Proceedings of the Royal Society B: Biological Sciences* 283: 20152258.
- Ellner, S., and P. Turchin. 1995. "Chaos in a Noisy World: New Methods and Evidence From Time-Series Analysis." *American Naturalist* 145: 343–375.
- Emanuel, K. 2005. "Increasing Destructiveness of Tropical Cyclones Over the Past 30 Years." *Nature* 436: 686–688.
- Funasaki, E., and M. Kot. 1993. "Invasion and Chaos in a Periodically Pulsed Mass-Action Chemostat." *Theoretical Population Biology* 44: 203–224.
- Geist, K., U. Parlitz, and W. Lauterborn. 1990. "Comparison of Different Methods for Computing Lyapunov Exponents." *Progress of Theoretical Physics* 83: 875–893.
- Gilpin, W. 2023. "Model Scale Versus Domain Knowledge in Statistical Forecasting of Chaotic Systems." *Physical Review Research* 5: 043252.
- Grziwotz, F., C. W. Chang, V. Dakos, et al. 2023. "Anticipating the Occurrence and Type of Critical Transitions." *Science Advances* 9: eabq4558.
- Hampton, S. E., E. E. Holmes, L. P. Scheef, et al. 2013. "Quantifying Effects of Abiotic and Biotic Drivers on Community Dynamics With Multivariate Autoregressive (Mar) Models." *Ecology* 94: 2663–2669.
- Harrison, G. W. 1979. "Stability Under Environmental Stress: Resistance, Resilience, Persistence, and Variability." *American Naturalist* 113: 659–669.
- Hastings, A., K. C. Abbott, K. Cuddington, et al. 2018. "Transient Phenomena in Ecology." *Science* 361: eaat6412.
- Hastings, A., and T. Powell. 1991. "Chaos in a Three-Species Food Chain." *Ecology* 72: 896–903.
- Holling, C. S. 1973. "Resilience and Stability of Ecological Systems." *Annual Review of Ecology and Systematics* 4: 1–23.
- Hughes, T. P., J. T. Kerry, A. H. Baird, et al. 2018. "Global Warming Transforms Coral Reef Assemblages." *Nature* 556: 492–496.
- Ives, A. R., B. Dennis, K. L. Cottingham, and S. R. Carpenter. 2003. "Estimating Community Stability and Ecological Interactions From Time-Series Data." *Ecological Monographs* 73: 301–330.
- Kéfi, S., V. Domínguez-García, I. Donohue, C. Fontaine, E. Thébaud, and V. Dakos. 2019. "Advancing Our Understanding of Ecological Stability." *Ecology Letters* 22: 1349–1356.
- Klausmeier, C. A. 2008. "Floquet Theory: A Useful Tool for Understanding Nonequilibrium Dynamics." *Theoretical Ecology* 1: 153–161.
- Lewis, S. C., and D. J. Karoly. 2013. "Anthropogenic Contributions to Australia's Record Summer Temperatures of 2013." *Geophysical Research Letters* 40: 3705–3709.
- May, R. M. 1973. *Stability and Complexity in Model Ecosystems*. Princeton University Press.
- McCann, K. S. 2011. *Food Webs (MPB-50)*. Princeton University Press.
- Medeiros, L. P., S. Allesina, V. Dakos, G. Sugihara, and S. Saavedra. 2023. "Ranking Species Based on Sensitivity to Perturbations Under Non-Equilibrium Community Dynamics." *Ecology Letters* 26: 170–183.
- Medeiros, L. P., and S. Saavedra. 2023. "Understanding the State-Dependent Impact of Species Correlated Responses on Community Sensitivity to Perturbations." *Ecology* 104: e4115.
- Miki, T., C. W. Chang, P. J. Ke, et al. 2025. "How to Quantify Interaction Strengths? A Critical Rethinking of the Interaction Jacobian and Evaluation Methods for Non-Parametric Inference in Time Series Analysis." *Physica D: Nonlinear Phenomena* 476: 134613.
- Munch, S. B., A. Brias, G. Sugihara, and T. L. Rogers. 2020. "Frequently Asked Questions About Nonlinear Dynamics and Empirical Dynamic Modelling." *ICES Journal of Marine Science* 77: 1463–1479.
- Nazerian, A., F. Sorrentino, and Z. Aminzare. 2024. "Bridging the Gap Between Reactivity, Contraction and Finite-Time Lyapunov Exponents." *arXiv Preprint*: 2410.23435.
- Neubert, M. G., and H. Caswell. 1997. "Alternatives to Resilience for Measuring the Responses of Ecological Systems to Perturbations." *Ecology* 78: 653–665.
- Nguyen, P. L., F. Pomati, and R. P. Rohr. 2025. "Inferring Coexistence Likelihood in Changing Environments From Ecological Time Series." *Proceedings of the National Academy of Sciences* 122: e2417905122.

- Perko, L. 2013. *Differential Equations and Dynamical Systems*. Vol. 7. Springer Science & Business Media.
- Rogers, T. L., B. J. Johnson, and S. B. Munch. 2022. "Chaos Is Not Rare in Natural Ecosystems." *Nature Ecology & Evolution* 6: 1105–1111.
- Rogers, T. L., S. B. Munch, S. I. S. Matsuzaki, and C. C. Symons. 2023. "Intermittent Instability Is Widespread in Plankton Communities." *Ecology Letters* 26: 470–481.
- Rosenzweig, M. L., and R. H. MacArthur. 1963. "Graphical Representation and Stability Conditions of Predator-Prey Interactions." *American Naturalist* 97: 209–223.
- Song, C., and S. Saavedra. 2021. "Bridging Parametric and Nonparametric Measures of Species Interactions Unveils New Insights of Non-Equilibrium Dynamics." *Oikos* 130: 1027–1034.
- Stein, R. R., V. Bucci, N. C. Toussaint, et al. 2013. "Ecological Modeling From Time-Series Inference: Insight Into Dynamics and Stability of Intestinal Microbiota." *PLoS Computational Biology* 9: e1003388.
- Strogatz, S. H. 2000. *Nonlinear Dynamics and Chaos: With Applications to Physics, Biology, Chemistry, and Engineering*. CRC press.
- Sugihara, G. 1994. "Nonlinear Forecasting for the Classification of Natural Time Series." *Philosophical Transactions of the Royal Society of London. Series A, Physical and Engineering Sciences* 348: 477–495.
- Sugihara, G., and R. M. May. 1990. "Nonlinear Forecasting as a Way of Distinguishing Chaos From Measurement Error in Time Series." *Nature* 344: 734–741.
- Suzuki, K., K. Yoshida, Y. Nakanishi, and S. Fukuda. 2017. "An Equation-Free Method Reveals the Ecological Interaction Networks Within Complex Microbial Ecosystems." *Methods in Ecology and Evolution* 8: 1774–1785.
- Trenberth, K. E., J. T. Fasullo, and T. G. Shepherd. 2015. "Attribution of Climate Extreme Events." *Nature Climate Change* 5: 725–730.
- Turchin, P. 2013. *Complex Population Dynamics: A Theoretical/Empirical Synthesis* (MPB-35). Princeton University Press.
- Ushio, M., C. H. Hsieh, R. Masuda, et al. 2018. "Fluctuating Interaction Network and Time-Varying Stability of a Natural Fish Community." *Nature* 554: 360–363.

Supporting Information

Additional supporting information can be found online in the Supporting Information section. **Data S1:** ele70313-sup-0001-Supinfo.pdf.

Supporting Information

A nonequilibrium framework for community responses to pulse perturbations

Lucas P. Medeiros^{1,*}, Michael G. Neubert¹, Heidi M. Sosik¹ and Stephan B. Munch^{2,3}

¹Department of Biology, Woods Hole Oceanographic Institution, Woods Hole, MA 02543, USA

²Southwest Fisheries Science Center, National Oceanic and Atmospheric Administration, Santa Cruz, CA 95060, USA

³Department of Applied Mathematics, University of California, Santa Cruz, CA 95064, USA

* To whom correspondence should be addressed. E-mail: lucas.medeiros@whoi.edu

Contents

S1 Derivation of linear dynamics of perturbations	2
S2 Derivation of stability metrics	3
S2.1 Median perturbation growth rate	3
S2.2 Maximum and minimum perturbation growth rate	5
S3 Connections to other stability metrics	6
S3.1 Largest eigenvalue	6
S3.2 Determinant	7
S4 Stability metrics under time-delay embedding	9
S4.1 Eigenvalues and singular values	10
S4.2 Constraint on singular values	11
S5 Accuracy of stability metrics under discrete-time models	13
S6 Exploring effects of parameter changes on stability metrics	14
S7 Inference of stability metrics from time-series data	15
S7.1 S-map model	15
S7.2 S-map model for continuous-time population dynamics	17
S7.3 Estimation of S-map coefficients	18
S7.4 Illustration of stability metrics inference	19
S8 Figures and Tables	21

1 S1 Derivation of linear dynamics of perturbations

2 In this section, we show how to derive the linear dynamics of a small pulse perturbation. This derivation can also be found in dynamical systems textbooks (e.g., Argyris
 3 *et al.* (2015)). Following the main text, we use a generic model for the population dynam-
 4 ics of a community with S species: $\frac{d\mathbf{N}(t)}{dt} = \mathbf{f}(\mathbf{N}(t), t)$, where $\mathbf{N}(t) = [N_1(t), \dots, N_S(t)]^\top$ is
 5 the vector containing species abundances at time t and $\mathbf{f} = [f_1, \dots, f_S]^\top$ is a vector-valued
 6 function. Note that each f_i is generally a nonlinear function with multiple parameters,
 7 which we omit to simplify the notation. However, we explicitly denote the dependence
 8 of \mathbf{f} on t (i.e., a nonautonomous system), given that we explore systems with parameters
 9 that change through time in the main text (Figs. 3 and 4). The autonomous system given
 10 by $\frac{d\mathbf{N}(t)}{dt} = \mathbf{f}(\mathbf{N}(t))$ is a special case of the nonautonomous system and the derivations
 11 below are valid for both.

13 At a given state $\tilde{\mathbf{N}}(t)$, a pulse perturbation $\mathbf{x}(t) = [x_1(t), \dots, x_S(t)]^\top$ moves species
 14 abundances from $\tilde{\mathbf{N}}(t)$ to $\mathbf{N}(t)$ (i.e., $\mathbf{x}(t) = \mathbf{N}(t) - \tilde{\mathbf{N}}(t)$). We can obtain the linearized
 15 dynamics of $\mathbf{x}(t)$ by computing the Taylor expansion of $\frac{d\mathbf{N}(t)}{dt}$ around $\tilde{\mathbf{N}}(t)$:

$$\frac{d\mathbf{N}(t)}{dt} = \mathbf{f}(\tilde{\mathbf{N}}(t)) + \left. \frac{\partial \mathbf{f}}{\partial \mathbf{N}} \right|_{\mathbf{N}=\tilde{\mathbf{N}}}(t)(\mathbf{N}(t) - \tilde{\mathbf{N}}(t)) + O(\mathbf{x}(t)^\top \mathbf{x}(t)), \quad (\text{S1})$$

16 where we denote $\left. \frac{\partial \mathbf{f}}{\partial \mathbf{N}} \right|_{\mathbf{N}=\tilde{\mathbf{N}}}(t) = \mathbf{J}_f(t)$ as the $S \times S$ Jacobian matrix evaluated at $\tilde{\mathbf{N}}(t)$. If
 17 $\mathbf{x}(t)$ remains sufficiently small over time, we can approximate its dynamics by taking just
 18 the linear term (i.e., ignoring higher-order terms):

$$\begin{aligned} \frac{d\mathbf{N}(t)}{dt} &= \mathbf{f}(\tilde{\mathbf{N}}(t)) + \left. \frac{\partial \mathbf{f}}{\partial \mathbf{N}} \right|_{\mathbf{N}=\tilde{\mathbf{N}}}(t)(\mathbf{N}(t) - \tilde{\mathbf{N}}(t)) \\ \frac{d\tilde{\mathbf{N}}(t)}{dt} + \frac{d\mathbf{x}(t)}{dt} &= \frac{d\tilde{\mathbf{N}}(t)}{dt} + \mathbf{J}_f(t)\mathbf{x}(t) \\ \frac{d\mathbf{x}(t)}{dt} &= \mathbf{J}_f(t)\mathbf{x}(t). \end{aligned} \quad (\text{S2})$$

19 Therefore, as stated in the main text, the dynamics of a pulse perturbation $\mathbf{x}(t)$ can
 20 be approximated by the linear equation above. Note that we have not assumed that
 21 the unperturbed state ($\tilde{\mathbf{N}}(t)$) is an equilibrium point (i.e., that it satisfies $\frac{d\mathbf{N}(t)}{dt} = \mathbf{0}$).
 22 Thus, the equation above is valid for any nonequilibrium trajectory. Finally, the above
 23 derivation also shows that we can linearize a nonautonomous system in the same way
 24 that we linearize an autonomous system. What is important is that the dependence of \mathbf{f}
 25 on t is inherited by its Jacobian matrix $\mathbf{J}_f(t)$. That is, $\mathbf{J}_f(t)$ depends not only on $\tilde{\mathbf{N}}(t)$
 26 but also explicitly on t .

27 S2 Derivation of stability metrics

28 Here, we derive the metrics \bar{r}_τ , $\max[r_\tau]$, and $\min[r_\tau]$ introduced in the main text
 29 (equations (21), (22), and (23)). These metrics measure the median, maximum, and
 30 minimum perturbation growth rate over a distribution of pulse perturbations around an
 31 unperturbed state $\tilde{\mathbf{N}}(t)$. The perturbation growth rate of a given pulse perturbation $\mathbf{x}(t)$
 32 from t_0 to t_n is given by

$$r_\tau = \frac{1}{\tau} \log \left[\frac{\|\mathbf{x}(t_n)\|}{\|\mathbf{x}(t_0)\|} \right] = \frac{1}{2\tau} \log \left[\frac{\|\mathbf{x}(t_n)\|^2}{\|\mathbf{x}(t_0)\|^2} \right], \quad (\text{S3})$$

33 where $\|\mathbf{x}(t)\| = \sqrt{\sum_{i=1}^S x_i(t)^2}$ is the Euclidean norm (or size) of the perturbation at time
 34 t .

35 S2.1 Median perturbation growth rate

36 We start by deriving the median perturbation growth rate (\bar{r}_τ). To do so, we con-
 37 sider that initial perturbations $\mathbf{x}(t_0)$ follow some arbitrary distribution with mean vector
 38 $\mathbb{E}[\mathbf{x}(t_0)] = \boldsymbol{\mu}_0$ and covariance matrix $\text{Cov}[\mathbf{x}(t_0)] = \boldsymbol{\Sigma}_0$. We can then analyze the growth
 39 rate of expected perturbation sizes, which is given by

$$\bar{r}_\tau = \frac{1}{2\tau} \log \left[\frac{\mathbb{E}[\|\mathbf{x}(t_n)\|^2]}{\mathbb{E}[\|\mathbf{x}(t_0)\|^2]} \right]. \quad (\text{S4})$$

40 Following Arnoldi *et al.* (2018) and Medeiros *et al.* (2023), $\mathbb{E}[\|\mathbf{x}(t_n)\|^2]$ is given by

$$\begin{aligned} \mathbb{E}[\|\mathbf{x}(t_n)\|^2] &= \mathbb{E}[\mathbf{x}(t_n)^\top \mathbf{x}(t_n)] \\ &= \mathbb{E}[(\Phi \mathbf{x}(t_0))^\top (\Phi \mathbf{x}(t_0))] \\ &= \mathbb{E}[\text{tr}[(\Phi \mathbf{x}(t_0))(\Phi \mathbf{x}(t_0))^\top]] \\ &= \text{tr}[\Phi \mathbb{E}[\mathbf{x}(t_0) \mathbf{x}(t_0)^\top] \Phi^\top] \\ &= \text{tr}[\Phi (\boldsymbol{\Sigma}_0 + \boldsymbol{\mu}_0 \boldsymbol{\mu}_0^\top) \Phi^\top], \end{aligned} \quad (\text{S5})$$

41 where Φ is the state-transition matrix (often called fundamental matrix) that connects
 42 $\mathbf{x}(t_0)$ to $\mathbf{x}(t_n)$ as explained in the main text and $\text{tr}(\mathbf{A})$ stands for the trace (i.e., sum of
 43 diagonal elements) of an arbitrary matrix \mathbf{A} . Similarly, $\mathbb{E}[\|\mathbf{x}(t_0)\|^2]$ is given by

$$\begin{aligned} \mathbb{E}[\|\mathbf{x}(t_0)\|^2] &= \mathbb{E}[\mathbf{x}(t_0)^\top \mathbf{x}(t_0)] \\ &= \text{tr}[\mathbb{E}[\mathbf{x}(t_0) \mathbf{x}(t_0)^\top]] \\ &= \text{tr}[\boldsymbol{\Sigma}_0 + \boldsymbol{\mu}_0 \boldsymbol{\mu}_0^\top]. \end{aligned} \quad (\text{S6})$$

44 Combining these two equations, we obtain a general expression for \bar{r}_τ :

$$\bar{r}_\tau = \frac{1}{2\tau} \log \left[\frac{\text{tr}[\Phi(\Sigma_0 + \mu_0\mu_0^\top)\Phi^\top]}{\text{tr}[\Sigma_0 + \mu_0\mu_0^\top]} \right]. \quad (\text{S7})$$

45 We can now obtain simplified versions of \bar{r}_τ by making additional assumptions. First,
 46 if we consider that perturbations are centered in $\tilde{\mathbf{N}}(t)$ (i.e., not biased in any direction),
 47 then we have $\mu_0 = \mathbf{0}$, which gives

$$\bar{r}_\tau = \frac{1}{2\tau} \log \left[\frac{\text{tr}[\Phi\Sigma_0\Phi^\top]}{\text{tr}[\Sigma_0]} \right]. \quad (\text{S8})$$

48 Second, if we consider that perturbations affect each species independently with identical
 49 variance, then we have $\Sigma_0 = \sigma^2\mathbf{I}$, which gives

$$\begin{aligned} \bar{r}_\tau &= \frac{1}{2\tau} \log \left[\frac{\sigma^2 \text{tr}[\Phi\Phi^\top]}{S\sigma^2} \right] \\ &= \frac{1}{2\tau} \log \left[\frac{\text{tr}[\Phi\Phi^\top]}{S} \right], \end{aligned} \quad (\text{S9})$$

50 where \mathbf{I} is the $S \times S$ identity matrix.

51 As suggested by [Arnoldi et al. \(2018\)](#) for equilibrium dynamics, \bar{r}_τ computed using
 52 equation (S9) is an excellent approximation to the median of the distribution of pertur-
 53 bation growth rates. That is, even though \bar{r}_τ does not correspond to the average of r_τ
 54 (i.e., $\mathbb{E}[r_\tau]$), it does accurately capture the median of r_τ , which we will denote as $\mathbb{M}[r_\tau]$.
 55 We can demonstrate this connection between \bar{r}_τ and $\mathbb{M}[r_\tau]$ using the following result:
 56 $\mathbb{M}[g(Y)] = g(\mathbb{M}[Y])$, where Y is a random variable and g is a monotonic function. With-
 57 out loss of generality, we can ignore τ and $\|\mathbf{x}(t_0)\|^2$ in equation (S4) and just focus on
 58 $\|\mathbf{x}(t_n)\|^2$. Given that log is a monotonic function, we have that

$$\mathbb{M}[\log[\|\mathbf{x}(t_n)\|^2]] = \log[\mathbb{M}[\|\mathbf{x}(t_n)\|^2]]. \quad (\text{S10})$$

59 If the distribution of $\|\mathbf{x}(t_n)\|^2$ is symmetric, then its mean is equal to its median and we
 60 have that:

$$\mathbb{M}[r_\tau] = \mathbb{M}[\log[\|\mathbf{x}(t_n)\|^2]] = \log[\mathbb{M}[\|\mathbf{x}(t_n)\|^2]] = \log[\mathbb{E}[\|\mathbf{x}(t_n)\|^2]] = \bar{r}_\tau. \quad (\text{S11})$$

61 In this case, we have a direct connection between our analytical metric (\bar{r}_τ) and the
 62 median perturbation growth rate ($\mathbb{M}[r_\tau]$). For less symmetric distributions of $\|\mathbf{x}(t_n)\|^2$,
 63 we propose that $\log[\mathbb{M}[\|\mathbf{x}(t_n)\|^2]]$ is a reasonable approximation to $\log[\mathbb{E}[\|\mathbf{x}(t_n)\|^2]]$ and,
 64 therefore, \bar{r}_τ will approximate $\mathbb{M}[r_\tau]$.

65 In addition to this connection between \bar{r}_τ and $\mathbb{M}[r_\tau]$, we can show that \bar{r}_τ is always an

66 upper bound to the average perturbation growth rate ($\mathbb{E}[r_\tau]$). Jensen's inequality states
 67 that $\mathbb{E}[f(Y)] \leq f(\mathbb{E}[Y])$, where Y is a random variable and f is a concave function. Given
 68 that \log is a concave function, we have that

$$\mathbb{E}[r_\tau] = \mathbb{E}[\log[||\mathbf{x}(t_n)||^2]] \leq \log[\mathbb{E}[||\mathbf{x}(t_n)||^2]] = \bar{r}_\tau. \quad (\text{S12})$$

69 Thus, from the above inequality, we know that \bar{r}_τ is always an upper bound to $\mathbb{E}[r_\tau]$.

70 S2.2 Maximum and minimum perturbation growth rate

71 We now derive the metrics for maximum and minimum perturbation growth rate.
 72 This derivation is based on previous results on reactivity in dynamical systems (Caswell
 73 & Neubert, 2005, Nazerian *et al.*, 2024, Neubert & Caswell, 1997). The maximum per-
 74 turbation growth rate will be given by

$$\begin{aligned} \max[r_\tau] &= \max_{\mathbf{x}(t_0) \neq \mathbf{0}} \left[\frac{1}{\tau} \log \left[\frac{||\mathbf{x}(t_n)||}{||\mathbf{x}(t_0)||} \right] \right] \\ &= \frac{1}{\tau} \log \left[\max_{\mathbf{x}(t_0) \neq \mathbf{0}} \left[\frac{||\mathbf{x}(t_n)||}{||\mathbf{x}(t_0)||} \right] \right] \\ &= \frac{1}{\tau} \log \left[\max_{\mathbf{x}(t_0) \neq \mathbf{0}} \left[\frac{||\Phi \mathbf{x}(t_0)||}{||\mathbf{x}(t_0)||} \right] \right] \\ &= \frac{1}{\tau} \log [|||\Phi|||] \\ &= \frac{1}{\tau} \log [\sigma_1(\Phi)], \end{aligned} \quad (\text{S13})$$

75 where $|||\mathbf{A}|||$ is the spectral norm of an arbitrary matrix \mathbf{A} , which corresponds to its
 76 largest singular value ($\sigma_1(\mathbf{A})$). An $S \times S$ matrix \mathbf{A} has S singular values ($\sigma_S \leq \dots \leq \sigma_1$),
 77 which are all real numbers. Note that, for a matrix \mathbf{A} , the definition of the spectral norm
 78 is the maximum value of $\frac{||\mathbf{A}\mathbf{y}||}{||\mathbf{y}||}$ under the Euclidean (or l_2) norm and a nonzero vector \mathbf{y}
 79 (Golub & Van Loan, 2013). Therefore, $\max[r_\tau]$ is linked to the spectral norm, whereas
 80 \bar{r}_τ is linked to the Frobenius norm of the state-transition matrix Φ (Golub & Van Loan,
 81 2013).

82 The derivation of the minimum perturbation growth rate is analogous to the derivation
 83 above. Instead of the maximum, we want to compute the minimum of $\frac{||\mathbf{A}\mathbf{y}||}{||\mathbf{y}||}$ under the
 84 Euclidean (or l_2) norm and a nonzero vector \mathbf{y} . It can be proved that this minimum is
 85 given by the smallest singular value of \mathbf{A} ($\sigma_S(\mathbf{A})$; Golub & Van Loan (2013)). Therefore,

86 we have that

$$\begin{aligned}\min[r_\tau] &= \min_{\mathbf{x}(t_0) \neq \mathbf{0}} \left[\frac{1}{\tau} \log \left[\frac{\|\mathbf{x}(t_n)\|}{\|\mathbf{x}(t_0)\|} \right] \right] \\ &= \frac{1}{\tau} \log \left[\min_{\mathbf{x}(t_0) \neq \mathbf{0}} \left[\frac{\|\Phi \mathbf{x}(t_0)\|}{\|\mathbf{x}(t_0)\|} \right] \right] \\ &= \frac{1}{\tau} \log [\sigma_S(\Phi)].\end{aligned}\tag{S14}$$

87 S3 Connections to other stability metrics

88 Previous studies in ecology have explored other metrics to measure stability under
89 nonequilibrium population dynamics. Two previously used metrics are the largest eigen-
90 value and the determinant of the state-transition matrix Φ . The largest eigenvalue of Φ
91 has been used to measure stability under both short (Rogers *et al.*, 2023, Ushio *et al.*,
92 2018) and long (Rogers *et al.*, 2022) time scales. The determinant of Φ is connected to
93 the trace of the continuous-time Jacobian matrix \mathbf{J}_f and has been used to measure the
94 expansion rate of a volume of perturbed abundances (Cenci & Saavedra, 2019, Chang
95 *et al.*, 2021, Medeiros & Saavedra, 2023, Zhao *et al.*, 2023). However, these past studies
96 have not explicitly used the concept of a state-transition matrix. In addition, the largest
97 eigenvalue and determinant have not been explicitly connected to the growth rate of pulse
98 perturbations under nonequilibrium dynamics. In this section, we show that the largest
99 eigenvalue and determinant of Φ are approximations to $\max[r_\tau]$ and \bar{r}_τ , respectively.

100 S3.1 Largest eigenvalue

101 The connection between the largest eigenvalue of Φ and $\max[r_\tau]$ comes from a simple
102 relationship between the eigenvalues and singular values of a matrix. That is, the smallest
103 ($\sigma_S(\mathbf{A})$) and largest ($\sigma_1(\mathbf{A})$) singular values of an $S \times S$ matrix \mathbf{A} bound the smallest
104 and largest eigenvalues in absolute value (Golub & Van Loan, 2013):

$$\sigma_S(\mathbf{A}) \leq \min_i |\lambda_i(\mathbf{A})| \leq \max_i |\lambda_i(\mathbf{A})| \leq \sigma_1(\mathbf{A}),\tag{S15}$$

105 where the absolute value of a complex number z (i.e., any of the eigenvalues) is $|z| =$
106 $\sqrt{\text{Re}(z)^2 + \text{Im}(z)^2}$, where $\text{Re}(z)$ is the real part and $\text{Im}(z)$ is the imaginary part of z .
107 This result allows us to use the largest eigenvalue of Φ (in absolute value) as a lower
108 bound to its largest singular value. For instance, if one is interested in knowing whether
109 $\sigma_1(\Phi) > 1$ (i.e., at least one perturbation will grow), finding that $\max_i |\lambda_i(\Phi)| > 1$ is a
110 sufficient condition. Nevertheless, finding that $\max_i |\lambda_i(\Phi)| < 1$ does not guarantee that
111 $\sigma_1(\Phi) < 1$ (i.e., all perturbations will shrink).

112 For long time scales (i.e., τ is large), Φ will be the product of a large number of
113 Jacobian matrices. This product typically leads to a big gap between the second-largest

and the largest singular value, that is: $\sigma_2(\Phi) \ll \sigma_1(\Phi)$. In this case, $\max_i |\lambda_i(\Phi)| \approx \sigma_1(\Phi)$, especially if Φ is not far from being a normal matrix (Golub & Van Loan, 2013). In Fig. S7, we use our simulation scenarios to illustrate that $\max_i |\lambda_i(\Phi)|$ is always a lower bound to $\sigma_1(\Phi)$ and that these two quantities are close to each other when τ is large. The lower bound given by $\max_i |\lambda_i(\Phi)|$ has been used in previous studies as a way to detect chaos—that is, a positive Lyapunov exponent ($\max[r_\tau] > 0$ for large τ)—in natural populations (Rogers *et al.*, 2022, 2023).

S3.2 Determinant

The connection between the determinant of Φ and \bar{r}_τ can be derived for small τ . Our derivation is based on a similar proof by Arnoldi *et al.* (2018) that assumed equilibrium dynamics. We start by defining the instantaneous perturbation growth rate from an arbitrary time t to $t + \tau$ as

$$\begin{aligned} \lim_{\tau \rightarrow 0} r_\tau &= \lim_{\tau \rightarrow 0} \frac{\log [||\mathbf{x}(t + \tau)||^2] - \log [||\mathbf{x}(t)||^2]}{2\tau} \\ &= \frac{1}{2} \frac{d \log [||\mathbf{x}(t)||^2]}{dt} \\ &= \frac{1}{2||\mathbf{x}(t)||^2} \frac{d||\mathbf{x}(t)||^2}{dt}. \end{aligned} \quad (\text{S16})$$

The term on the right of the equation above can be computed considering the linear dynamics from equation (S2):

$$\begin{aligned} \frac{d||\mathbf{x}(t)||^2}{dt} &= \frac{d\mathbf{x}(t)^\top \mathbf{x}(t)}{dt} \\ &= \mathbf{x}(t)^\top [\mathbf{J}_f \mathbf{x}(t)] + [\mathbf{J}_f \mathbf{x}(t)]^\top \mathbf{x}(t) \\ &= 2\mathbf{x}(t)^\top H(\mathbf{J}_f) \mathbf{x}(t), \end{aligned} \quad (\text{S17})$$

where $H(\mathbf{A}) = \left[\frac{\mathbf{A} + \mathbf{A}^\top}{2} \right]$ is called the symmetric (or Hermitian) part of a matrix \mathbf{A} . This result was first derived by Neubert & Caswell (1997). We now take the expectation of equation (S17):

$$\begin{aligned} \mathbb{E} \left[\frac{d||\mathbf{x}(t)||^2}{dt} \right] &= 2\mathbb{E} \left[\mathbf{x}(t)^\top H(\mathbf{J}_f) \mathbf{x}(t) \right] \\ &= 2\mathbb{E} \left[\text{tr} [H(\mathbf{J}_f) \mathbf{x}(t) \mathbf{x}(t)^\top] \right] \\ &= 2\text{tr} [\mathbf{J}_f \mathbb{E}[\mathbf{x}(t) \mathbf{x}(t)^\top]]. \end{aligned} \quad (\text{S18})$$

¹³¹ Combining equations (S4) and (S16), we can write the instantaneous growth rate of
¹³² expected perturbation sizes as

$$\begin{aligned}\lim_{\tau \rightarrow 0} \bar{r}_\tau &= \frac{1}{2\mathbb{E}[||\mathbf{x}(t)||^2]} \frac{d\mathbb{E}[||\mathbf{x}(t)||^2]}{dt} \\ &= \frac{1}{2\mathbb{E}[||\mathbf{x}(t)||^2]} \mathbb{E}\left[\frac{d||\mathbf{x}(t)||^2}{dt}\right].\end{aligned}\quad (\text{S19})$$

¹³³ Now, we evaluate the above equation at initial time t_0 :

$$\begin{aligned}\frac{1}{2\mathbb{E}[||\mathbf{x}(t_0)||^2]} \mathbb{E}\left[\frac{d||\mathbf{x}(t_0)||^2}{dt}\right] &= \frac{1}{2\text{tr}[\Sigma_0 + \boldsymbol{\mu}_0 \boldsymbol{\mu}_0^\top]} 2\text{tr}[\mathbf{J}_f(t_0) \mathbb{E}[\mathbf{x}(t_0) \mathbf{x}(t_0)^\top]] \\ &= \frac{1}{\text{tr}[\Sigma_0 + \boldsymbol{\mu}_0 \boldsymbol{\mu}_0^\top]} \text{tr}[\mathbf{J}_f(t_0)(\Sigma_0 + \boldsymbol{\mu}_0 \boldsymbol{\mu}_0^\top)].\end{aligned}\quad (\text{S20})$$

¹³⁴ The result in equation (S20) applies to any mean vector $\boldsymbol{\mu}_0$ and covariance matrix Σ_0
¹³⁵ of the distribution of initial perturbations $\mathbf{x}(t_0)$. However, to simplify this equation, we
¹³⁶ assume that $\boldsymbol{\mu}_0 = \mathbf{0}$ and $\Sigma_0 = \sigma^2 \mathbf{I}$. In this case, we obtain

$$\begin{aligned}\frac{1}{2\mathbb{E}[||\mathbf{x}(t_0)||^2]} \mathbb{E}\left[\frac{d||\mathbf{x}(t_0)||^2}{dt}\right] &= \frac{1}{\text{tr}[\sigma^2 \mathbf{I}]} \text{tr}[\mathbf{J}_f(t_0) \sigma^2 \mathbf{I}] \\ &= \frac{1}{S} \text{tr}[\mathbf{J}_f(t_0)].\end{aligned}\quad (\text{S21})$$

¹³⁷ Equation (S21) shows that $\lim_{\tau \rightarrow 0} \bar{r}_\tau$ computed at initial time t_0 is simply the trace of
¹³⁸ the Jacobian matrix \mathbf{J}_f divided by the number of species S (Arnoldi *et al.*, 2018).

¹³⁹ To connect the determinant of Φ to \bar{r}_τ , we use a result that links the determinant
¹⁴⁰ of Φ to the trace of \mathbf{J}_f (i.e., Liouville's Theorem; Argyris *et al.* (2015), Perko (2013)),
¹⁴¹ which measures the expansion rate of a volume of perturbed abundances. Specifically, the
¹⁴² volume of perturbed abundances at times t_0 and t_n is proportional to the determinants
¹⁴³ of Σ_0 and $\Phi \Sigma_0 \Phi^\top$, respectively (Medeiros & Saavedra, 2023). Note that the derivation
¹⁴⁴ below applies when $\boldsymbol{\mu}_0 \neq \mathbf{0}$ as well. The ratio of volumes in log is given by

$$\begin{aligned}\log \left[\frac{\det[\Phi \Sigma_0 \Phi^\top]}{\det[\Sigma_0]} \right] &= \log \left[\frac{\det[\Phi] \det[\Sigma_0] \det[\Phi^\top]}{\det[\Sigma_0]} \right] \\ &= 2 \log [\det[\Phi]] \\ &= 2 \log \left[\det \left[\exp \left[\int_{t_0}^{t_n} \mathbf{J}_f(s) ds \right] \right] \right] \\ &= 2 \log \left[\exp \left[\int_{t_0}^{t_n} \text{tr}[\mathbf{J}_f(s)] ds \right] \right] \\ &= 2 \int_{t_0}^{t_n} \text{tr}[\mathbf{J}_f(s)] ds.\end{aligned}\quad (\text{S22})$$

¹⁴⁵ Equation (S22) shows that the ratio of volumes can be obtained by integrating the trace
¹⁴⁶ of \mathbf{J}_f from t_0 to t_n . We now consider a special case of equation (S22) when $\tau = t_n - t_0$
¹⁴⁷ is small. A derivation under this special case can also be found in [Medeiros & Saavedra](#)
¹⁴⁸ ([2023](#)). In this case, we can use the following approximation for the state-transition
¹⁴⁹ matrix: $\Phi \approx \exp[\tau \mathbf{J}_f(t_0)] = \mathbf{J}_F(t_0)$, where $\mathbf{J}_f(t_0)$ and $\mathbf{J}_F(t_0)$ are the Jacobian matrices
¹⁵⁰ at t_0 in continuous and discrete time, respectively. The ratio of volumes in log is then
¹⁵¹ given by

$$\begin{aligned} \log \left[\frac{\det[\Phi \Sigma_0 \Phi^\top]}{\det[\Sigma_0]} \right] &= 2 \log [\det[\Phi]] \\ &= 2\tau \text{tr}[\mathbf{J}_f(t_0)]. \end{aligned} \quad (\text{S23})$$

¹⁵² Combining equations (S21) and (S23), we have that

$$\lim_{\tau \rightarrow 0} \bar{r}_\tau = \frac{1}{S} \text{tr}[\mathbf{J}_f(t_0)] = \frac{1}{S\tau} \log [\det(\Phi)]. \quad (\text{S24})$$

¹⁵³ Fig. S8 confirms the accuracy of this approximation under our simulation scenarios. Un-
¹⁵⁴ der continuous time, the trace of \mathbf{J}_f evaluated at a given state \mathbf{N} is the divergence of
¹⁵⁵ the vector field \mathbf{f} around \mathbf{N} ([Cenci & Saavedra, 2019](#), [Strogatz, 2000](#)). Hence, equation
¹⁵⁶ (S22) states that the change in the volume of perturbed abundances is equivalent to the
¹⁵⁷ integrated divergence of the vector field. Our new result from equation (S24) connects
¹⁵⁸ the instantaneous (i.e., $\tau \rightarrow 0$) volume change to the median perturbation growth rate
¹⁵⁹ (\bar{r}_τ).

¹⁶⁰ S4 Stability metrics under time-delay embedding

¹⁶¹ The stability metrics introduced in this study are based on the Jacobian matrix con-
¹⁶² taining all relevant state variables (e.g., all species present in a population dynamics
¹⁶³ model). However, as mentioned in the Discussion section of the main text, when in-
¹⁶⁴ ferring this matrix from empirical data, there are always relevant state variables (e.g.,
¹⁶⁵ species, traits, genes) that are not observed. In this section, we focus on the discrete-time
¹⁶⁶ Jacobian matrix to understand how using time-delay embedding (i.e., Takens' Theorem;
¹⁶⁷ [Takens \(1981\)](#)) to account for unobserved state variables can affect the stability metrics.

¹⁶⁸ To simplify the notation, we assume without loss of generality that the discrete-time
¹⁶⁹ dynamics occur on a time step of $\Delta t = 1$. Thus, the generic model for species i is given
¹⁷⁰ by $N_i(t+1) = F_i(N_1(t), \dots, N_S(t))$. The Jacobian matrix containing all S state variables
¹⁷¹ is given by

$$\mathbf{J}_F = \begin{bmatrix} \frac{\partial N_1(t+1)}{\partial N_1(t)} & \dots & \frac{\partial N_1(t+1)}{\partial N_S(t)} \\ \vdots & \ddots & \vdots \\ \frac{\partial N_S(t+1)}{\partial N_1(t)} & \dots & \frac{\partial N_S(t+1)}{\partial N_S(t)} \end{bmatrix}. \quad (\text{S25})$$

¹⁷² This matrix is typically called the Jacobian matrix in native coordinates. One approach

to deal with the problem of unobserved state variables is to work with a single species i and a Jacobian matrix based on time-delay embedding (Grziwotz *et al.*, 2023, Rogers *et al.*, 2022, 2023). That is, if we have data on species i , we can create delay coordinates by taking $E + 1$ lagged versions of the abundance of this species. Under certain conditions, Takens' Theorem guarantees a one-to-one mapping between an attractor in native coordinates and in delay coordinates (Takens, 1981). For more information on time-delay embedding and its applications to ecology see Munch *et al.* (2020, 2023). The Jacobian matrix in delay coordinates for species i is given by

$$\mathbf{J}_{DF} = \begin{bmatrix} \frac{\partial N_i(t+1)}{\partial N_i(t)} & \frac{\partial N_i(t+1)}{\partial N_i(t-1)} & \frac{\partial N_i(t+1)}{\partial N_i(t-2)} & \cdots & \frac{\partial N_i(t+1)}{\partial N_S(t-E)} \\ 1 & 0 & 0 & \cdots & 0 \\ 0 & 1 & 0 & \cdots & 0 \\ \vdots & \vdots & \ddots & \ddots & \vdots \\ 0 & 0 & \cdots & 1 & 0 \end{bmatrix}. \quad (\text{S26})$$

Thus, an important question is how this matrix can impact the stability metrics ($\min[r_\tau]$, \bar{r}_τ , and $\max[r_\tau]$).

S4.1 Eigenvalues and singular values

We first provide some mathematical results related to the eigenvalues and singular values of the state-transition matrix (Φ) under time-delay embedding. Recall that the log of the largest singular value of Φ is used to compute the maximum perturbation growth rate ($\max[r_\tau]$). Also, recall from Section S3 that the largest eigenvalue of Φ (in absolute value) is a lower bound to its largest singular value. We start by exploring the case of short time scales (i.e., $\tau = 1$) and then explore the case of long time scales (i.e., $\tau = n$, where n is large).

Time-delay embedding involves a one-to-one and invertible transformation \mathbf{G} from the S -dimensional space of all state variables (e.g., $\mathbf{N}(t) = [N_1(t), \dots, N_S(t)]^\top$) to the $(E + 1)$ -dimensional delay-coordinate space ($\mathbf{N}_{DF}(t) = [N_i(t), N_i(t - 1), \dots, N_i(t - E)]$). That is, $\mathbf{N}_{DF}(t) = \mathbf{G}(\mathbf{N}(t))$. Therefore, for the pulse perturbation $\mathbf{x}(t)$, we have that $\mathbf{x}_{DF}(t) = \mathbf{J}_G(t)\mathbf{x}(t)$, where $\mathbf{J}_G(t)$ is the Jacobian matrix of \mathbf{G} evaluated at $\mathbf{N}_{DF}(t)$. With this in mind, we can consider the linear dynamics of a pulse perturbation for $\tau = 1$ (i.e., from $t = 0$ to $t = 1$) in delay coordinates. We have that

$$\begin{aligned} \mathbf{x}_{DF}(1) &= \mathbf{J}_G(1)\mathbf{J}_F(0)\mathbf{x}(0) \\ &= \mathbf{J}_G(1)\mathbf{J}_F(0)\mathbf{J}_G(0)^{-1}\mathbf{x}_{DF}(0), \end{aligned} \quad (\text{S27})$$

where $\mathbf{J}_{DF}(0) = \mathbf{J}_G(1)\mathbf{J}_F(0)\mathbf{J}_G(0)^{-1}$ is the state-transition matrix in delay coordinates that connects $\mathbf{x}_{DF}(0)$ to $\mathbf{x}_{DF}(1)$. Thus, an important question about equation (S27) is whether the eigenvalues and singular values of $\mathbf{J}_G(1)\mathbf{J}_F(0)\mathbf{J}_G(0)^{-1}$ are close to the eigenvalues and singular values of $\mathbf{J}_F(0)$ (i.e., the state-transition matrix in native coor-

dinates). Because τ is small, $\mathbf{J}_G(1)$ and $\mathbf{J}_G(0)$ will be approximately the same matrix, that is: $\mathbf{J}_G(1)\mathbf{J}_F(0)\mathbf{J}_G(0)^{-1} \approx \mathbf{A}\mathbf{J}_F(0)\mathbf{A}^{-1}$. Because $\mathbf{A}\mathbf{J}_F(0)\mathbf{A}^{-1}$ is a similarity transformation, the eigenvalues of $\mathbf{A}\mathbf{J}_F(0)\mathbf{A}^{-1}$ and $\mathbf{J}_F(0)$ are the same. As a consequence, their determinant and trace are also the same. Therefore, if τ is small, the eigenvalues (as well as determinant and trace) of the state-transition matrix in delay coordinates are expected to be close to the eigenvalues of the state-transition matrix in native coordinates. Regarding singular values, we would need \mathbf{A} to be an orthogonal matrix for the singular values of $\mathbf{A}\mathbf{J}_F(0)\mathbf{A}^{-1}$ and $\mathbf{J}_F(0)$ to be the same, which is a stronger condition.

We now explore the case of a long time scale. We start by incorporating another time step to equation (S27):

$$\begin{aligned}\mathbf{x}_{DF}(2) &= \mathbf{J}_G(2)\mathbf{J}_F(1)\mathbf{J}_G(1)^{-1}\mathbf{J}_G(1)\mathbf{J}_F(0)\mathbf{J}_G(0)^{-1}\mathbf{x}_{DF}(0) \\ &= \mathbf{J}_G(2)\mathbf{J}_F(1)\mathbf{J}_F(0)\mathbf{J}_G(0)^{-1}\mathbf{x}_{DF}(0).\end{aligned}\quad (\text{S28})$$

Repeating this procedure n times, we obtain

$$\mathbf{x}_{DF}(n) = \mathbf{J}_G(n)\Phi_F\mathbf{J}_G(0)^{-1}\mathbf{x}_{DF}(0), \quad (\text{S29})$$

where $\Phi_F = \mathbf{J}_F(t_{n-1}) \cdots \mathbf{J}_F(t_0)$ is the state-transition matrix that connects $\mathbf{x}(0)$ to $\mathbf{x}(n)$ and $\mathbf{J}_G(n)\Phi_F\mathbf{J}_G(0)^{-1}$ is the state-transition matrix that connects $\mathbf{x}_{DF}(0)$ to $\mathbf{x}_{DF}(n)$. The important point here is that the Jacobian matrices for all intermediate transformations cancel out. Thus, when the product that makes up Φ_F is large, $\mathbf{J}_G(n)$ and $\mathbf{J}_G(0)^{-1}$ will have a negligible impact. This implies that the largest singular value of $\mathbf{J}_G(n)\Phi_F\mathbf{J}_G(0)^{-1}$ and of Φ_F will be close to each other. Therefore, $\max[r_\tau]$ computed for a long time scale (i.e., Lyapunov exponent) under delay coordinates will be close to $\max[r_\tau]$ computed under native coordinates. This is a well-known result of the theory of Lyapunov exponents (Argyris *et al.*, 2015, Datseris & Parlitz, 2022). However, this is not true for short time scales (e.g., $\tau = 1$ as in equation (S27)), for which the impact of the transformation is relevant. For this short-term case, $\max[r_\tau]$ computed under delay coordinates can be very different from $\max[r_\tau]$ computed under native coordinates.

S4.2 Constraint on singular values

We now prove that, under a single time step (i.e., from $t = 0$ to $t = 1$), the log of the largest singular value of $\mathbf{J}_{DF}(0)$ is always greater than 0. This constraint illustrates further how $\max[r_\tau]$ computed under delay coordinates can be very different from $\max[r_\tau]$ computed under native coordinates. As mentioned above, for $\tau = 1$ we have that $\mathbf{J}_{DF}(0) = \mathbf{J}_G(1)\mathbf{J}_F(0)\mathbf{J}_G(0)^{-1}$ is the state-transition matrix connecting $\mathbf{x}_{DF}(0)$ to $\mathbf{x}_{DF}(1)$. To simplify the notation, we will denote $\mathbf{J}_{DF}(0)$ as \mathbf{J}_{DF} .

²³² The matrix $\mathbf{J}_{DF}\mathbf{J}_{DF}^\top$ is given by

$$\mathbf{J}_{DF}\mathbf{J}_{DF}^\top = \begin{bmatrix} \sum_{j=1}^E \left(\frac{\partial N_i(t+1)}{\partial N_i(t-j)}\right)^2 & \frac{\partial N_i(t+1)}{\partial N_i(t)} & \frac{\partial N_i(t+1)}{\partial N_i(t-1)} & \cdots & \frac{\partial N_i(t+1)}{\partial N_S(t-E+1)} \\ \frac{\partial N_i(t+1)}{\partial N_i(t)} & 1 & 0 & \cdots & 0 \\ \frac{\partial N_i(t+1)}{\partial N_i(t-1)} & 0 & 1 & \cdots & 0 \\ \vdots & \vdots & \ddots & \ddots & \vdots \\ \frac{\partial N_i(t+1)}{\partial N_i(t-E+1)} & 0 & \cdots & 0 & 1 \end{bmatrix}. \quad (\text{S30})$$

²³³ Now, we proceed by calculating the eigenvalues of $\mathbf{J}_{DF}\mathbf{J}_{DF}^\top$, which are the squared singular
²³⁴ values of \mathbf{J}_{DF} . This matrix has a simple block structure of the form

$$\mathbf{J}_{DF}\mathbf{J}_{DF}^\top = \begin{bmatrix} s & \mathbf{b}^\top \\ \mathbf{b} & \mathbf{I} \end{bmatrix}. \quad (\text{S31})$$

²³⁵ The eigenvalues of this matrix satisfy

$$\det \left(\begin{bmatrix} s - \lambda & \mathbf{b}^\top \\ \mathbf{b} & \mathbf{I}(1 - \lambda) \end{bmatrix} \right) = 0. \quad (\text{S32})$$

²³⁶ Making use of the block structure and matrix determinant lemma, this reduces to

$$(s - \lambda)(1 - \lambda)^{E-1}[(s - \lambda)(1 - \lambda) - \mathbf{b}^\top \mathbf{b}] = 0. \quad (\text{S33})$$

²³⁷ The rightmost term shows that the largest eigenvalue of $\mathbf{J}_{DF}\mathbf{J}_{DF}^\top$ (and hence the largest
²³⁸ singular value of \mathbf{J}_{DF}) is greater than 1. Rearranging this we have $\lambda^2 - (s+1)\lambda + s - \mathbf{b}^\top \mathbf{b} =$
²³⁹ 0. The easiest way to see that the positive root must be greater than 1 is to note that
²⁴⁰ $f(\lambda) = \lambda^2 - (s+1)\lambda + s - \mathbf{b}^\top \mathbf{b}$ has a minimum at $\lambda^* = (s+1)/2$ and that $f(\lambda^*) < 0$. From
²⁴¹ here, $f(\lambda)$ increases monotonically and since $f(1) = -\mathbf{b}^\top \mathbf{b} < 0$ the root (i.e., $f(\lambda) = 0$)
²⁴² must be to the right at some λ greater than 1. Therefore, the log of the largest singular
²⁴³ value of \mathbf{J}_{DF} will always be greater than 0.

²⁴⁴ In contrast to singular values, there are no constraints on the eigenvalues of \mathbf{J}_{DF} .
²⁴⁵ Using the cofactor formula for determinants, we can show that the eigenvalues of \mathbf{J}_{DF}
²⁴⁶ will be given by the roots of the following n -degree polynomial:

$$\lambda^n - \frac{\partial N_i(t+1)}{\partial N_i(t)} \lambda^{n-1} - \frac{\partial N_i(t+1)}{\partial N_i(t-1)} \lambda^{n-2} - \cdots - \frac{\partial N_i(t+1)}{\partial N_S(t-E+1)} \lambda - \frac{\partial N_i(t+1)}{\partial N_S(t-E)} = 0. \quad (\text{S34})$$

²⁴⁷ This is a generic polynomial with the j th coefficient given by $\frac{\partial N_i(t+1)}{\partial N_i(t-j)}$. Because there are
²⁴⁸ no constraints on the values of these partial derivatives, there are no constraints on the
²⁴⁹ values of the polynomial roots (i.e., the eigenvalues).

250 **S5 Accuracy of stability metrics under discrete-time
251 models**

252 Here, we report additional tests of the stability metrics (\bar{r}_τ , $\max[r_\tau]$, and $\min[r_\tau]$
253 (equations (21), (22), and (23) in the main text) under two discrete-time models. The
254 first model consists of a 2-species predator-prey model (Zhang *et al.*, 2018). Several 2-
255 species models could be explored for this analysis. We decided to use this model because
256 it contains the Crowley-Martin functional response instead of the Holling Type II function
257 response used in the main text models. The model is given by

$$\begin{aligned} N_1(t+1) &= N_1(t) \left[1 + \tau \left[a - N_1(t) - \frac{bN_2(t)}{(1 + \alpha N_1(t))(1 + \beta N_2(t))} \right] \right] \\ N_2(t+1) &= N_2(t) \left[1 + \tau \left[-c + \frac{dN_1(t)}{(1 + \alpha N_1(t))(1 + \beta N_2(t))} \right] \right], \end{aligned} \quad (\text{S35})$$

258 where N_1 is the abundance of the resource species and N_2 is the abundance of the con-
259 sumer species. We analyze this model under a limit cycle with period 5, that is, recurrence
260 time $T = 5$. Description of parameters and their values are given in Table S1.

261 The second model consists of the population dynamics of flour beetles (*Tribolium* sp)
262 with three different life stages (Costantino *et al.*, 1997). Thus, this is a model with three
263 state variables that are life stages instead of species. This model has been extensively
264 explored both theoretically and experimentally (Costantino *et al.*, 1997). The model is
265 given by

$$\begin{aligned} N_1(t+1) &= bN_3(t) \exp[-c_{el}N_1(t) - c_{ea}N_3(t)] \\ N_2(t+1) &= (1 - \mu_l)N_1(t) \\ N_3(t+1) &= N_2(t) \exp[-c_{pa}N_3(t)] + N_3(t)(1 - \mu_a), \end{aligned} \quad (\text{S36})$$

266 where N_1 is the abundance of feeding larvae, N_2 is the abundance of large larvae, non-
267 feeding larvae, pupae, and callow adults combined, and N_3 is the abundance of sexually
268 mature adults. We analyze this model under a chaotic attractor with recurrence time
269 $T = 3$. Description of parameters and their values are given in Table S1.

270 For both models, we conducted the analysis described in the main text (see Section
271 *Accuracy of stability metrics*). We used $c = 3$ and $c = 5$ recurrences for the predator-prey
272 and larvae-pupae-adult, respectively, to generate the unperturbed trajectory of species
273 abundances $\{\tilde{N}(t)\}$, $t = 0, \dots, cT$. We computed the three metrics ($\min[r_\tau]$, \bar{r}_τ , and
274 $\max[r_\tau]$) from the analytical Jacobian matrix of each system evaluated along the unper-
275 turbed trajectory. Then, we selected three states with low, medium, and high \bar{r}_τ in the
276 short term (i.e., small τ) (top panels in Fig. S2). We then applied pulse perturbations,
277 evolved perturbed abundances for cT time steps, and computed r_τ (equation (S3)) at
278 different τ .

279 The stability metrics accurately captured the growth rate of simulated perturbations
280 for the two discrete-time models and all three states (Fig. S2). Similarly to the results for
281 continuous-time models (Fig. 3), $\min[r_\tau]$ only accurately captured the minimum pertur-
282 bation growth rate for the larvae-pupae-adult model under short time scales (e.g., $\tau = 1$).
283 This apparent discrepancy between $\min[r_\tau]$ and the minimum growth rate observed in
284 the simulations is a result of the long-tailed distribution of r_τ for large τ . Hence, as seen
285 with continuous-time models, $\min[r_\tau]$ is a less relevant metric at long time scales.

286 **S6 Exploring effects of parameter changes on stabil- 287 ity metrics**

288 Stability metrics like \bar{r}_τ can provide new insights when analyzing population dynamics
289 models like the Rosenzweig-MacArthur model (main text equation (24)), which exhibits
290 the “paradox of enrichment.” The paradox arises because increasing the carrying ca-
291 pacity K in the model can induce a Hopf bifurcation—a shift from a stable equilibrium
292 point to a limit cycle (McCann, 2011). On the limit cycle, abundances can become very
293 small; therefore, “enriching” the community (i.e., increasing K) makes extinctions more
294 likely (Rosenzweig & MacArthur, 1963). Changes in the resource intrinsic growth rate
295 r , however, do not generate a bifurcation, but instead alter properties of the equilibrium
296 point or limit cycle (McCann, 2011).

297 We conducted an analysis to investigate how changes in K and r would impact the
298 median perturbation growth rate (\bar{r}_τ) for a short time scale under the equilibrium point
299 and limit cycle regimes. With our parameterization (Table S1), the Hopf bifurcation
300 occurs at $K_H = 1.56$. Below this value of K , the community converges to a stable
301 equilibrium point \mathbf{N}^* . We quantified \bar{r}_τ at \mathbf{N}^* to verify how changes in K and r affect
302 perturbation growth rate. We found that high values of K and intermediate values of r
303 create the most unstable situations (i.e., highest values of \bar{r}_τ ; Fig. S13a).

304 For $K > K_H$, the community converges to a limit cycle instead of an equilibrium point.
305 Because the stability metrics derived here apply to both equilibrium and nonequilibrium
306 dynamics, they allow us to study how pulse perturbations amplify on both sides of the
307 Hopf bifurcation. As in the equilibrium case, large values of K imply large positive
308 values of \bar{r}_τ (Fig. S13b). However, large (rather than intermediate) values of r imply
309 large values of \bar{r}_τ (Fig. S13b). This result provides a new insight into the “paradox of
310 enrichment”, where increasing K and r beyond the Hopf bifurcation creates a highly
311 unstable location along the limit cycle, where the resource abundance is small, making it
312 especially vulnerable to extinction. This result could not have been predicted from our
313 knowledge about how K and r affect \bar{r}_τ under equilibrium dynamics (Fig. S13a).

314 S7 Inference of stability metrics from time-series data

315 As mentioned in Box 2 in the main text, several statical approaches based on regression
 316 models have been used to infer stability metrics from abundance time series (Cenci &
 317 Saavedra, 2019, Grziwotz *et al.*, 2023, Hampton *et al.*, 2013, Ives *et al.*, 2003, Medeiros
 318 *et al.*, 2023, Nguyen *et al.*, 2025, Rogers *et al.*, 2023, Ushio *et al.*, 2018). In this section,
 319 we explain our approaches to perform this task, which consist of the S-map model (Deyle
 320 *et al.*, 2016, Sugihara, 1994) and an extension of this model to continuous-time population
 321 dynamics.

322 S7.1 S-map model

323 We start by describing the standard S-map model (Deyle *et al.*, 2016, Sugihara, 1994).
 324 This statistical model assumes that the population dynamics for species i follows a generic
 325 discrete-time model (equation (2) in the main text):

$$N_i(t + \Delta t) = F_i(N_1(t), \dots, N_S(t)). \quad (\text{S37})$$

326 Without loss of generality, we will assume throughout this section that the time step of
 327 the discrete-time dynamics is $\Delta t = 1$. If we have time-series data for all S interacting
 328 species $\{N_i(t)\}$ ($i = 1, \dots, S$; $t = 0, 1, \dots, T$), the simplest statistical model for F_i is the
 329 following linear regression model:

$$N_i(t + 1) = \beta_{i0} + \sum_{j=1}^S \beta_{ij} N_j(t) + \epsilon_i(t), \quad (\text{S38})$$

330 where β_{ij} ($j = 0, \dots, S$) are the model coefficients and $\epsilon_i(t)$ is the error for species i at
 331 time t . Note that equation (S38) corresponds to a vector autoregressive model of order 1
 332 (i.e., VAR(1); Ives *et al.* (2003)). This equation can be written in matrix form as:

$$\mathbf{y}_i = \mathbf{X}\boldsymbol{\beta}_i + \boldsymbol{\epsilon}_i, \quad (\text{S39})$$

333 where

$$\mathbf{y}_i = \begin{bmatrix} N_i(1) \\ N_i(2) \\ \vdots \\ N_i(T) \end{bmatrix}, \mathbf{X} = \begin{bmatrix} 1 & N_1(0) & \cdots & N_S(0) \\ 1 & N_1(1) & \cdots & N_S(1) \\ \vdots & \vdots & \ddots & \vdots \\ 1 & N_1(T-1) & \cdots & N_S(T-1) \end{bmatrix}, \boldsymbol{\beta}_i = \begin{bmatrix} \beta_{i0} \\ \beta_{i1} \\ \vdots \\ \beta_{iS} \end{bmatrix}, \text{ and } \boldsymbol{\epsilon}_i = \begin{bmatrix} \epsilon_i(0) \\ \epsilon_i(1) \\ \vdots \\ \epsilon_i(T-1) \end{bmatrix}. \quad (\text{S40})$$

334 Note that the model can be written for all S species at once by concatenating \mathbf{y}_i vectors,
 335 $\boldsymbol{\beta}_i$ vectors, and $\boldsymbol{\epsilon}_i$ vectors into matrices (Nguyen *et al.*, 2025).

336 Given that F_i is typically nonlinear, we can fit this regression model for each fo-
 337 cal time t^* separately, assigning a weight $w(t)$ to each time t based on the Euclidean

338 distance between $\mathbf{N}(t)$ and $\mathbf{N}(t^*)$ (Deyle *et al.*, 2016, Sugihara, 1994), where $\mathbf{N}(t) =$
 339 $[N_1(t), \dots N_S(t)]^\top$. By giving a stronger weight to the closest neighbors of $\mathbf{N}(t^*)$ in state
 340 space, this setup allows us to capture nonlinearities in F_i . Specifically, the S-map model
 341 uses the following weighting kernel:

$$w(t) = \exp \left[-\theta \frac{\|\mathbf{N}(t) - \mathbf{N}(t^*)\|}{\bar{d}} \right], \quad (\text{S41})$$

342 where θ controls how weights decay with distance (i.e., the degree of nonlinearity of the
 343 model) and $\bar{d} = \frac{1}{T} \sum_{t=0}^{T-1} \|\mathbf{N}(t) - \mathbf{N}(t^*)\|$ is the average distance between $\mathbf{N}(t^*)$ and all
 344 other states. It is important to note that several recurrences of the system (e.g., several
 345 seasonal cycles) need to be present in the time-series data. Without such recurrences,
 346 there will not be enough neighbors for any given $\mathbf{N}(t^*)$ and the S-map model will not
 347 accurately represent F_i locally. Also note that an alternative implementation of the
 348 weighting kernel related to dynamic linear models (DLM) is for $w(t)$ to depend on distance
 349 in time (i.e., $|t - t^*|$) (Deyle *et al.*, 2016, Hampton *et al.*, 2013, Nguyen *et al.*, 2025). The
 350 S-map coefficients at each focal time t^* (i.e., $\beta_{ij}(t^*)$) can be estimated via least squares,
 351 as explained in Section S7.3.

352 Importantly, the estimated coefficients of this weighted regression model correspond
 353 to the discrete-time Jacobian matrix elements evaluated at $\mathbf{N}(t^*)$ (Deyle *et al.*, 2016):

$$[\hat{\mathbf{J}}_F]_{ij}(t^*) = \frac{\partial \hat{F}_i}{\partial N_j}(t^*) = \hat{\beta}_{ij}(t^*). \quad (\text{S42})$$

354 It is also important to note that, if continuous-time population dynamics generated the
 355 time-series data, the inferred S-map coefficients contain information about the continuous-
 356 time Jacobian matrix. That is, if $\mathbf{J}_f(t^*)$ is almost constant between t^* and $t^* + 1$, then
 357 we have the following relationship between $\mathbf{J}_f(t^*)$ and $\mathbf{J}_F(t^*)$ (equation (16) in the main
 358 text):

$$\mathbf{J}_F(t^*) \approx \exp[\mathbf{J}_f(t^*)], \quad (\text{S43})$$

359 After inferring $\mathbf{J}_F(t^*)$ for all times t^* , we can then compute the discrete-time state-
 360 transition matrix Φ_F (equation (14) in the main text) and stability metrics (equations
 361 (21), (22), and (23) in the main text).

362 Lastly, note that the S-map model can also be implemented with time-delay embed-
 363 ding by using lagged versions of the abundance of species i (i.e., $N_i(t), N_i(t-1), \dots, N_i(t-E)$)
 364 on the right-hand side of equation (S38) (Rogers *et al.*, 2022, 2023). This allows us
 365 to infer the Jacobian matrix in delay coordinates (equation (S26)) and use this matrix to
 366 compute stability metrics (Section S4).

367 S7.2 S-map model for continuous-time population dynamics

368 The standard S-map model described above can be extended in different ways by
 369 making different assumptions about the underlying population dynamics (Nguyen *et al.*,
 370 2025, Rogers *et al.*, 2022, Suzuki *et al.*, 2017). Here, we describe an extension that
 371 is similar to previous approaches (Stein *et al.*, 2013, Suzuki *et al.*, 2017) and assumes
 372 continuous-time dynamics. Specifically, we assume that population dynamics are given
 373 by

$$\frac{dN_i(t)}{dt} = N_i(t)g_i(N_1(t), \dots, N_S(t)), \quad (\text{S44})$$

374 where g_i is a function describing the per capita growth rate of species i . Note that
 375 multiple population dynamics models follow this general structure (e.g., equations (24)
 376 and (25) in the main text). If such continuous-time dynamics generated the time-series
 377 data, then we can leverage the structure of equation (S44) to infer the continuous-time
 378 Jacobian matrix $\mathbf{J}_f(t^*)$. Note that we can extend the S-map model in a very similar way
 379 by assuming the following discrete-time model (Nguyen *et al.*, 2025):

$$N_i(t+1) = N_i(t) \exp[G_i(N_1(t), \dots, N_S(t))]. \quad (\text{S45})$$

380 If sampling time intervals are small compared to the generation time of the organisms
 381 (Munch *et al.*, 2020), we can integrate both sides of equation (S44) assuming that they
 382 are constant between t and $t + 1$. Thus, we can fit the following linear regression model
 383 to g_i (Stein *et al.*, 2013, Suzuki *et al.*, 2017):

$$g_i(\mathbf{N}(t)) \approx \log \left[\frac{N_i(t+1)}{N_i(t)} \right] = \beta_{i0} + \sum_{j=1}^S \beta_{ij} N_j(t) + \epsilon_i(t). \quad (\text{S46})$$

384 Equation (S46) represents a regression model that has the same predictor variables (i.e.,
 385 right-hand side) but a different response variable (i.e., left-hand side) as the standard
 386 S-map model (equation (S38)). The vector \mathbf{y}_i in equation (S39) then becomes

$$\mathbf{y}_i = \begin{bmatrix} \log \left[\frac{N_i(1)}{N_i(0)} \right] \\ \log \left[\frac{N_i(2)}{N_i(1)} \right] \\ \vdots \\ \log \left[\frac{N_i(T)}{N_i(T-1)} \right] \end{bmatrix}. \quad (\text{S47})$$

387 The S-map weighting kernel (equation (S41)) remains exactly the same under this setup.

388 With this setup, the S-map coefficients correspond to $\beta_{ij}(t^*) = \frac{\partial g_i}{\partial N_j}(t^*)$. To obtain
 389 $\frac{\partial f_i}{\partial N_j}(t^*)$ and build the Jacobian matrix evaluated at $\mathbf{N}(t^*)$, we can leverage the structure

390 of equation (S44) (Song & Saavedra, 2021):

$$[\hat{\mathbf{J}}_f]_{ij}(t^*) = \frac{\partial \hat{f}_i}{\partial N_j}(t^*) = \begin{cases} \hat{\beta}_{ij}(t^*)N_i(t^*) + \hat{g}_i(\mathbf{N}(t^*)), & \text{if } i = j \\ \hat{\beta}_{ij}(t^*)N_i(t^*), & \text{if } i \neq j \end{cases}. \quad (\text{S48})$$

391 Similarly to the standard S-map model, after inferring $\mathbf{J}_f(t^*)$ for all times t^* , we can then
392 compute the continuous-time state-transition matrix Φ_f (equation (12) in the main text)
393 and stability metrics (equations (21), (22), and (23) in the main text).

394 S7.3 Estimation of S-map coefficients

395 The S-map coefficients (i.e., β_{ij}) for both approaches outlined above can be estimated
396 by solving the following general least squares problem (Cenci et al., 2019):

$$\min_{\boldsymbol{\beta}_i} \frac{1}{T} \sum_{t=0}^{T-1} w(t) \left[y_i(t+1) - \left(\beta_{i0} + \sum_{j=1}^S \beta_{ij} N_j(t) \right) \right]^2, \quad (\text{S49})$$

397 where $y_i(t+1) = N_i(t+1)$ or $y_i(t+1) = \log \left[\frac{N_i(t+1)}{N_i(t)} \right]$. The analytical solution of this
398 weighted least squares problem is given by

$$\hat{\boldsymbol{\beta}}_i = (\mathbf{X}^\top \mathbf{W} \mathbf{X})^{-1} \mathbf{X}^\top \mathbf{W} \mathbf{y}_i, \quad (\text{S50})$$

399 where \mathbf{W} is a diagonal matrix with t -th diagonal element being $w(t)$. Standard errors for
400 $\hat{\beta}_{ij}$ can be obtained via conventional methods (Deyle et al., 2016, Nguyen et al., 2025).

401 In cases where we have many species (i.e., large S) but a limited amount of data
402 (i.e., not very large T), adding a regularization to the S-map model can help to avoid
403 collinearity and overfitting issues (Cenci et al., 2019, Chang et al., 2021). The weighted
404 least squares problem with both Ridge and Lasso regularization (i.e., Elastic Net; Hastie
405 et al. (2009)) then becomes

$$\min_{\boldsymbol{\beta}_i} \frac{1}{T} \sum_{t=0}^{T-1} w(t) \left[y_i(t+1) - \left(\beta_{i0} + \sum_{j=1}^S \beta_{ij} N_j(t) \right) \right]^2 + \lambda \left[\frac{1-\alpha}{2} \|\boldsymbol{\beta}_i\|_2^2 + \alpha \|\boldsymbol{\beta}_i\|_1 \right], \quad (\text{S51})$$

406 where λ is the strength of the penalty on coefficients and α is the proportion of Lasso
407 (i.e., L^1 norm) as opposed to Ridge (i.e., L^2 norm) regularization. Equation (S51) can be
408 solved via an optimization algorithm such as cyclic coordinate descent (Tay et al., 2023).

409 We used leave-future-out cross-validation to determine the values of the regularized
410 S-map hyperparameters (i.e., θ , λ , and α ; Cenci et al. (2019), Nguyen et al. (2025)). We
411 performed this analysis in the same way for both S-map setups described above. We
412 started by creating a grid of hyperparameters and performed the following analysis for
413 each combination of θ , λ , and α in the grid. We assigned the first half of the time series
414 as the training set (i.e., $t = 0, \dots, (T/2) - 1$) and the future point as the test set (i.e.,

415 $t = T/2$). For each species i , we standardized N_i in the training set to have mean zero
416 and unit standard deviation. Next, we fit the regularized S-map model (equation (S51))
417 to the training set at focal time $t^* = (T/2) - 1$ and used equation (S38) or (S46) to make
418 a prediction for $N_i(t^* + 1)$. We then iterated this procedure by incorporating the test
419 set point into the training set and assigning the future point as the new test set. For
420 example, in the second iteration, the training set times were $t = 0, \dots, T/2$ and the test
421 set time was $t = (T/2) + 1$. After all iterations, we computed the out-of-sample R^2 as
422 our measure of prediction accuracy:

$$R^2 = 1 - \frac{\sum_{t=T/2}^T [N_i(t) - \hat{N}_i(t)]^2}{\sum_{t=T/2}^T [N_i(t) - \bar{N}_i]^2}, \quad (\text{S52})$$

423 where $\hat{N}_i(t)$ is the S-map prediction for $N_i(t)$ and \bar{N}_i is the average of $N_i(t)$ from $t = T/2$
424 to $t = T$. Because multiple combinations of the hyperparameters can produce very similar
425 R^2 values, we used a parsimony criterion to choose the best combination of θ , λ , and α .
426 We considered all R^2 values within 1% of the highest R^2 to be equivalent and chose the
427 hyperparameters with lowest value from this set of R^2 values. This procedure favors
428 S-map models that are more linear (i.e., lower θ) and less regularized (i.e., lower λ).

429 S7.4 Illustration of stability metrics inference

430 We used stochastic versions of the Rosenzweig-MacArthur ([Rosenzweig & MacArthur, 1963](#)),
431 and Hastings-Powell ([Hastings & Powell, 1991](#)) models to illustrate how to infer
432 stability metrics from abundance time-series data. The Rosenzweig-MacArthur model
433 with process noise is given by

$$\begin{aligned} dN_1 &= N_1 \left[r \left(1 - \frac{N_1}{K} \right) - \frac{aN_2}{b + N_1} \right] dt + \sigma_1 N_1 dW_1 \\ dN_2 &= N_2 \left[\frac{eaN_1}{b + N_1} - d \right] dt + \sigma_2 N_2 dW_2, \end{aligned} \quad (\text{S53})$$

434 where N_1 is the abundance of the resource species and N_2 is the abundance of the con-
435 sumer species (see Table S1 for parameter details). The Hastings-Powell model with
436 process noise is given by

$$\begin{aligned} dN_1 &= N_1 \left[r \left(1 - \frac{N_1}{K} \right) - \frac{a_1 N_2}{b_1 + N_1} \right] dt + \sigma_1 N_1 dW_1 \\ dN_2 &= N_2 \left[\frac{e_1 a_1 N_1}{b_1 + N_1} - d_1 - \frac{a_2 N_3}{b_2 + N_2} \right] dt + \sigma_2 N_2 dW_2 \\ dN_3 &= N_3 \left[\frac{e_2 a_2 N_3}{b_2 + N_2} - d_2 \right] dt + \sigma_3 N_3 dW_3, \end{aligned} \quad (\text{S54})$$

437 where N_1 is the abundance of the resource species, N_2 is the abundance of the consumer
438 species, and N_3 is the abundance of the top predator (see Table S1 for parameter details).
439 In both models, the amount of process noise for species i is given by σ_i , which is the

standard deviation of the Wiener process dW_i . The Wiener process has mean zero and is uncorrelated across species.

To generate time series, we first integrated the system of stochastic differential equations (i.e., equation (S53) or (S54)) using the Euler-Maruyama algorithm. We used $\sigma_i = 0.04 \forall i$ for the Rosenzweig-MacArthur model and $\sigma_i = 0.01 \forall i$ for the Hastings-Powell model. For each species i , this resulted in a time series of $N_i(t)$ with 1,000,000 points. We then sampled equally spaced points to obtain a time series with 150 points (i.e., $t = 0, 1, \dots, 149$). Finally, we added observational noise to the simulated time series. Specifically, for each species i , we added normally distributed noise to $N_i(t)$ with mean zero and standard deviation corresponding to 10% of the standard deviation of $\{N_i(t)\}$ ($t = 0, \dots, 149$). This resulted in the abundance time series with both process and observational noise shown in Figs. 6, S11, S12, and S13.

To infer stability metrics, we followed the procedures described in Sections S7.1 (i.e., standard S-map model) and S7.2 (i.e., S-map model for continuous-time dynamics). Our goal was to follow procedures that we would use with empirical time series and then compare the inferred stability metrics with the true metrics computed using the population dynamics equations (i.e., equation (S53) or (S54)). To do so, we first performed leave-future-out cross-validation to determine the best values for θ , α , and λ . Then, we inferred S-map coefficients (Section S7.3) and computed \bar{r}_τ from the inferred state-transition matrix Φ . Figs. 6 and S11 show the results for the Rosenzweig-MacArthur model, whereas Figs. S12 and S13 show the results for the Hastings-Powell model. Overall, the pattern of the inferred \bar{r}_τ over time closely matched the pattern of the true \bar{r}_τ in those figures. Given that the underlying dynamics was in continuous time, the S-map model for continuous-time dynamics (Figs. 6 and S12) led to more accurate results than the standard S-map model (Figs. S11 and S13), as expected. When working with empirical data, one can determine which S-map setup is more appropriate by comparing their leave-future-out prediction accuracy.

S8 Figures and Tables

Model	Scenario	Parameters
Rosenzweig-MacArthur (main text equation (24))	Equilibrium point with periodic forcing (scenario 1)	$r = 5, K(t) = 1 + 0.5 \sin(0.2\pi t), a = 1.3, b = 1, e = 0.7, d = 0.2$
Rosenzweig-MacArthur (main text equation (24))	Limit cycle (scenario 2)	$r = 5, K = 1.8, a = 1.3, b = 1, e = 0.7, d = 0.2$
Hastings-Powell (main text equation (25))	Limit cycle with nonstationary forcing (scenario 3)	$r = 1, K = 0.99, a_1 = 0.8036, a_2(t) = 0.1984 + 0.000048t, e_1 = 1, e_2 = 1, b_1 = 0.16129, b_2 = 0.5, d_1 = 0.4, d_2 = 0.08$
Hastings-Powell (main text equation (25))	Chaotic attractor (scenario 4)	$r = 1, K = 0.99, a_1 = 0.8036, a_2 = 0.23008, e_1 = 1, e_2 = 1, b_1 = 0.16129, b_2 = 0.5, d_1 = 0.4, d_2 = 0.08$
Discrete-time predator-prey (equation (S35))	Limit cycle	$\tau = 1.1, a = 2, b = 2, \alpha = 0.1, \beta = 0.1, c = 2, d = 1.85$
Discrete-time larvae-pupae-adult (equation (S36))	Chaotic attractor	$b = 6.598, c_{el} = 0.01209, c_{ea} = 0.01155, \mu_l = 0.2055, c_{pa} = 0.35, \mu_a = 0.96$

Table S1. Parameter values for each model and scenario. Description of parameters are as follows. *Rosenzweig-MacArthur model*: r is the resource intrinsic growth rate, K is the resource carrying capacity, a is the consumer attack rate, e is the consumer energy conversion efficiency, b is the half-saturation coefficient, and d is the consumer natural mortality. *Hastings-Powell model*: r is the resource intrinsic growth rate, K is the resource carrying capacity, a_1 (a_2) is the consumer (predator) attack rate, e_1 (e_2) is the consumer (predator) energy conversion efficiency, b_1 (b_2) is the half-saturation coefficient of the consumer (predator), and d_1 (d_2) is the consumer (predator) natural mortality. *Discrete-time predator-prey model*: τ is the time scale of the dynamics, a is the prey intrinsic growth rate, b is the predator attack rate, b/d is the predation conversion factor, α (β) is the magnitude of interference among prey (predators), and c is the predator natural mortality. *Discrete-time larvae-pupae-adult model*: b is the number of larval recruits per adult in the absence of cannibalism, μ_l (μ_a) is the larval (adult) mortality fraction, c_{el} is the rate of cannibalism of eggs by larvae, c_{ea} is the rate of cannibalism of eggs by adults, and c_{pa} is the rate of cannibalism of pupae by adults.

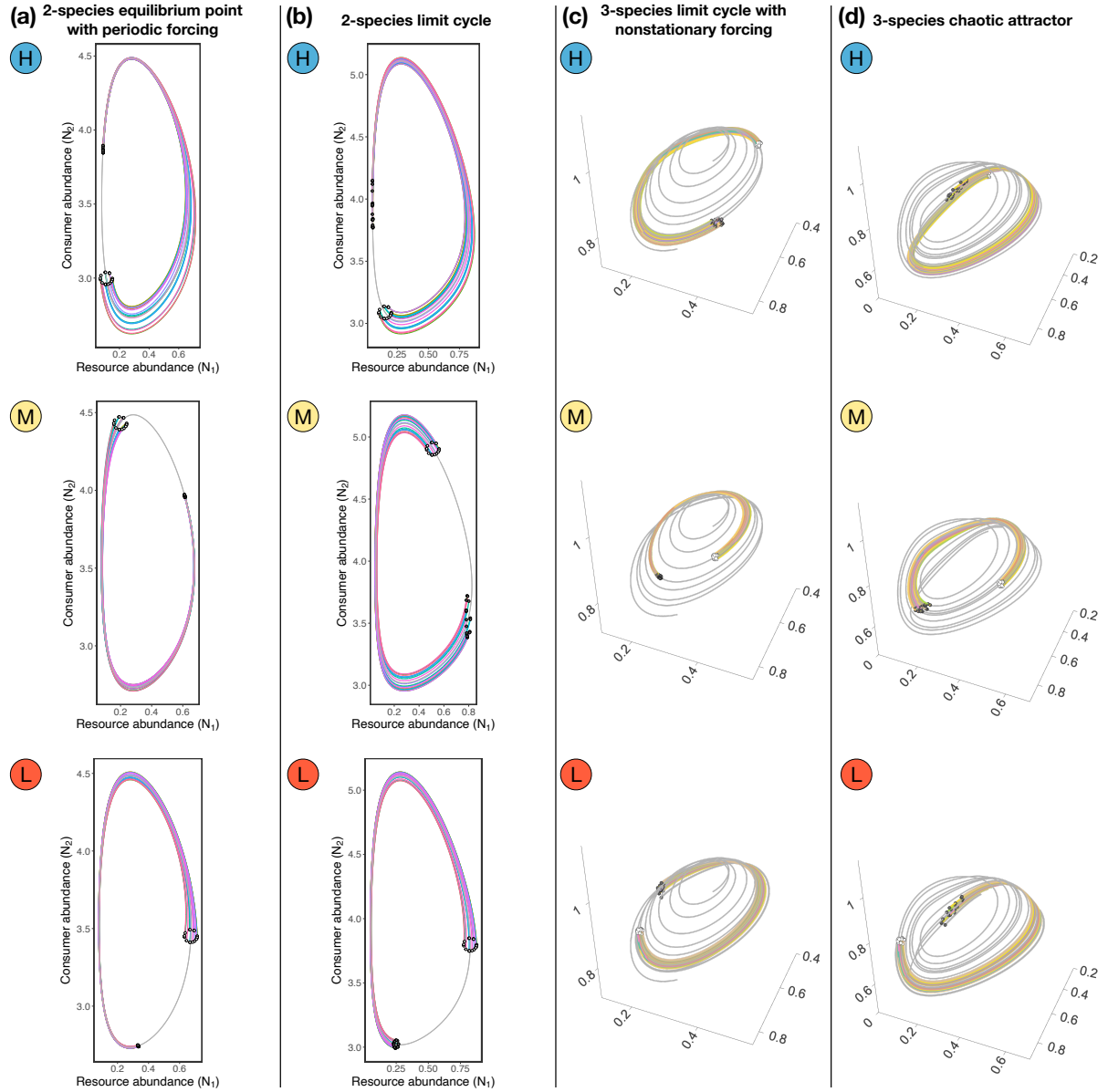


Figure S1. Examples of 20 perturbed abundances $\mathbf{N}(t)$ and their evolution from time $t = 0$ to $t = 0.8T$, where T is the recurrence time of the system. These simulated pulse perturbations are examples of the results shown in Fig. 3 in the main text. White points denote $\mathbf{N}(t)$ at $t = 0$, whereas dark gray points denote $\mathbf{N}(t)$ at $t = 0.8T$. Within each plot, each colored line represents the trajectory of one perturbation and the gray line represents the unperturbed trajectory. Scenarios (a) through (d) are the same as the ones in Fig. 3.

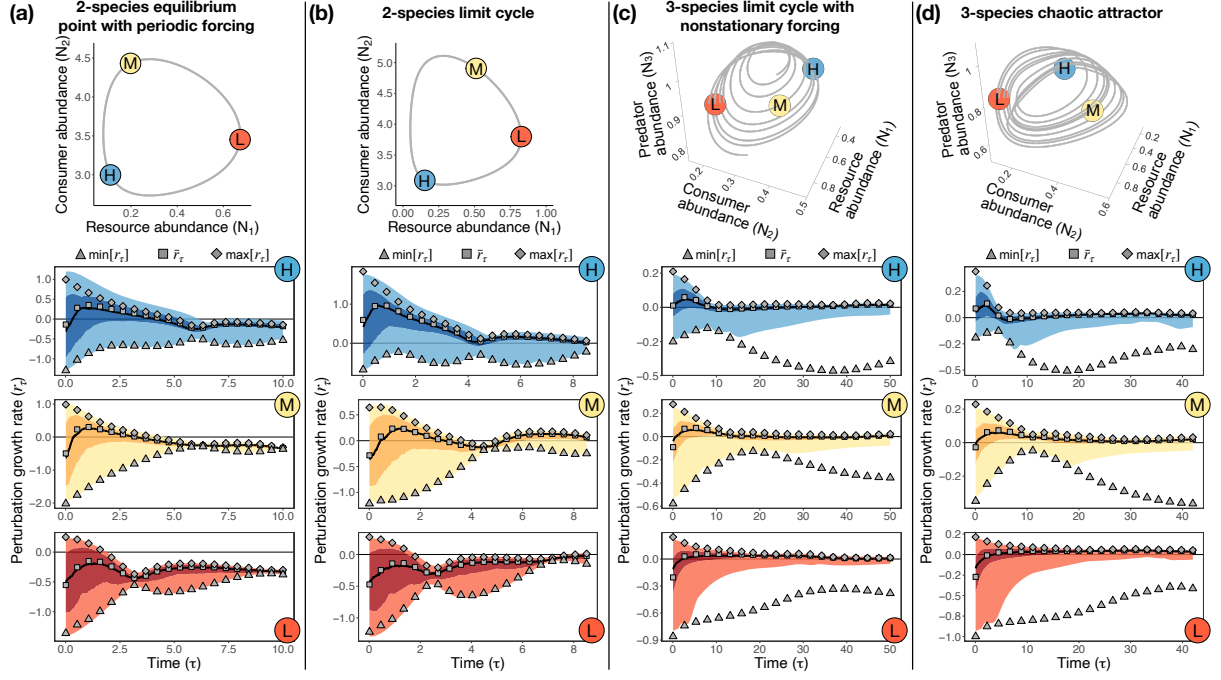


Figure S2. Accuracy of stability metrics under larger perturbation size. For this figure, we set the perturbation size δ to be 20% of the average standard deviation of abundances, instead of 5% as in Fig. 3. Each column (a-d) depicts a scenario, where the top plot shows the trajectory of unperturbed abundances ($\bar{N}(t)$, gray line) and the three bottom plots show the outcome of simulated perturbations (blue, yellow, and red shades) together with the stability metrics as gray points ($\min[r_\tau]$, \bar{r}_τ , and $\max[r_\tau]$). Points labeled as H (in blue), M (in yellow), and L (in red) represent locations along the trajectory with high, medium, and low values of \bar{r}_τ (for small τ), respectively. In bottom plots, the dark shade denotes the region between the 25th and 75th percentiles, whereas the light shade goes to the minimum and maximum values of r_τ . Bottom plots span $t = 0$ to $t = T$, where T denotes the recurrence time of the system. Scenarios (a) through (d) are the same as the ones in Fig. 3.

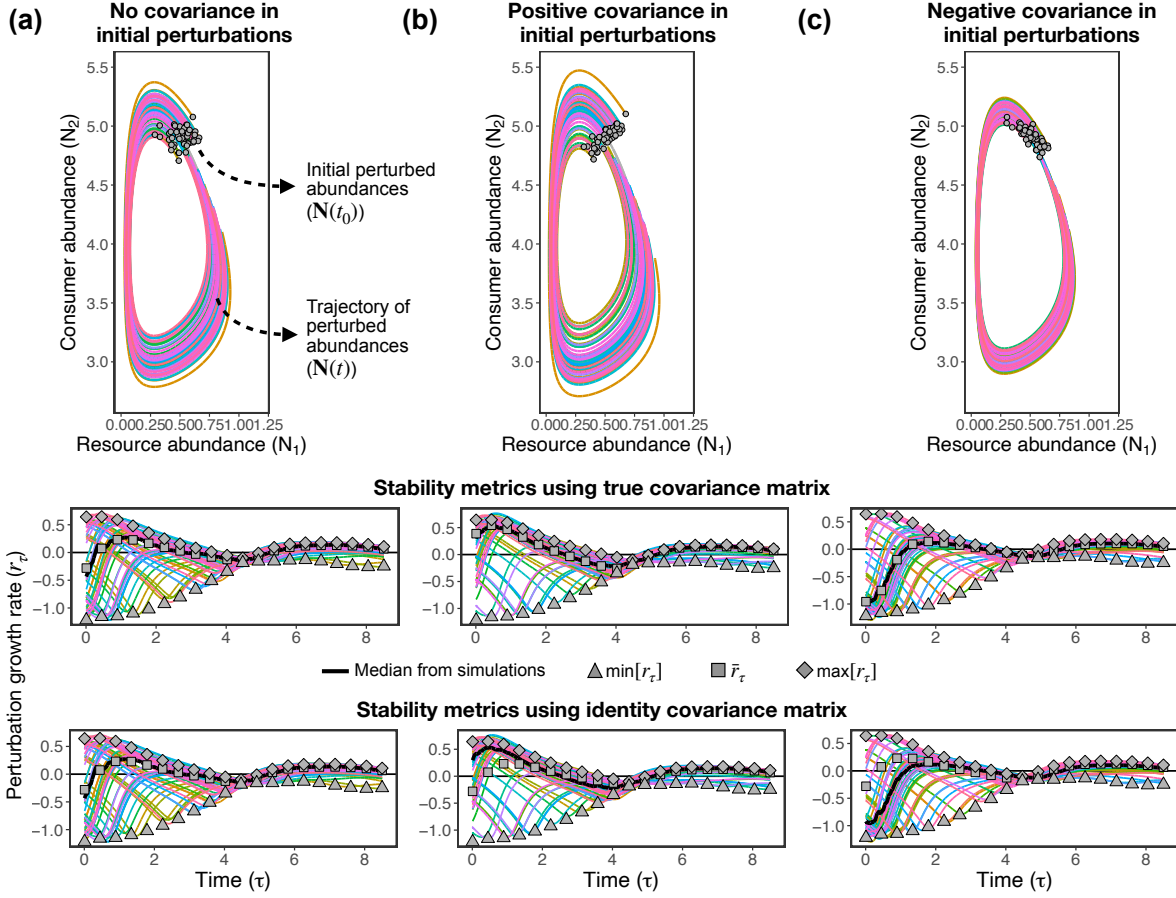


Figure S3. Responses to pulse perturbations for a 2-species resource-consumer model (Rosenzweig-MacArthur model) under different covariance matrices for the initial distribution of perturbations. (a) Covariance matrix proportional to the identity matrix (i.e., perturbations affect each species independently with identical variance). (b) Covariance matrix with the same variances (i.e., diagonal terms) as in (a) but with positive covariances (i.e., off-diagonal terms). (c) Covariance matrix with the same variances (i.e., diagonal terms) as in (a) but with negative covariances (i.e., off-diagonal terms). In (a) through (c), initial perturbations ($\mathbf{x}(t_0)$) follow a multivariate normal distribution with mean zero ($\mu_0 = \mathbf{0}$) and covariance matrix Σ_0 . In top plots, each gray point (total of 50 points) depicts perturbed abundances at t_0 ($\mathbf{N}(t_0)$) and each colored line shows the trajectory over time for each of the gray points. Middle and bottom plots show the perturbation growth rate (r_τ) over time for all 50 simulated perturbations shown in the top plots as colored lines. The thick black line corresponds to the median perturbation growth rate across all simulated perturbations. Gray points are the analytical metrics for the minimum ($\min[r_\tau]$, triangles), median (\bar{r}_τ , squares), and maximum ($\max[r_\tau]$, diamonds) perturbation growth rate. In middle plots \bar{r}_τ is computed using the true Σ_0 , whereas in bottom plots \bar{r}_τ is computed using an identity matrix for Σ_0 . All plots focus on the same initial state (i.e., unperturbed abundances $\tilde{\mathbf{N}}(t_0)$) shown in Fig. 2.

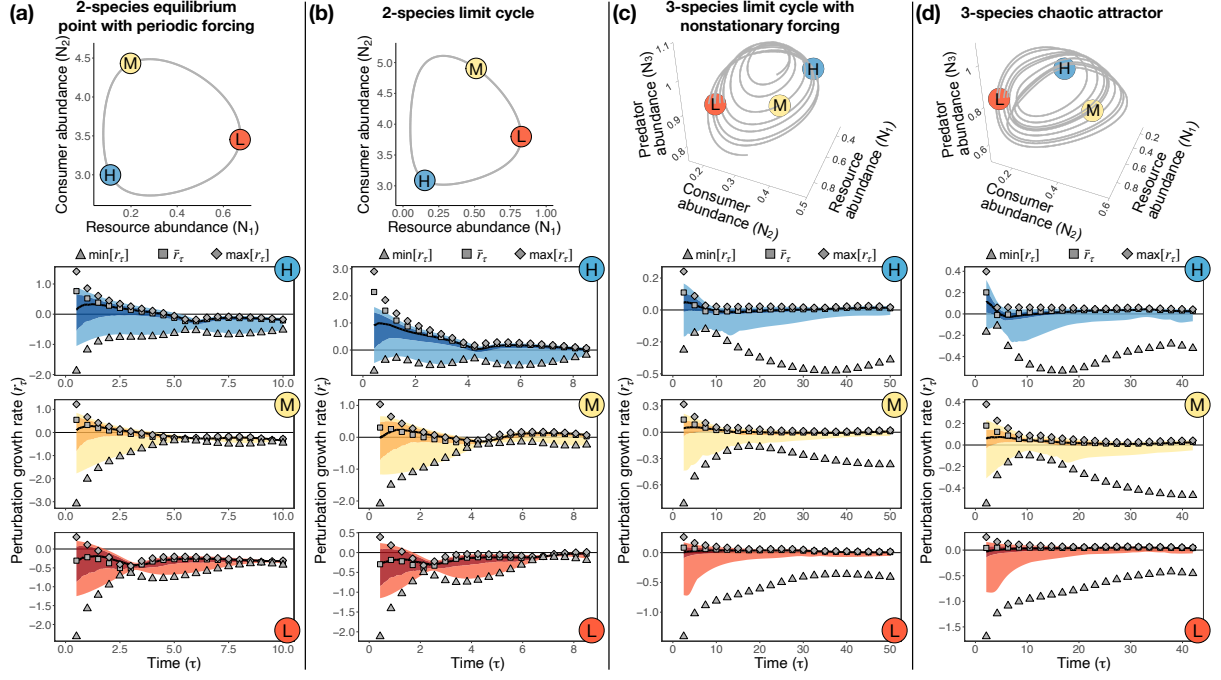


Figure S4. Accuracy of stability metrics using a large time step $t_{i+1} - t_i$ to compute the continuous-time state-transition matrix Φ_f . For this figure, we use a time step $t_{i+1} - t_i$ that is 500 times larger than the small time step used in Fig. 3. Each column (a-d) depicts a scenario, where the top plot shows the trajectory of unperturbed abundances ($\tilde{\mathbf{N}}(t)$, gray line) and the three bottom plots show the outcome of simulated perturbations (blue, yellow, and red shades) together with the stability metrics as gray points ($\min[r_\tau]$, \bar{r}_τ , and $\max[r_\tau]$). Points labeled as H (in blue), M (in yellow), and L (in red) represent locations along the trajectory with high, medium, and low values of \bar{r}_τ (for small τ), respectively. In bottom plots, the dark shade denotes the region between the 25th and 75th percentiles, whereas the light shade goes to the minimum and maximum values of r_τ . Bottom plots span $t = 0$ to $t = T$, where T denotes the recurrence time of the system. Scenarios (a) through (d) are the same as the ones in Fig. 3.

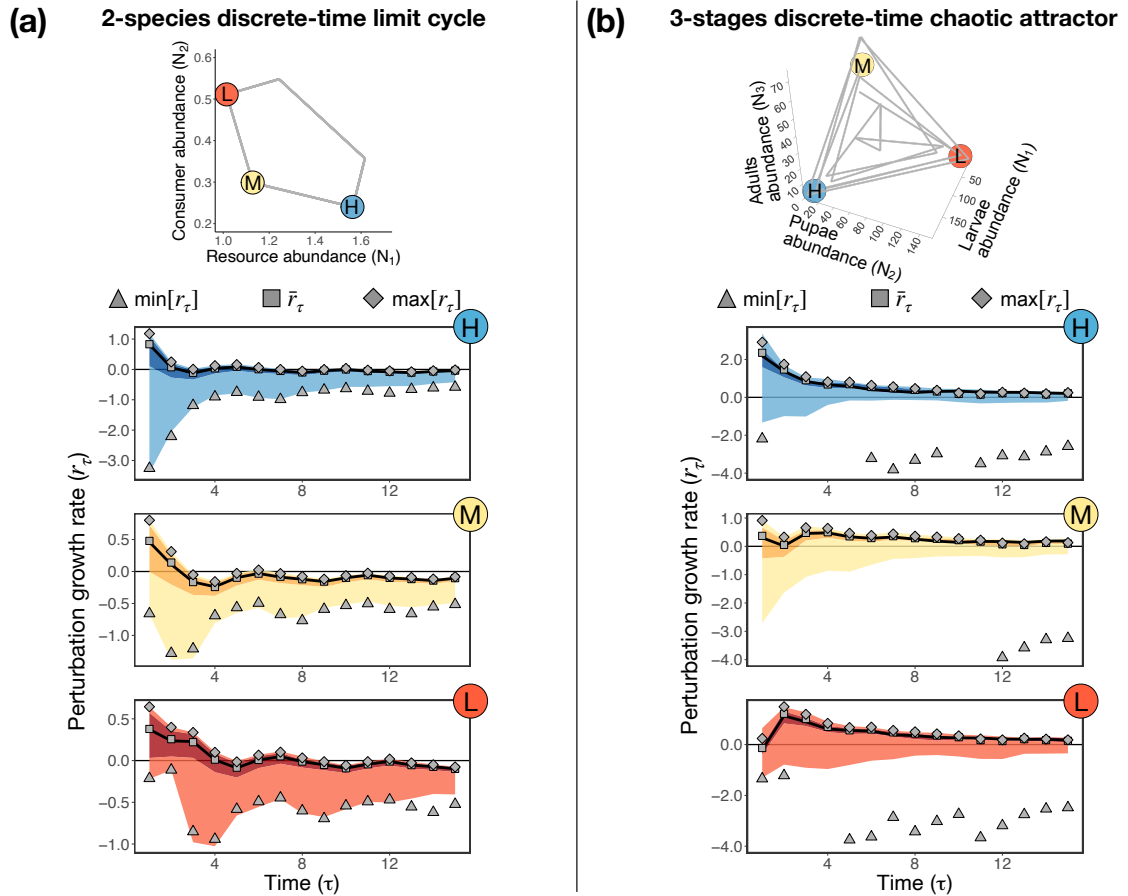


Figure S5. Accuracy of stability metrics under two discrete-time models (equations (S35) and (S36)). Each column (a-b) depicts a model, where the top plot shows the trajectory of unperturbed abundances ($\hat{N}(t)$, gray line) and the three bottom plots show the outcome of simulated perturbations (blue, yellow, and red shades) together with the stability metrics as gray points ($\min[r_\tau]$, \bar{r}_τ , and $\max[r_\tau]$). Points labeled as H (in blue), M (in yellow), and L (in red) represent locations along the trajectory with high, medium, and low values of \bar{r}_τ (for small τ), respectively. In bottom plots, the dark shade denotes the region between the 25th and 75th percentiles, whereas the light shade goes to the minimum and maximum values of r_τ . Recurrence times are $T = 5$ for the system in (a) and $T = 3$ for the system in (b). Note that we set the lower limit of the y-axis to -4 in (b) to improve visualization. Thus, some of the values of $\min[r_\tau]$ are not shown in (b).

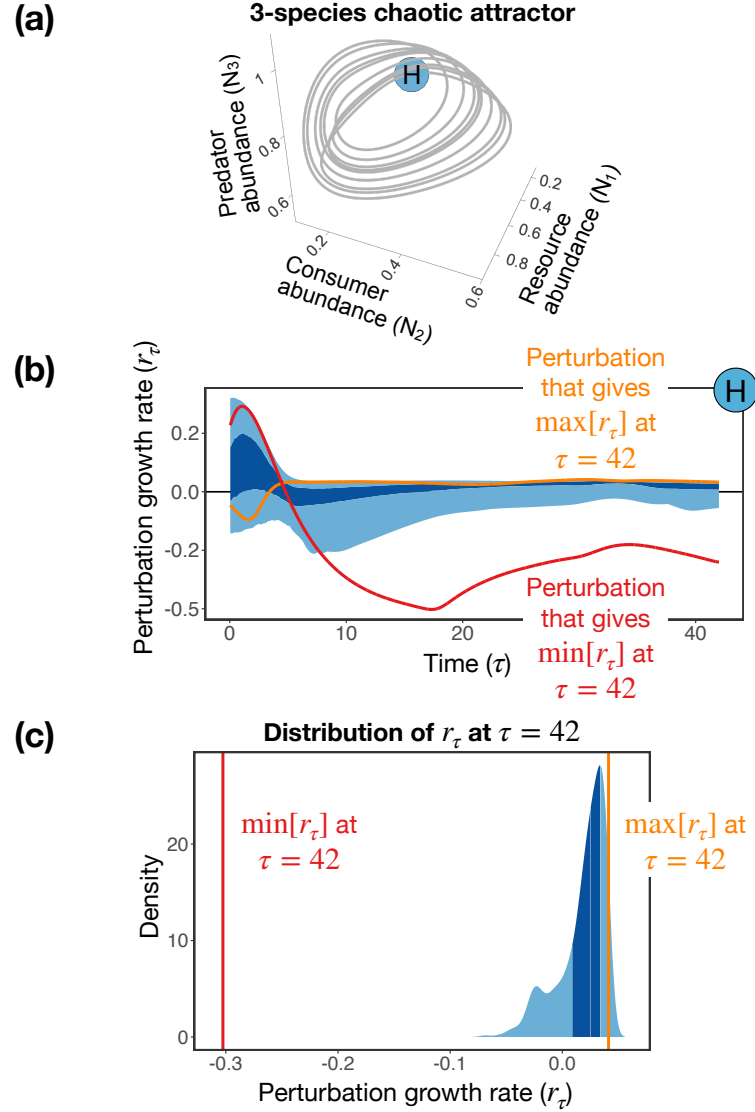


Figure S6. Demonstration that the metric for minimum perturbation growth rate ($\min[r_\tau]$) captures the minimum growth rate of simulated perturbations. The figure focuses on the results shown in Fig. 3 for scenario 4 (Hastings-Powell model under a chaotic attractor) at a long time scale. (a) Trajectory of unperturbed abundances ($\hat{\mathbf{N}}(t)$, gray line) and the location along the trajectory (blue point) for which we performed this analysis. (b) Distribution of growth rate of 500 simulated perturbations (blue shade) and growth rate of the two perturbations that give the maximum (orange line) and minimum (red line) values at $\tau = 42$. The dark blue shade denotes the region between the 25th and 75th percentiles, whereas the light blue shade goes to the minimum and maximum values of r_τ . As seen in Fig. 3, none of the 500 perturbations gives $\min[r_\tau]$ at $\tau = 42$. Nevertheless, although it is very unlikely that this perturbation will be sampled, it exists, as shown by the red line. (c) Distribution of growth rate of the 500 simulated perturbations at $\tau = 42$. Dark and light blue shades are the same as in (b). Orange and red vertical lines denote $\max[r_\tau] = 0.041$ and $\min[r_\tau] = -0.303$ at $\tau = 42$, respectively.

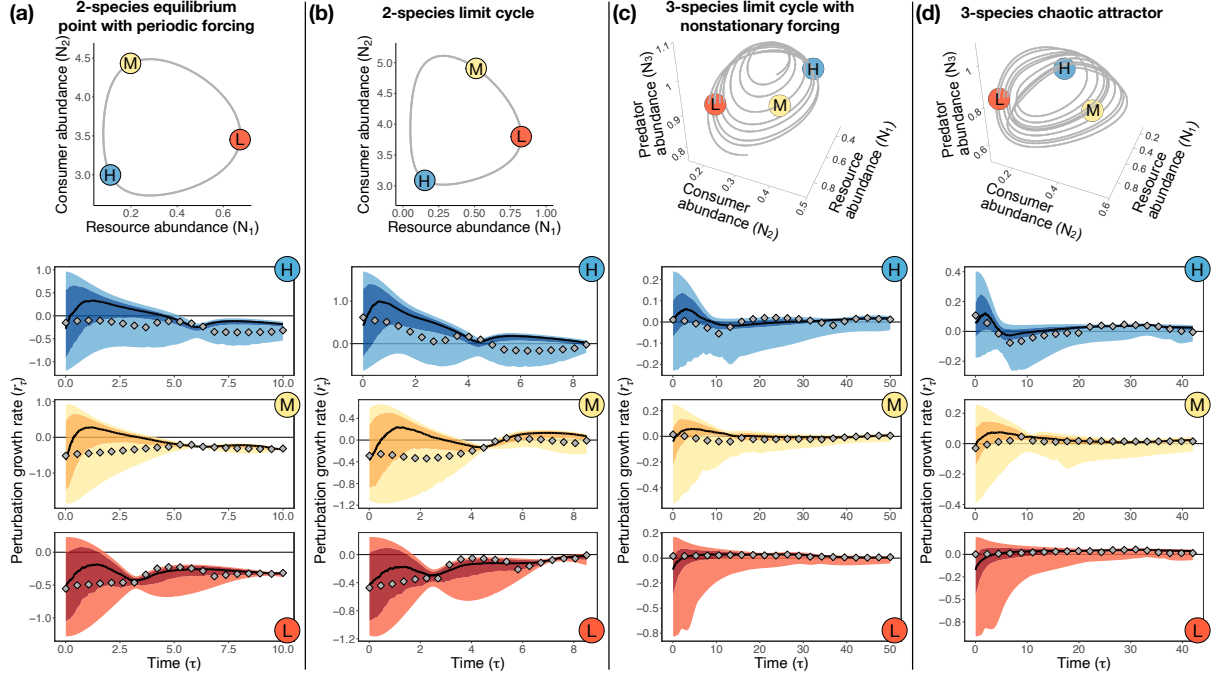


Figure S7. Accuracy of the largest eigenvalue of the state-transition matrix Φ as a metric for the maximum perturbation growth rate. As explained in Section S3, $\frac{1}{\tau} \log [\max[|\lambda_i(\Phi)|]]$ approximates the maximum perturbation growth rate for large τ (i.e., $\tau \rightarrow \infty$). Each column (a-d) depicts a scenario, where the top plot shows the trajectory of unperturbed abundances ($\bar{N}(t)$, gray line) and the three bottom plots show the outcome of simulated perturbations (blue, yellow, and red shades) together with $\frac{1}{\tau} \log [\max[|\lambda_i(\Phi)|]]$ as gray diamonds. Points labeled as H (in blue), M (in yellow), and L (in red) represent locations along the trajectory with high, medium, and low median perturbation growth rate (for small τ), respectively. In bottom plots, the dark shade denotes the region between the 25th and 75th percentiles, whereas the light shade goes to the minimum and maximum values of r_τ . Bottom plots span $t = 0$ to $t = T$, where T denotes the recurrence time of the system. Scenarios (a) through (d) are the same as the ones in Fig. 3.

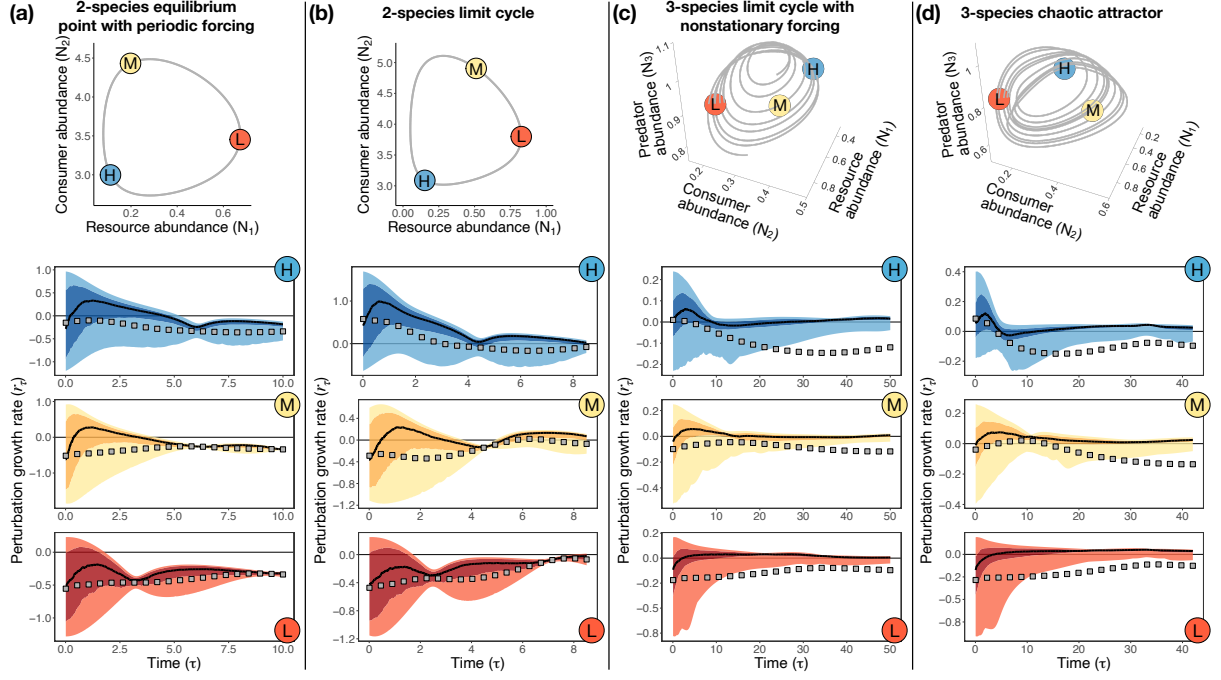


Figure S8. Accuracy of the determinant of the state-transition matrix Φ as a metric for the median perturbation growth rate. As explained in Section S3, $\frac{1}{S\tau} \log [\det(\Phi)]$ approximates the median perturbation growth rate for small τ (i.e., $\tau \rightarrow 0$). Each column (a-d) depicts a scenario, where the top plot shows the trajectory of unperturbed abundances ($\tilde{N}(t)$, gray line) and the three bottom plots show the outcome of simulated perturbations (blue, yellow, and red shades) together with $\frac{1}{S\tau} \log [\det(\Phi)]$ as gray squares. Points labeled as H (in blue), M (in yellow), and L (in red) represent locations along the trajectory with high, medium, and low median perturbation growth rate (for small τ), respectively. In bottom plots, the dark shade denotes the region between the 25th and 75th percentiles, whereas the light shade goes to the minimum and maximum values of r_τ . Bottom plots span $t = 0$ to $t = T$, where T denotes the recurrence time of the system. Scenarios (a) through (d) are the same as the ones in Fig. 3.

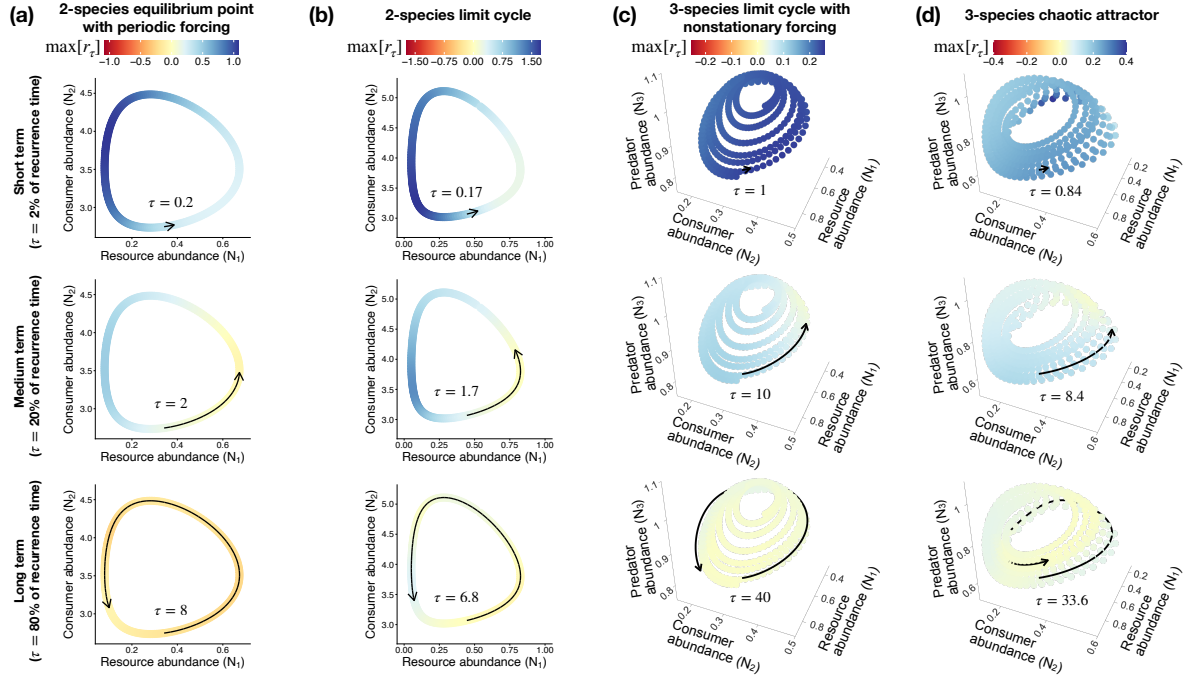


Figure S9. Impact of time scale (τ) on responses to pulse perturbations using $\max[r_\tau]$ instead of \bar{r}_τ as the stability metric. Although the values of $\max[r_\tau]$ (this figure) and \bar{r}_τ (Fig. 4) are different, the state-dependent patterns under each scenario are similar for these two metrics. Each column (a-d) depicts a scenario and each row depicts a time scale (short, medium, and long time scales). Time scales are defined in terms of the recurrence time T of the system. Each colored point in each plot denotes a given unperturbed state ($\tilde{\mathbf{N}}(t)$) along a trajectory at which we compute the maximum perturbation growth rate ($\max[r_\tau]$). Black arrows in each plot indicate the time scale τ . Scenarios (a) through (d) are the same as the ones in Fig. 4.

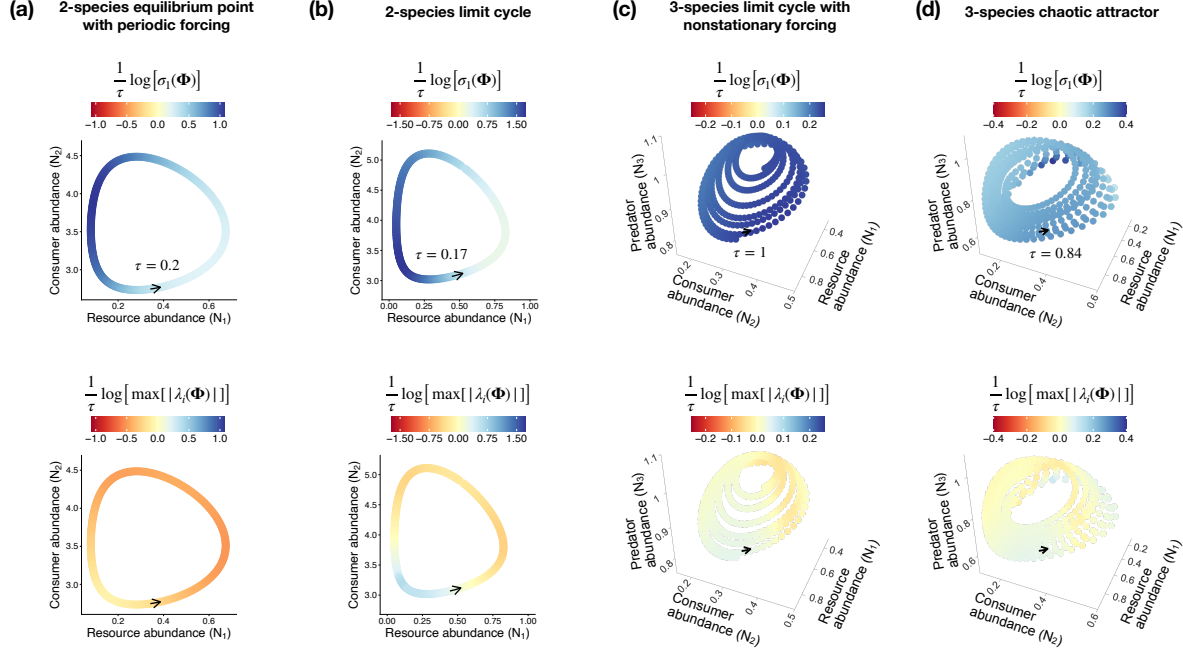


Figure S10. Comparison between the largest singular value ($\sigma_1(\Phi)$) and the largest eigenvalue ($\max[|\lambda_i(\Phi)|]$) of the state-transition matrix Φ as stability metrics under a short time scale ($\tau = 0.02T$, where T is the recurrence time of the system). Top plots show $\max[r_\tau] = \frac{1}{\tau} \log [\sigma_1(\Phi)]$ (same as top plots in Fig. S9), whereas bottom plots show $\frac{1}{\tau} \log [\max[|\lambda_i(\Phi)|]]$. Within each scenario (columns a to d), the state-dependent pattern of the top and bottom plots are very different. Each colored point in each plot denotes a given unperturbed state ($\tilde{\mathbf{N}}(t)$) along a trajectory at which we compute the two metrics. Black arrows in each plot indicate the time scale τ . Scenarios (a) through (d) are the same as the ones in Fig. 4.

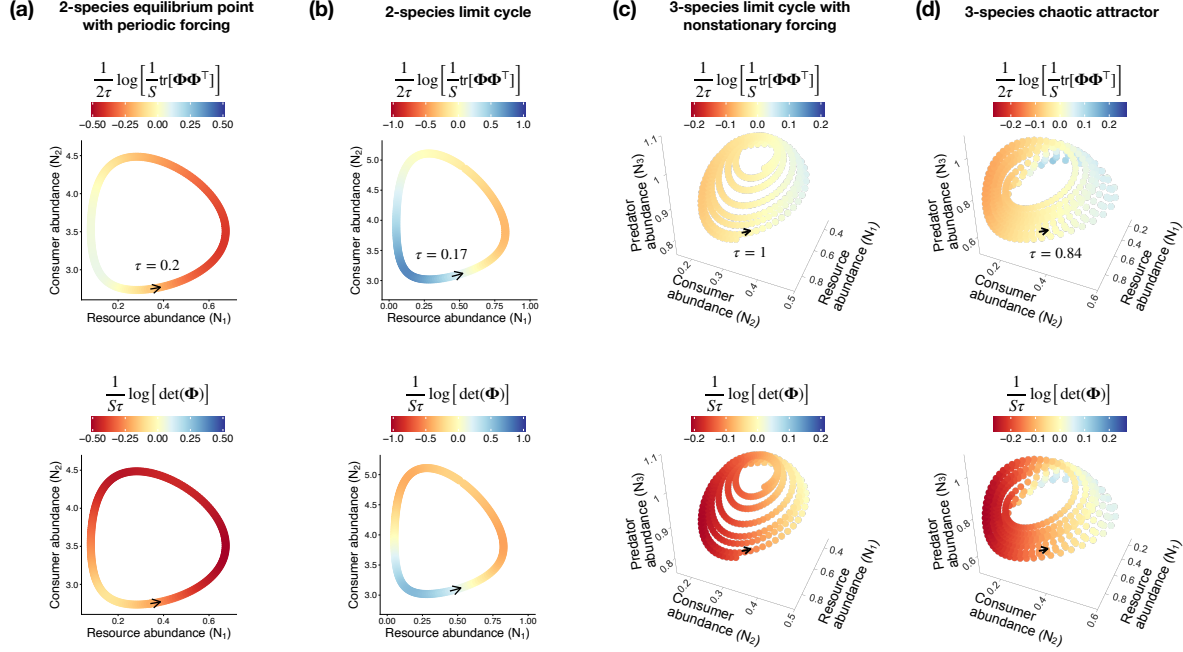


Figure S11. Comparison between the trace of $\Phi\Phi^T$ and the determinant of Φ as stability metrics under a short time scale ($\tau = 0.02T$, where T is the recurrence time of the system). Top plots show $\bar{r}_\tau = \frac{1}{2\tau} \log \left[\frac{1}{S} \text{tr}[\Phi\Phi^T] \right]$ (same as top plots in Fig. 4), whereas bottom plots show $\frac{1}{S\tau} \log [\det(\Phi)]$. Within each scenario (columns a to d), the state-dependent pattern of the top and bottom plots are similar. Each colored point in each plot denotes a given unperturbed state ($\tilde{\mathbf{N}}(t)$) along a trajectory at which we compute the two metrics. Black arrows in each plot indicate the time scale τ . Scenarios (a) through (d) are the same as the ones in Fig. 4.

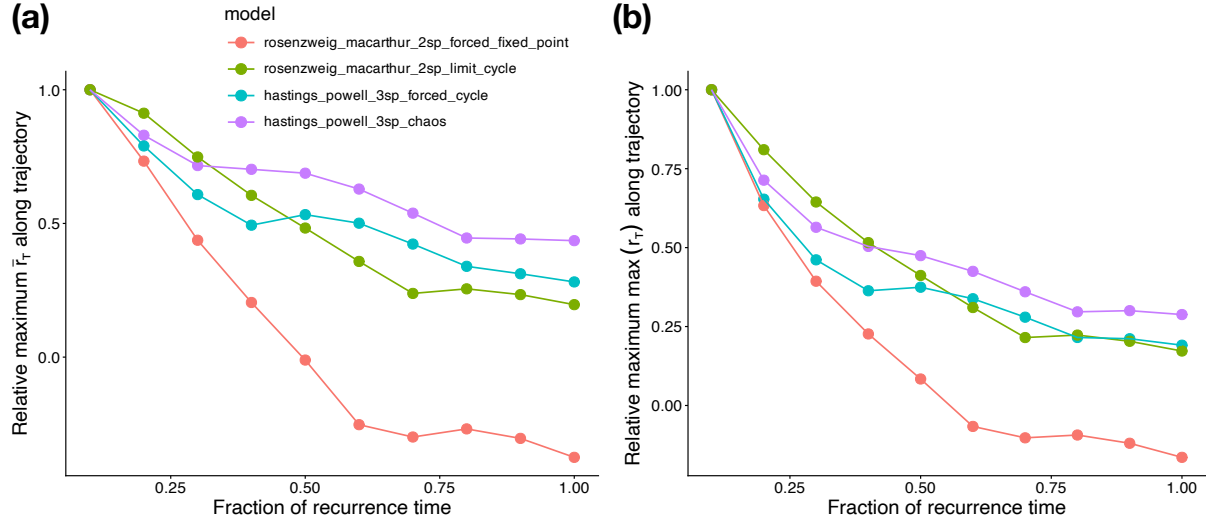


Figure S12. Dependence of (a) median perturbation growth rate (\bar{r}_τ) and (b) maximum perturbation growth rate ($\max[r_\tau]$) on τ across all nonequilibrium scenarios (different colors). The figure shows the fraction of the recurrence time T used as τ in the x-axis and a scaled version of the maximum value of (a) \bar{r}_τ and (b) $\max[r_\tau]$ in the y-axis. We scaled the y-axis by diving the metric within each scenario by its maximum value across all values of τ . Thus, all curves start at 1 and converge towards the long-term value for (a) \bar{r}_τ or (b) $\max[r_\tau]$ as τ increases. This convergence is faster for the forced equilibrium point (red curve) and slower for the chaotic attractor (purple curve). These different rates of convergence could be used as a way to distinguish different types of dynamics in natural communities. For example, the rate of convergence of different communities could be compared to determine which one shows more evidence of chaotic dynamics.

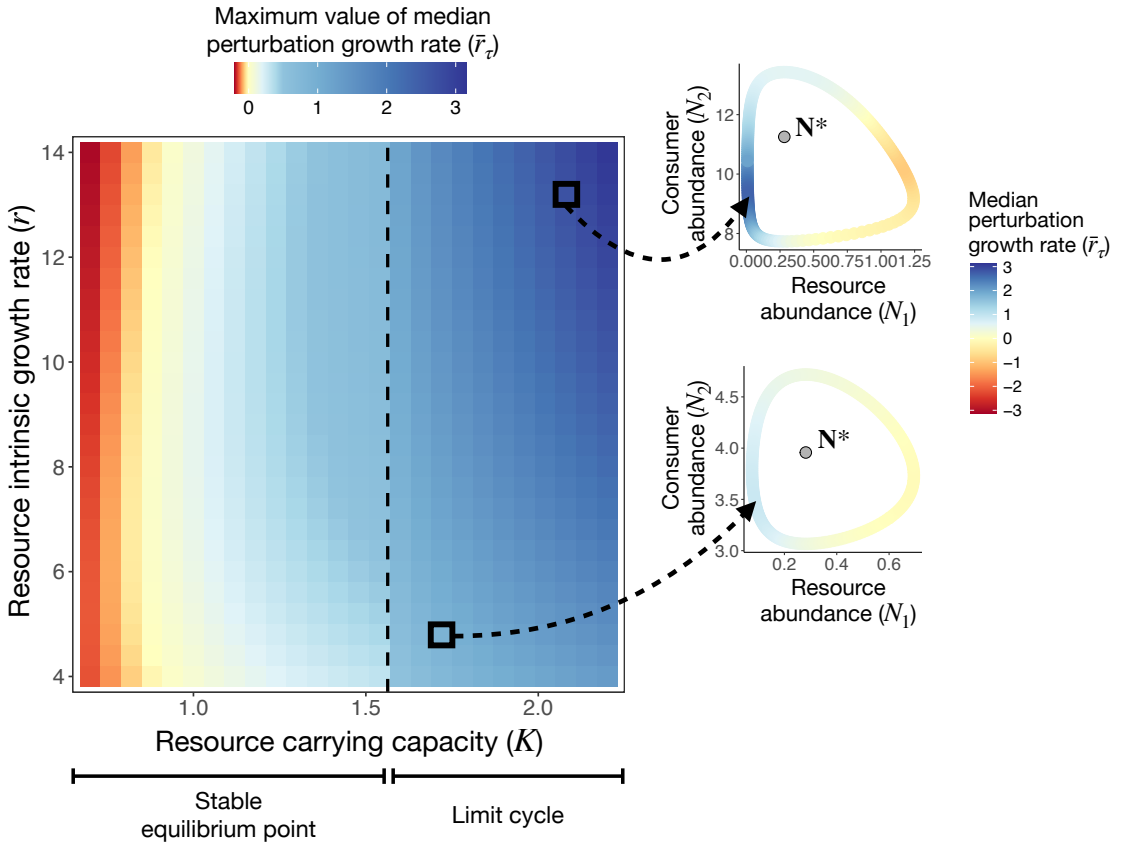


Figure S13. Impact of parameter changes in a 2-species resource-consumer model (main text equation (24)) on the median perturbation growth rate (\bar{r}_τ) under equilibrium (a) and nonequilibrium (b) dynamics (Section S6). For each combination of resource carrying capacity (K) and intrinsic growth rate (r), the heatmap shows the maximum value of \bar{r}_τ across the attractor. We computed \bar{r}_τ assuming a short time scale ($\tau = 1.5$). For $K < 1.56$ (left of the dashed line), the attractor is a stable equilibrium point (\mathbf{N}^*) and the maximum of \bar{r}_τ is simply \bar{r}_τ computed at \mathbf{N}^* . The vertical dashed line denotes the Hopf bifurcation at $K_H = 1.56$. For $K > 1.56$ (right of the dashed line), the equilibrium point becomes unstable and the attractor becomes a limit cycle. For the limit cycle regime, the heatmap shows the maximum of \bar{r}_τ along the unperturbed cycle ($\dot{\mathbf{N}}(t)$) for each parameter combination. Examples of \bar{r}_τ at different states along the cycle are shown to the right of the heatmap for two parameter combinations. Note that the color scale for the heatmap (at the top) is nonlinear to accommodate a wide range of \bar{r}_τ values.

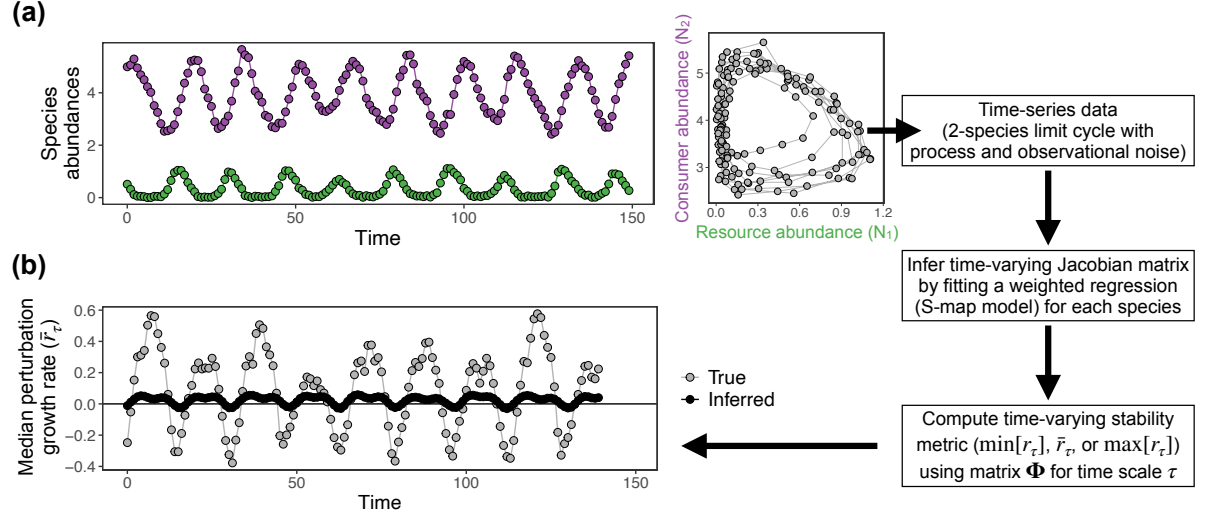


Figure S14. Inference of stability metrics from abundance time series generated from a 2-species resource-consumer model under a limit cycle (equation (S53)). For this figure, we use the standard S-map model, instead of the extension of the S-map model that assumes continuous-time dynamics as in Fig. 5 (see Section S7). (a) Plot on the left shows the noisy time-series data for the resource ($N_1(t)$; green points) and consumer ($N_2(t)$; purple points) species with 150 observations ($t = 0, 1, \dots, 149$). Plot on the right shows the same data but plotted in state space. From this data, we first infer the discrete-time Jacobian matrix $\mathbf{J}_F(t)$ at all times t using a weighted regression (S-map model). Then, we compute the state-transition matrix Φ and the median perturbation growth rate (\bar{r}_τ) at time scale $\tau = 10$. (b) Median perturbation growth rate for all times t computed analytically from equation (S53) (gray points) and inferred from the time series (black points). The correlation between true and inferred \bar{r}_τ is 0.83. The S-map hyperparameters selected with cross-validation are: $\theta = 2$, $\alpha = 0$, and $\lambda = 0$.

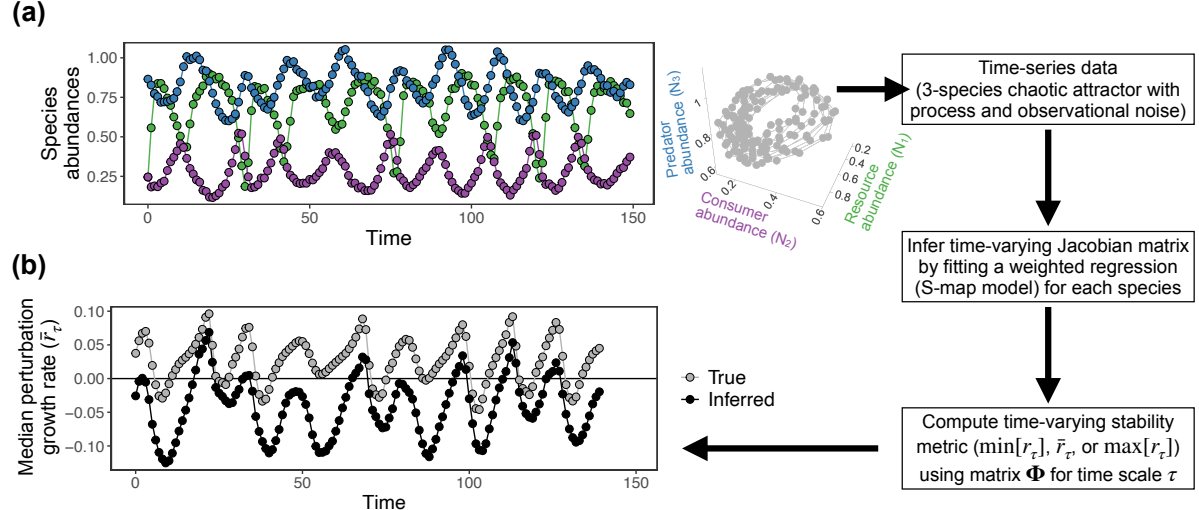


Figure S15. Inference of stability metrics from abundance time series generated from a 3-species food chain model under a chaotic attractor (equation (S54)). For this figure, we use the 3-species Hastings-Powell model instead of the Rosenzweig-MacArthur model as in Fig. 5 (see Section S7). (a) Plot on the left shows the noisy time-series data for the resource ($N_1(t)$; green points), consumer ($N_2(t)$; purple points), and top predator ($N_3(t)$; blue points) species with 150 observations ($t = 0, 1, \dots, 149$). Plot on the right shows the same data but plotted in state space. From this data, we first infer the Jacobian matrix $\mathbf{J}_f(t)$ at all times t using a weighted regression (S-map model) and assuming continuous-time dynamics. Then, we compute the state-transition matrix Φ and the median perturbation growth rate (\bar{r}_τ) at time scale $\tau = 10$. (b) Median perturbation growth rate for all times t computed analytically from equation (S54) (gray points) and inferred from the time series (black points). The correlation between true and inferred \bar{r}_τ is 0.83. The S-map hyperparameters selected with cross-validation are: $\theta = 2$, $\alpha = 0$, and $\lambda = 0$.

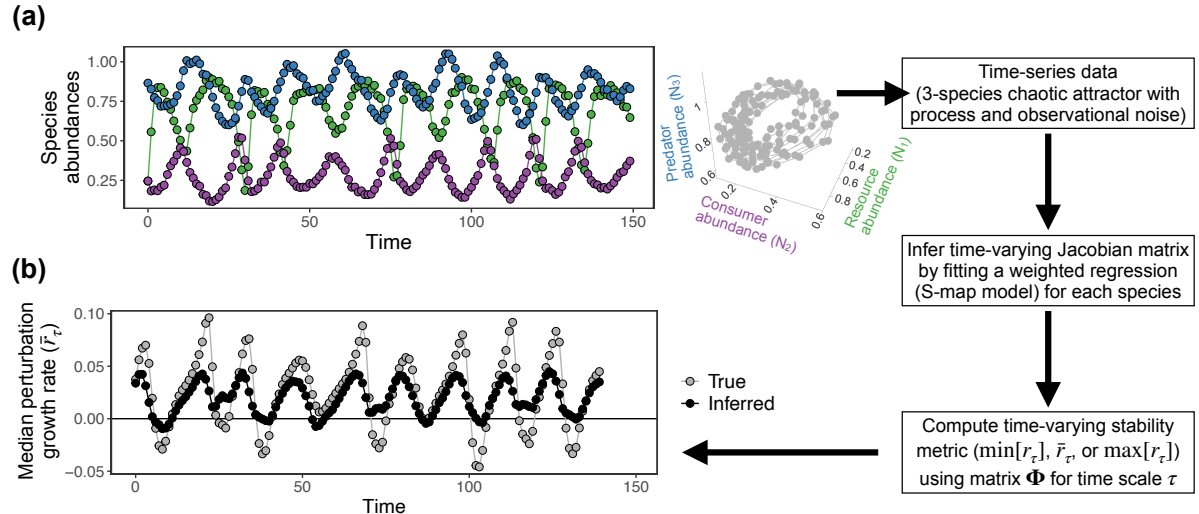


Figure S16. Inference of stability metrics from abundance time series generated from a 3-species food chain model under a chaotic attractor (equation (S54)). For this figure, we use the standard S-map model with the 3-species Hastings-Powell model, instead of the extension of the S-map model that assumes continuous-time dynamics with the Rosenzweig-MacArthur model as in Fig. 5 (see Section S7). (a) Plot on the left shows the noisy time-series data for the resource ($N_1(t)$; green points), consumer ($N_2(t)$; purple points), and top predator ($N_3(t)$; blue points) species with 150 observations ($t = 0, 1, \dots, 149$). Plot on the right shows the same data but plotted in state space. From this data, we first infer the discrete-time Jacobian matrix $\mathbf{J}_F(t)$ at all times t using a weighted regression (S-map model). Then, we compute the state-transition matrix Φ and the median perturbation growth rate (\bar{r}_τ) at time scale $\tau = 10$. (b) Median perturbation growth rate for all times t computed analytically from equation (S54) (gray points) and inferred from the time series (black points). The correlation between true and inferred \bar{r}_τ is 0.80. The S-map hyperparameters selected with cross-validation are: $\theta = 2$, $\alpha = 0$, and $\lambda = 0.01$.

468 **References**

- 469 Argyris, J.H., Faust, G., Haase, M. & Friedrich, R. (2015). *An Exploration of Dynamical*
470 *Systems and Chaos*. Springer.
- 471 Arnoldi, J.F., Bideault, A., Loreau, M. & Haegeman, B. (2018). How ecosystems re-
472 cover from pulse perturbations: A theory of short-to long-term responses. *Journal of*
473 *Theoretical Biology*, 436, 79–92.
- 474 Caswell, H. & Neubert, M.G. (2005). Reactivity and transient dynamics of discrete-time
475 ecological systems. *Journal of Difference Equations and Applications*, 11, 295–310.
- 476 Cenci, S. & Saavedra, S. (2019). Non-parametric estimation of the structural stability of
477 non-equilibrium community dynamics. *Nature Ecology & Evolution*, 3, 912–918.
- 478 Cenci, S., Sugihara, G. & Saavedra, S. (2019). Regularized s-map for inference and
479 forecasting with noisy ecological time series. *Methods in Ecology and Evolution*, 10,
480 650–660.
- 481 Chang, C.W., Miki, T., Ushio, M., Ke, P.J., Lu, H.P., Shiah, F.K. & Hsieh, C.h. (2021).
482 Reconstructing large interaction networks from empirical time series data. *Ecology*
483 *Letters*, 24, 2763–2774.
- 484 Costantino, R.F., Desharnais, R.A., Cushing, J.M. & Dennis, B. (1997). Chaotic dynam-
485 ics in an insect population. *Science*, 275, 389–391.
- 486 Datseris, G. & Parlitz, U. (2022). *Nonlinear Dynamics: A Concise Introduction Interlaced*
487 *with Code*. Springer Nature.
- 488 Deyle, E.R., May, R.M., Munch, S.B. & Sugihara, G. (2016). Tracking and forecasting
489 ecosystem interactions in real time. *Proceedings of the Royal Society B: Biological*
490 *Sciences*, 283, 20152258.
- 491 Golub, G.H. & Van Loan, C.F. (2013). *Matrix Computations*. JHU press.
- 492 Grziwotz, F., Chang, C.W., Dakos, V., van Nes, E.H., Schwarzländer, M., Kamps, O.,
493 Heßler, M., Tokuda, I.T., Telschow, A. & Hsieh, C.h. (2023). Anticipating the occur-
494 rence and type of critical transitions. *Science Advances*, 9, eabq4558.
- 495 Hampton, S.E., Holmes, E.E., Scheef, L.P., Scheuerell, M.D., Katz, S.L., Pendleton, D.E.
496 & Ward, E.J. (2013). Quantifying effects of abiotic and biotic drivers on community
497 dynamics with multivariate autoregressive (mar) models. *Ecology*, 94, 2663–2669.
- 498 Hastie, T., Tibshirani, R., Friedman, J. *et al.* (2009). *The elements of statistical learning*.
499 Springer series in statistics New-York.
- 500 Hastings, A. & Powell, T. (1991). Chaos in a three-species food chain. *Ecology*, 72,
501 896–903.

- 502 Ives, A.R., Dennis, B., Cottingham, K.L. & Carpenter, S.R. (2003). Estimating community
503 stability and ecological interactions from time-series data. *Ecological Monographs*,
504 73, 301–330.
- 505 McCann, K.S. (2011). *Food Webs (MPB-50)*. Princeton University Press.
- 506 Medeiros, L.P., Allesina, S., Dakos, V., Sugihara, G. & Saavedra, S. (2023). Ranking
507 species based on sensitivity to perturbations under non-equilibrium community dy-
508 namics. *Ecology Letters*, 26, 170–183.
- 509 Medeiros, L.P. & Saavedra, S. (2023). Understanding the state-dependent impact of
510 species correlated responses on community sensitivity to perturbations. *Ecology*, p.
511 e4115.
- 512 Munch, S.B., Brias, A., Sugihara, G. & Rogers, T.L. (2020). Frequently asked questions
513 about nonlinear dynamics and empirical dynamic modelling. *ICES Journal of Marine
514 Science*, 77, 1463–1479.
- 515 Munch, S.B., Rogers, T.L. & Sugihara, G. (2023). Recent developments in empirical
516 dynamic modelling. *Methods in Ecology and Evolution*, 14, 732–745.
- 517 Nazerian, A., Sorrentino, F. & Aminzare, Z. (2024). Bridging the gap between reactivity,
518 contraction and finite-time lyapunov exponents. *arXiv preprint arXiv:2410.23435*.
- 519 Neubert, M.G. & Caswell, H. (1997). Alternatives to resilience for measuring the re-
520 spondes of ecological systems to perturbations. *Ecology*, 78, 653–665.
- 521 Nguyen, P.L., Pomati, F. & Rohr, R.P. (2025). Inferring coexistence likelihood in chang-
522 ing environments from ecological time series. *Proceedings of the National Academy of
523 Sciences*, 122, e2417905122.
- 524 Perko, L. (2013). *Differential Equations and Dynamical Systems*. vol. 7. Springer Science
525 & Business Media.
- 526 Rogers, T.L., Johnson, B.J. & Munch, S.B. (2022). Chaos is not rare in natural ecosys-
527 tems. *Nature Ecology & Evolution*, 6, 1105–1111.
- 528 Rogers, T.L., Munch, S.B., Matsuzaki, S.i.S. & Symons, C.C. (2023). Intermittent insta-
529 bility is widespread in plankton communities. *Ecology Letters*, 26, 470–481.
- 530 Rosenzweig, M.L. & MacArthur, R.H. (1963). Graphical representation and stability
531 conditions of predator-prey interactions. *The American Naturalist*, 97, 209–223.
- 532 Song, C. & Saavedra, S. (2021). Bridging parametric and nonparametric measures of
533 species interactions unveils new insights of non-equilibrium dynamics. *Oikos*, 130,
534 1027–1034.

- 535 Stein, R.R., Bucci, V., Toussaint, N.C., Buffie, C.G., Rätsch, G., Pamer, E.G., Sander,
536 C. & Xavier, J.B. (2013). Ecological modeling from time-series inference: Insight
537 into dynamics and stability of intestinal microbiota. *PLoS Computational Biology*, 9,
538 e1003388.
- 539 Strogatz, S.H. (2000). *Nonlinear Dynamics and Chaos: With Applications to Physics,*
540 *Biology, Chemistry, and Engineering*. CRC press.
- 541 Sugihara, G. (1994). Nonlinear forecasting for the classification of natural time series.
542 *Philosophical Transactions of the Royal Society of London. Series A: Physical and*
543 *Engineering Sciences*, 348, 477–495.
- 544 Suzuki, K., Yoshida, K., Nakanishi, Y. & Fukuda, S. (2017). An equation-free method re-
545 veals the ecological interaction networks within complex microbial ecosystems. *Methods*
546 *in Ecology and Evolution*, 8, 1774–1785.
- 547 Takens, F. (1981). Detecting strange attractors in turbulence. In: *Dynamical Systems*
548 *and Turbulence, Warwick 1980*. Springer, pp. 366–381.
- 549 Tay, J.K., Narasimhan, B. & Hastie, T. (2023). Elastic net regularization paths for all
550 generalized linear models. *Journal of Statistical Software*, 106, 1–31.
- 551 Ushio, M., Hsieh, C.h., Masuda, R., Deyle, E.R., Ye, H., Chang, C.W., Sugihara, G. &
552 Kondoh, M. (2018). Fluctuating interaction network and time-varying stability of a
553 natural fish community. *Nature*, 554, 360–363.
- 554 Zhang, H., Ma, S., Huang, T., Cong, X., Gao, Z. & Zhang, F. (2018). Complex dynamics
555 on the routes to chaos in a discrete predator-prey system with crowley-martin type
556 functional response. *Discrete Dynamics in Nature and Society*, 2018, 2386954.
- 557 Zhao, Q., Van den Brink, P.J., Xu, C., Wang, S., Clark, A.T., Karakoç, C., Sugihara,
558 G., Widdicombe, C.E., Atkinson, A., Matsuzaki, S.i.S. *et al.* (2023). Relationships
559 of temperature and biodiversity with stability of natural aquatic food webs. *Nature*
560 *Communications*, 14, 3507.